Archives of Computational Methods in Engineering (2021) 28:4979–5020
https://doi.org/10.1007/s11831-021-09568-9

ORIGINAL PAPER

Theories and Applications of CFD–DEM Coupling Approach for Granular Flow: A Review

Mahmoud A. El-Emam[1,2] · Ling Zhou[1] · Weidong Shi[3] · Chen Han[1] · Ling Bai[1] · Ramesh Agarwal[4]

Received: 20 December 2019 / Accepted: 2 March 2021 / Published online: 12 April 2021

Abstract

Bio-particulate matter includes grains, cereal crops, and biomass that are considered discrete materials with irregular size and shape. Although the flow of these particles can behave like a continuum fluid at times, their discontinuous behavior cannot be simulated with traditional continuum-based modeling. The Discrete Element Method (DEM), coupled with Computational Fluid Dynamics (CFD), is considered a promising numerical method that can model discrete particles by tracking the motion of each particle in fluid flow. DEM has been extensively used in the field of engineering, where its application is starting to achieve the popularity in agricultural processing. While CFD has been able to simulate the complex fluid flows with a quantitative and qualitative description of the temporal and spatial change of the flow field. This paper reviews the recent strategies and the existing applications of the CFD–DEM coupling approach in aerodynamic systems of bio-particles. It mainly represents four principal aspects: the definition of aerodynamic systems with its principals, modeling of particle motion including interaction forces of particle–particle and particle–fluid in the system, CFD–DEM coupling methodologies, and drag correlation models with theoretical developments, and the applications of aerodynamic systems related to the agricultural field. The existing published literature indicates that CFD–DEM is a promising approach to study the bio-particulate matter behavior immersed in fluid flow, and it could be benefiting from developing and optimizing the device's geometry and the operations. The main findings are discussed and summarized as a part of the review, where future developments and challenges are highlighted.

Abbreviations

A_i	Projected area of particle
a	Separation radius between particles
C_d	Drag coefficient
C_{ij}	Convection
$D_{T,ij}$	Turbulent diffusion
$D_{L,ij}$	Molecular diffusion
D	Domain diameter
d	Normal distance to the wall
d_i	Particle diameter
$d_{i_{vol}}$	Particle diameter with the same volume of the actual one
E_i	Young's modulus of particle
E_w	Young's modulus of wall boundary
F_{net}	Net force acting on a particle
F_{ij}^{C}	Total contact force acting on a particle
F_i^f	Fluid-particle interaction force
F_{ij}^{n}	Normal contact force on a particle
F_{ij}^{t}	Tangential contact force on a particle
$F_i^{t,T}$	Tangential contact force at current time
$F_i^{t,(T-\Delta T)}$	Tangential contact force at previous time
$F_i^{n,T}$	Normal contact force at current time
$F_i^{n,(T-\Delta T)}$	Normal contact force at previous time
$F_{i_{adh}}^{n,T}$	Normal adhesive force at current time
F_{ij}	Force production by system rotation
F_i^f	Interaction force of the fluid on particle
f_i^g	Gravity force
f_{adh}	Adhesive force fraction
G_k	Kinetic energy generation due to the velocity

✉ Ling Zhou
lingzhou@ujs.edu.cn

[1] Research Center of Fluid Machinery Engineering and Technology, Jiangsu University, Zhenjiang 212013, China

[2] Department of Agricultural and Biosystems Engineering, Alexandria University, Shatby 21526, Egypt

[3] School of Mechanical Engineering, Nantong University, Nantong 226019, China

[4] Department of Mechanical Engineering and Materials Science, Washington University in Saint Louis, St. Louis 63130, USA

G_b	Kinetic energy generation due to buoyancy
G_{ij}	Buoyancy production rate of $\overline{u_i' u_j'}$
g	Gravity acceleration
T_K	Kolmogorov time scale
T_e	Turnover time of large eddy
T	Time
u	Root mean square of fluid velocity
u_f	Average velocity component of fluid
V_a	Air velocity
V_T	Terminal velocity
V_f	Average velocity of the fluid
V_i and V_j	Particles velocity before interaction
V_i' and V_j'	Particles velocity after interaction
Vol_i	Particle volume
Vol	Volume occupied by particles and fluid
Y_M	Dilatation contribution over dissipation rate
Z	Particle size or geometry
$\phi_{ij,1}$	Slow pressure-strain
$\phi_{ij,2}$	Rapid pressure-strain
$\phi_{ij,3}$	Wall-reflection term
ϕ_{ij}	Pressure strain
$\emptyset_i$	Particle sphericity
η	Damping ratio
η^t	Tangential damping ratio
K_1	Stokes' shape factor
K_2	Newton's shape factor
k_a	Coefficient of aerodynamic resistance
K_u^n	Unloading contact stiffnesses
K_l^n	Loading contact stiffnesses
l	Length scale of the energy-containing eddies
m^*	Equivalent mass of particles
m_i and m_j	Mass of particles i and j
N	Number of particles
n_k	Component of x_k normal to the wall
$\widehat{n_c}$	Unit vector in the normal direction
n and t	Normal and tangential coordinates
p	Pressure shared by two phases
P_{max}	Maximum liquid bridge tensile force
P_{ij}	Stress production rate of $\overline{u_i' u_j'}$
R_{e_i}	Particle Reynolds number
R_ϵ	Dissipation of swirl and rotational effect
R_e	Reynolds number
R_i and R_j	Radii of particles i and j
s_{max}^t	Maximum relative tangential displacement
s^t	Tangential relative displacement at contact
S^n	Normal overlapping
ΔS^n	Change in the normal overlapping
ΔS^t	Change in the tangential overlapping
$S^{n,T}$	Normal overlap value at the current time
$S^{n,T-\Delta T}$	Normal overlap value at the previous time
S_k and S_ϵ	Constant source terms for user-defined
S_{user}	Constant source term for user-defined
ΔT	Timestep
T_i	Response time of particle
ρ_f	Fluid density
$\rho_f \overline{u_i' u_j'}$	Reynolds stress tensor
ρ_a	Air density
ρ_i	Particle density
μ_f	Fluid turbulent viscosity
μ_t	Turbulent viscosity
μ	Friction coefficient
μ_a	Dynamic viscosity of the air
$\mu_{f_{eff}}$	Effective turbulent viscosity of a fluid
α_f	Fluid volume fraction
α_k and α_ϵ	Inverse effective Prandtl number for k and ϵ
α_i	Particle volume fraction of
ϵ	Coefficient of restitution
σ_k and σ_ϵ	Turbulent Prandtl numbers for k and ϵ
Γ	Surface energy
ϵ_{ij}	Dissipation
δ_{adh}	Adhesive distance
τ_f	Viscous stress tensor
υ_f	Kinematic viscosity of the fluid
$\frac{d}{dT} S^t$	Relative tangential velocity at the contact

1 Introduction

1.1 Bio-particulate Matter

Agriculture crops are the primary source of various bio-particulate matter include cereal grains, seeds, and biomass, which are differences in shape, size, density, and other physical characteristics. These materials, which are considered the primary bio-particulate matter in this investigation, are used as a raw material or grinded for energy (biomass) production or food to provide calories and protein resource for human and animal diet. It sometimes contains a heterogeneous mass of foreign materials such as sands, stones, sticks, chaff, glass fragments, weed, and other crop seeds. These contaminants are mainly introduced during harvesting and post-harvesting process [1]. Therefore, before being processed, separation and purification of cereal grains and seeds from impurities is an essential process in food processing and oilseed trading [2]. This process can be carried out by more technological procedures depending on their physio-mechanical characteristics. In this way, a part of impurities is cast away depending on their size (width, length, thickness); others are separated depending on their drag coefficient [3]. Given that the principle of separation and the type of impurities, a wide range of technical equipment and installations are used

for carrying out the separation of impurities such as aerodynamic separators, screening devices, magnetic separators, vibrating separators, etc. [4]. Herein, the current work will focus only on the aerodynamic systems and processing used for bio-particles such as cereal grains and seeds.

1.2 Aerodynamic Principals

Generally, aerodynamic devices are commonly used in the separation process of bio-particulate matter. It can be defined as a process of using air generated by natural or mechanical fan to remove light, chaffy, and dusty materials out of the bio-particles. It is considered one of the critical methods which can be used lonely or usually in conjunction with another method to separate and clean various heterogeneous agricultural grain mixtures [5–7]. The advantages of this technique can be summarized in the following points: allow for cleaning and segregation of seeds particles simultaneously without changing the separation parameters, obtain the product without damage, no change in the physical and biological properties of the particles during the separation process, and characterized by a high efficiency without demand much power [8]. Found that the most effective factors to improve the quality of the aerodynamic system are: the aerodynamic properties of the particulate matter, feeding load ratio of granular flow, speed and angle of feed grain material, airflow properties, particles properties, and the system inlet geometry [9–12].

In this process, the aerodynamic properties of particles, such as their critical or terminal velocity and drag coefficient, are mainly used [7, 13]. The large the difference values of terminal velocities in the mixture component, the better and more efficient is the aerodynamic separation [14, 15]. Commonly, the aerodynamic systems can be classified into three significant aspects based on the direction of the air stream in the system: vertical, horizontal, and oblique.it can also classified depending on the conditions of the airflow or location of the fan in the system (vacuum, overpressure, and hybrid) [15, 16]. Herein, the value of the redistribution of product components between fractions should be taken into account to evaluate the quality of the aerodynamic separation process, mainly when the initial product is divided into three or more fractions [17].

The expediency of using forced air technology is determined by the presence in the initial material of components that differ from the main product by aerodynamic properties. If there are no such differences, other methods will be used. Up to 70% of the impurities in the original grain material that comes to post-harvest processing are separated from the main crop by aerodynamic characteristics [17]. The efficiency of any air-using machine depends on the weight and aerodynamic drag of the particles, which in turn affects their terminal velocity of fall [18]. Consequently, awareness of the aerodynamic properties seems necessary in the proper design of aerodynamic equipment. The drag coefficients of a wide range of bio-particles material have been measured experimentally by finding the suspension velocities of the particles in an airstream [19, 20]. To correlate the drag coefficient, the Reynolds number has been used by grouping the particles within the limits of a sphere and a cylinder shape [21]. The need to correlate the drag coefficient is the difference between the experiment and the calculated terminal velocity of grains. As mentioned above, the aerodynamic properties can be mainly described by two major aspects: critical or terminal velocity and drag coefficient [22]. The first parameter, which is considered the main representation of the aerodynamic properties of particles, can be mainly used as their distinguishing feature in such aerodynamic applications and optimizations [8, 20, 23]. Terminal velocity is the velocity of the vertical air stream which keeps the particle to be suspended in the air as a result of balancing their weight with the force of the air stream [24–26]. The values of this parameter are affected by some secondary parameters like density, shape, and cross-sectional area [22] that can be formulated according to Eq. (1) [27, 28]. The greater the particle mass, the greater the terminal velocity, and the larger the particle area, the lower the velocity.

$$V_T = \sqrt{\frac{m_i g}{k_a A_i \rho_a}} or \cong \sqrt{\frac{4 d_i \left(\rho_i - \rho_a\right) g}{3 C_d \rho_a}} \tag{1}$$

where V_T is the terminal velocity, m_i is the mass of the particle, g is the gravity acceleration, k_a is the dimensionless coefficient of aerodynamic resistance, A_i is the projected or lifting area of the particle,d_i is the particle diameter, ρ_i and ρ_a are the particle and air density,C_d is the drag coefficient and can be calculated, as mentioned in Sect. 6. The drag coefficient is a dimensionless parameter of the particle that is used to quantify how easy or difficult it is for a particle to be entrained in the fluid flow [29]. It is related to the particle Reynolds number, which is given by Eq. (2)

$$Re_i = \frac{\rho_a d_i \left| v_a - v_i \right|_{max}}{\mu_a} \tag{2}$$

where R_{e_i} is the particle Reynolds number and μ_a is the dynamic viscosity of the air. Since the particle Reynolds number depends on terminal velocity, the calculation of terminal velocity is an iterative procedure. The following three flow regimes can be characterized based on particle Reynolds number: Stokes' regime when $R_{e_i} < 0.2$, intermediate regime when $0.2 < R_{e_i} < 1000$, and Newton regime when $R_{e_i} > 1000$ that will be described in detail in Sect. 6. Typically, the value of the drag coefficient C_d of spherical and cylindrical particles can be assumed 0.44 and 1.0,

respectively, in the range of Reynolds number of $R_e = 1000$ to 200,000 [22, 30].

Experimentally, the suspension or terminal velocity of particles can be determined by the suspension apparatus test, and it can be slightly differing from experiment to another depending on the grain material and the study condition [24, 31–34].

When applying aerodynamic principles to cereal grain crops, a method for expressing the projected area of the particle must be chosen because of the irregular shape of the particles. So, in most cases, the particles are assumed to be spherical, where the diameter of the particle could be taken as the diameter of a sphere of the same volume as the original size. In cases where the volume of the object is difficult to evaluate, the geometric mean diameter is a good approximation of the diameter of the equivalent sphere, provided that the shape factor is close to unity [26]. Theoretically, the net force acting on a particle moving in a fluid is defined by the difference between the drag and the gravitational forces, as shown in Eq. (3) [21].

$$F_{net} = \frac{1}{2} C_d A_i \rho_a V_a^2 - m_i g \tag{3}$$

where F_{net} is the net force acting on the particle, V_a is the velocity of the air.

1.3 Modeling Representations

Nowadays, improving the design and the performance of harvesting and post-harvesting devices such as combine harvester, grain dryers, spouted bed, aerodynamic separators, etc. becomes an urgent necessity for industrial needs. Experimental studies, mathematical models, and computer simulations are essential tools to solve this problem. With the current increase of computing power and technology, computational simulations are showing high adaptability to simulate the multiphase flow accurately. Numerical models have been used with some relevant modifications in recent and previous studies to describe the particulates matter and gas flow field inside the aerodynamic systems [35–42].

Since the bulk bio-particulate matter mass introduced to the structure domain, it is considered discrete elements, where each particle is an element, having an interaction with neighboring elements. Discrete Element Method (DEM) is a common and powerful numerical simulation technique for predicting and modeling this discrete media flow basis on Newton's laws of motion. The extensive usage of bio-particulate matter applications in industrial processing methods leads to several DEM articles development [43–51]. Computers with significant memories and a high-performance processor make it possible to simulate a large number of particles with a straight-forward approach. DEM can dynamically simulate each particle trajectory of dense phase flow by tracking its rotational and translational movement in the domain, taking into consideration the contact forces and the interaction couples of particle–particle and particle-boundary [35, 52, 53].

Practically, the particulate matters are introduced to the aerodynamic systems with air or gas flow; hence, it can be regarded as multiphase flow. Therefore, Computational Fluid Dynamics (CFD) models are mainly used to capture the air or fluid flow characteristics successfully with essential data in predicting the aerodynamic behavior [54–57]. For gas-particle flows, CFD multiphase models cannot be used to estimate the particulate matter phases; due to many restrictions happen when the dense flow is applied, those restrictions can be exceeded by coupling CFD with DEM [58]. This coupled process increases the computational time but enables a resolved particle–particle interaction combined

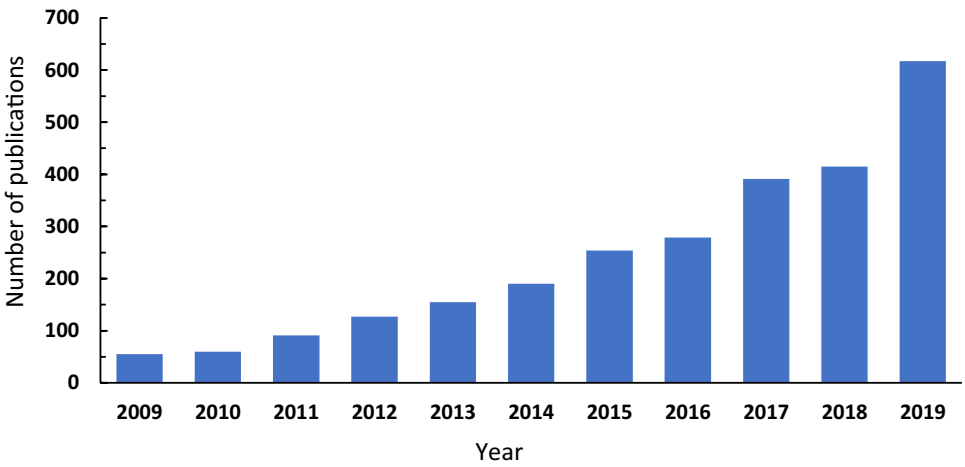

Fig. 1 Number of published works obtained from Science Direct using keywords: "CFD–DEM" (Accessed in December 2019)

with gas to solid and solid to gas modeled interactions as well.

1.4 Scope of this Work

In this decade, as illustrated in (Fig. 1), CFD–DEM coupling has become a hot research area for fluid-particles flow modeling, especially with the increase of computer technology progress and theoretical developments. However, previous reviews related to the bio-particulate matter field concentrated on DEM modeling [51, 59] or CFD technique [57] only; no reviews can be found on CFD–DEM coupling basics on modeling the bio-particulate matter in aerodynamic systems. However, these reviews did not concentrate on the force models related to fluid-particle interactions or the coupling ways between CFD and DEM for the bio-particulate matter. This paper is the first try aiming to provide a summary of the investigates based on computational simulations in the past two decades or so to open the way for the researcher to know the last working in these field. This information is important in the application of grain modeling in particle–fluid multiphase flows, and therefore, an extensive review is necessary.

The objective of this paper is to comprehensively review and collect the existing published research that used the coupling of CFD–DEM as a numerical technique for simulating the aerodynamic particulate systems related to the agricultural field. Firstly, this review summarizes the representations of the aerodynamic system in the agricultural process and industries, including some experimental works. Secondly, it represents the equations of particle motion and contacts force models between particles and interaction forces between particles and fluid in the aerodynamic systems as apart of DEM and CFD theories. Thirdly, drafts the CFD–DEM coupling ways, including theoretical developments and applications with a brief introduction of drag correlation models. Fourthly, introduces the applications of CFD–DEM modeling in aerodynamic systems and particle–fluid flow systems where the significant findings were discussed in some detail. Finally, the main challenges of CFD–DEM currently faces, and the exciting research topics for future studies are discussed. We conclude that CFD–DEM is an effective method for particle–fluid scale research in the aerodynamic systems related to the agriculture field. It also has a bright future as it offers a new way of understanding industrial processes and/or phenomena with practical particle shapes. However, there are still some aspects that are needed to be investigated in the future.

2 Theoretical Background of DEM

The DEM is considered one of the numerical modeling technique, which is first published by Cundall and Strack [60]. It is mainly developed to complement the finite element method to solve the complicated problems in engineering and applied science and investigating natural phenomena of granular flow of differently shaped particles that display sporadic conduct [61]. DEM simulations can also provide dynamic information which is extremely difficult or impossible to obtain by traditional experimentations, such as trajectories of, and transient forces acting on, individual particles, and analyze multiple, interacting, deformable, discontinuous, or fractured elements undergoing rotations and large displacements [59, 62]. With advanced computers, the simulations software reiterates the calculations million times during a second for each element of the system. Currently, the most advanced software and hardware allow simulations of processes with over a million particles, which facilitate the practicality of the DEM approach [63].

In DEM modeling, particle–particle interaction is treated as a dynamic process and solved by the explicitly numerical scheme. The contact forces, rotations, momentum, and displacements of a stressed particle are described by tracking each contact of the individual particles [64]. The primary assumption in the DEM is that every discrete element has different boundaries that physically separate it from every other element in the analysis. During the element movement in the domain, the translating and rotating behavior equations are applied on an element-by-element separately and the elements contacting through boundary forces. The deformation resulting from the collision can then be decoupled from the mean motion and written as the sum of the bodies' normal modes, which in turn gives a newly derived set of decoupled modal equations. These new equations are then solved by an explicit central difference scheme, where the final solution is obtained through modal superposition [59, 65].

Recently, the Discrete element method (DEM) application is gaining popularity in the harvest and postharvest processing of grain and highly utilized for many industrial processes, such as granular mixing, drying food, pharmaceutical industries, mining, and agricultural processing. The widely spread is because of its close and real characterization of actual conditions in predicting various processes [66]. Unlike the field of mining and the chemical industry, however, DEM is not widely applied in the agricultural processes because of various particle property issues arising from the biological origins of grain and food products.

In the agricultural industry, the DEM in agricultural and food processing applications have been considerably developed to describe; the flow in chutes and dryers [37,

67–69], the aerodynamic conveying systems [70, 71], the discharging silo [72], the transportation and compression of seeds [73], the dynamics discharge of particles in hoppers [74], the shaking separation of paddy and brown rice [75], the grain–straw separation screening in combine harvester [76, 77], the fluidization and spray drying of food powders [78], the grain transportation and aerodynamic separation [79], the grains segregation and seed motion in seed feeding device [80, 81], the screening separation of crop seeds [82, 83], and the mixing process in a bucket elevator [84]. DEM has also been useful in the modeling of interactions between soft materials: fruits such as grape [85], apple [86], or biomass [87]. A complete description and good over a review of the DEM can be found in much previous literature [51, 59, 65, 88, 89].

2.1 Approaches in DEM Modeling

In general, the granular dynamics modeling through DEM techniques can be classified into hard-sphere and soft-sphere approaches depending on the particle deformation during contact or collision [90]. The first concept of the "hard sphere" that comes to mind to simplify the collision modeling is to treat the particles as hard spheres; however, it is not necessary to describe the collision as entirely elastic. The word hard simply means that there is no interpenetration or deformation during the collision. In contrast, the word "soft" revolves around the deformation of spheres and the duration in contact. Figure 2 schematically indicates the main differences between these two modeling approaches [91, 92].

In the hard-sphere modeling approach, the effect of overlapping and deformation or interpenetration between particles during contact is assumed to be neglected [93]. So, this contact can be named as a non-smooth DEM where the particle's motion and the energy loss during a collision can be modeled through shock laws and the coefficients of restitution [94]. Collisions are also assumed to happen in a short time and may be assumed to be instantaneous; because the collision is limited between two particles only, one collision at a time, and does not consider multiple contacts [58]. So, different time steps will be applied, and the time step interval for the numerical solution varies with the time between each collision. Therefore, this approach is probably suited for rapid granular flow simulations, where the particulate material is partially or entirely fluidized [92].

In contrast to the soft-sphere approach, the overlapping at the contact points is allowed, and the contact forces between particles are strongly considered [62, 91]. Herein, it is essential in this approach to model the forces of elastic restitution and friction that happened during the collision of the particles [95]. Because of the nature of the iterative schemes used in the soft-sphere approach, it is susceptible to the time step. Therefore, the time step interval is assumed constant during simulation [93] and should be smaller than the duration of contact for stability considerations [96]. Usually, in most soft- sphere models, the duration of the contact is artificially increased by allowing softer interaction and hence reducing the required CPU time. The obtained deformation due to the collision can be considered similar to that occurs at the contacts among bio-particles. These deformations are used to calculate elastic, plastic, and frictional forces between particles [59]. Hence, this approach highly used in particulate mechanics models related to agricultural cereals and crops. The motion of particles in this approach is described through numerical integration of the Newtonian equations of motion. Apart from external forces acting on the system, the interparticle forces are of crucial importance to these models [38, 97]. The magnitude of the overlap can be related to the interparticle contact force, as discussed subsequently.

The significant advantage of soft-sphere models is that they can model the dense-phase bulk granular materials regarding the multiple particle contacts [98], which is essential when modeling quasi-static systems [62]. These models start by solving the equations governing the linear translation and rotational motions of particles [92]. While in hard-sphere models, the interaction forces are assumed to be impulsive, and hence the particle modeling strategy starts from the equations governing momentum exchanges [93].

However, hard-sphere approaches are computationally cheap, fast, and preferred for non-dense flow; it can give a limited description of the dense material's response involving multiple simultaneous contacts [99]. Therefore, given the advantages of soft-sphere approaches mentioned above for describing the bulk material physics, where it is most

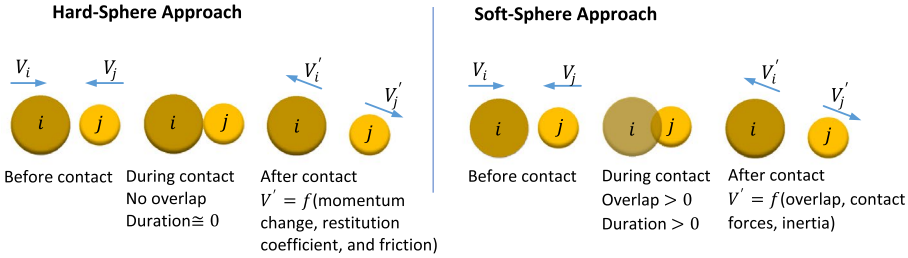

Fig. 2 Illustration of hard-sphere and soft-sphere approaches [91, 92]

commonly used in the grain and food processing industries, no further consideration of the hard-sphere algorithms is given in this study. Thus, soft-sphere modeling is called DEM (Discrete Element Method or Distinct Element Method) [100], which is the scope of this review.

2.2 Governing Equations of Motion

In soft-sphere DEM modeling, the motion of each particle can be tracked by calculating the contact forces and displacements using an explicit numerical scheme and a very small time step [60]. The particle movements can be divided into two parts: the translation motion calculated by the basic's equations of Newton's second law as shown in Eq. (4), and rotation motion described by Euler's law as formulated in Eq. (5) [101–103]. In general, the spaces between the particles are filled with interstitial fluid, usually air in aerodynamic systems. When that fluid forces the particles, the effect of this interstitial fluid should be taken into account. Nevertheless, if the particles are considered to be large and heavy, they are exempt from the effects of the interstitial fluid [98, 104].

$$m_i \frac{d^2}{dT^2} x_i = \sum_{j=1}^{n_i^c} F_{ij}^c + F_i^g + F_i^f + \sum_{k=1}^{n_i^c} F_{ik}^{nc} \tag{4}$$

$$I_i \frac{d^2}{dT^2} \Phi_i = \sum_{j=1}^{n_i^c} M_{ij} + M_{rij} \tag{5}$$

where m_i is the particle mass,x_i and Φ_i are the position and the orientation in the space of particle i, respectively,F_{ij}^C the total contact force, M_{ij} is the momentum acting on particle i by particle j or wall,f_i^g is the gravitational force, F_i^f is the fluid-particle interaction force on the particle i, M_{rij} the momentum generated by rolling friction when the particle rotates in a fluid which will be represented in Sect. 5, F_{ik}^{nc} is a term of non- contact force acting on particle i by particle k or other sources, and I_i is the moment of inertia of particle i, and T is the time.

The contact between two particles is not taken place at a single point but on a specific area, which can lead to making the particles slightly overlapping on the normal and tangential coordinates (n and t) [62]. Particle overlapping cannot be neglected because it can significantly affect the simulation result [105]. So, the total contact force acting on the particle at the contact plan can be analyzed on n and t coordinates which can be mathematically calculated according to Eq. (6). In addition, (Fig. 3) indicates a schematic illustration of the typical contact force vectors with overlapping and torques implicated in a soft-sphere DEM modeling.

$$F_{ij}^C = F_{ij}^n + F_{ij}^t \tag{6}$$

where F_{ij}^n and F_{ij}^t are the normal and tangential contact forces on the particle i by contacting particle j, respectively.

2.3 Modeling of Contact Force

In any granular flow, forces are mainly generated by interparticle contacts that can be mechanically described by how the particles "see" one another. The philosophy of DEM is to use rigid springs, acting both normal and tangentially to the contact plane to calculate the interparticle forces. Although DEM simulations are worked efficiently in predicting many processes in the agricultural industry, it requires a detailed understanding of the interactions between particles under various loads.

Precise values of physical and mechanical parameters of granular materials that have biological origins are considered critical parameters for modeling contact models of DEM [106]; due to the high moisture content of these particles, which makes the deformability to be high during contact [51]. As such, different contact models can be generated and developed based on elastic, viscous, plastic, dry friction, and adhesive interactions.

Usually, the main assumptions of the theoretical contact models are considered the particles to be isotropic and elastic, where the contact is completely smooth. It is a beyond contradiction that the bio-particulate matters are varied in

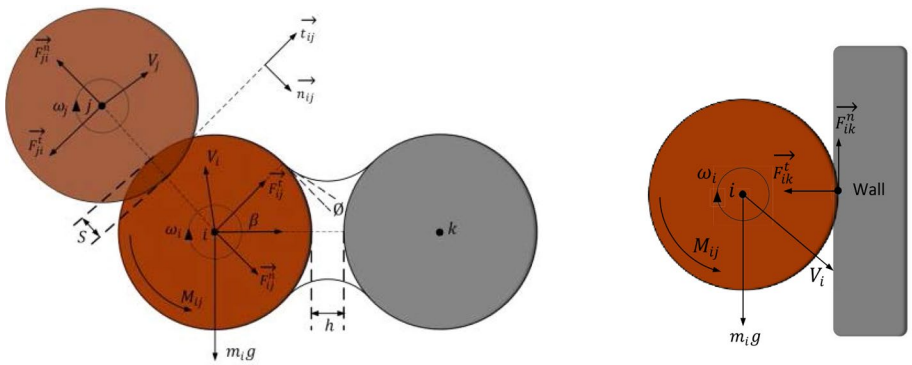

Fig. 3 Contact forces analysis during the collision of the discrete particles considering the overlapping [35, 105]

geometry and shape. Most of them have a convex shape, while others are spherical in shape, but none of them are purely elastic bodies [51]. Therefore, the application and the development of contact models for biomaterials related to the agricultural field face many restrictions.

The contact forces in any DEM code consist of forces normal-to-contact plane and force tangent-to-contact plane. For spherical particles, the contact plane is perpendicular to the line that connects the centers of two spheres. For non-round particles, the methodology for determining a contact plane is more complicated. It can be determined by the closest points of two particles or the closest points of a particle and triangle or the two points with the maximum overlap distance in the case of a physical contact [107]. This chapter will introduce the standard contact models and the interaction properties, including coefficients of restitution, static and rolling friction, plastic or viscous damping, and adhesion used by investigators for the bio-particulate matter.

2.3.1 Normal Force Modeling

The primary requirements to model the normal contact force are that the force should have to be repulsive, and the model has to allow significant energy dissipation. For this purpose, several investigators developed many models to describe the behavior contact of the granular medium systems.

2.3.1.1 Hertzian Contact Model Following the work of Hertz in the nineteenth century and the theory of elasticity [108, 109], the normal contact force is modeled by considering the response of two elastic spheres in contact over a small circular contact area. This model has been widely used to determine the modulus of elasticity for various agricultural grains that have a convex shape [110]. It is usually called as a Hertzian spring dashpot model where the normal contact force is modeled as the sum of an elastic force and a damping force. When considering the overlapping during contact, the model can be expressed mathematically in an incremental way, as shown in Eqs. (7, 8, and 9).

$$F_{ij}^{n} = \frac{4}{3}E^{*}\sqrt{R^{*}S^{n^{3}}} + \eta\left(\frac{4}{3}m^{*}E^{*}\sqrt{R^{*}S^{n}}\right)^{1/2}\frac{d}{dT}S^{n} \tag{7}$$

$$\frac{1}{E^{*}} = \frac{\left(1-\nu_{i}^{2}\right)}{E_{i}} + \frac{\left(1-\nu_{j}^{2}\right)}{E_{j}} \tag{8}$$

$$R^{*} = \frac{R_{i}R_{j}}{R_{i}+R_{j}} \tag{9}$$

where E^{*} and R^{*} are Young's modulus equivalent and radius, E_i, E_j, and ν_i, ν_j are Young's moduli and Poisson's ratios of the two contacting spheres of radii R_i, R_j,S^n is the normal overlapping, η is called a damping ratio, which is a dimensionless parameter related to the restitution coefficient that can be calculated as expressed in Eq. (10) [44, 111].

$$\eta = -\ln\varepsilon\sqrt{\frac{5}{ln^{2}\varepsilon+\pi^{2}}} \tag{10}$$

where ε is the coefficient of restitution defined by DEM user according to the studying case and m^{*} is the equivalent mass for the particles in contact and can be calculated according to Eq. (11).

$$\frac{1}{m^{*}} = \frac{1}{m_{i}} + \frac{1}{m_{j}} \tag{11}$$

2.3.1.2 Elastic–Plastic Contact Model This model was first introduced by Walton and Braun [112] and named as a Hysteretic Linear Spring Model [113, 114]. This elastic–plastic or repulsive-dissipative normal contact model allows simulation of the plastic energy dissipation on contact without introducing the overhead of long simulation times. Besides, the energy dissipation is not considered the velocities of the neighboring particles and loading rate that makes the energy dissipation insensitive to other contacts. Furthermore, the coefficient of restitution is velocity independent, and it can be accurately modeled the compressible materials with correctly simulating the non-adhesive particles flow [35, 52, 53, 115]. The following equations starting from Eqs. (12–17) draw and describe mathematically one by one the linear hysteresis model used in DEM code [29, 107, 116–118]

$$F_{i}^{n,T} = \begin{cases} \min\left(F_{i}^{n,(T-\Delta T)} + K_{u}^{n}\Delta S^{n}, K_{l}^{n}S^{n,T}\right), & \text{if } \Delta S^{n} \geq 0 \\ \max\left(F_{i}^{n,(T-\Delta T)} + K_{u}^{n}\Delta S^{n}, 0.001K_{l}^{n}S^{n,T}\right), & \text{if } \Delta S^{n} < 0 \end{cases} \tag{12}$$

$$\Delta S^{n} = S^{n,T} - S^{n,T-\Delta T} \tag{13}$$

where $F_i^{n,T}$ and $F_i^{n,(T-\Delta T)}$ are the normal elastic–plastic contact forces acting on the particle i at the current time T and at the previous time $T-\Delta T$ respectively, where ΔT is the timestep, ΔS^n is the change in the overlapping during the time step, $S^{n,T}, S^{n,T-\Delta T}$ are the normal overlap values at the current and at the previous time, respectively, K_u^n and K_l^n are the unloading and loading contact stiffnesses, respectively.

Note that the unloading force is limited by the value of $0.001K_l^nS^{n,T}$ to ensure that the normal force becomes zero with zero overlappings. A schematic sketch, as shown in (Fig. 4) can demonstrate the overlapping circle (*A*–*C*) of loading and unloading response due to the normal force effect

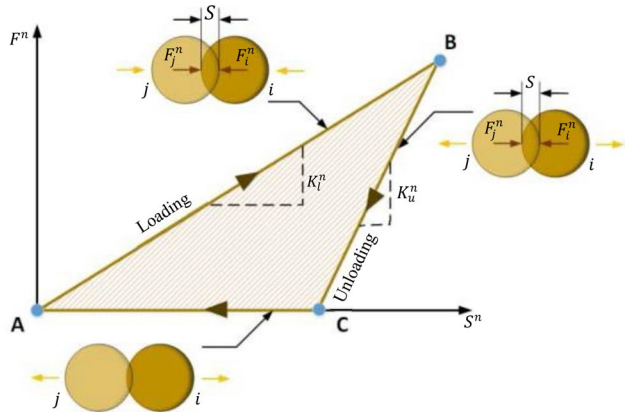

Fig. 4 Normal force–overlapping response for the hysteretic linear spring model [35, 107]

where the hatched area is represented the energy dissipation during the particles contact. Besides,K_l^n and K_u^n are the slope of loading and unloading lines, respectively, and the plastic deformation only happens during the contact of the particles i and j; after that, the residual deformation neglected.

The coefficient of restitution can be determined by the user, which represents the energy dissipation due to particle–particle or particle–wall contact; also, the loading and unloading stiffness represented in Eqs. (14 and 15) can be taken into account by considering the valve of Young's modulus and the particle geometry.

$$\frac{1}{K_l^n} = \begin{cases} \frac{1}{K_{li}^n} + \frac{1}{K_{lj}^n} & \text{Particle - Particle} \\ \frac{1}{K_{li}^n} + \frac{1}{K_{lw}^n} & \text{Particle - wall} \end{cases} \tag{14}$$

$$K_u^n = \frac{K_l^n}{\varepsilon^2} \tag{15}$$

whereas:

$$K_{li}^n = E_i Z \tag{16}$$

$$K_{lk}^n = E_w Z \tag{17}$$

where E_i and E_w are Young's modulus of particle and boundary, respectively, and Z is representing the particle size or geometry. This model should be applied to adequately selected individual cases of the behavior of dry and hard seeds with the elastic behavior in the normal direction, such as the application of discharging silo with rapeseeds and the aerodynamic systems of seeds and foreign materials separation [35, 72].

2.3.1.3 Visco-Elastic Contact Model The simple model to describe the Visco-elastic behavior of the particles is called a linear elastic, viscous model. The advantage of this model

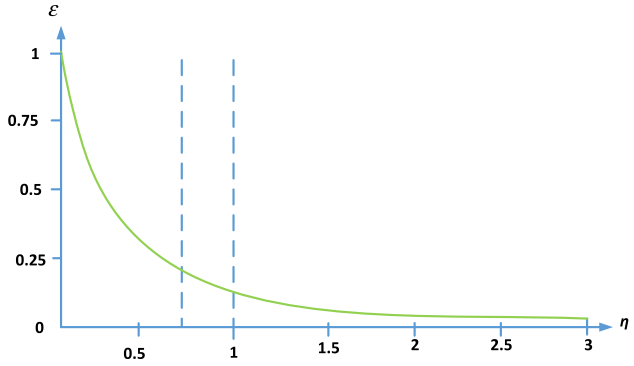

Fig. 5 The relationship between damping ratio and the restitution coefficient [107, 120]

is that it takes less time and machine resources to process but provides less accurate results compared to the hysteretic linear spring model [107]. When Visco-elastic particles are in contact, the normal contact force is given by the sum of elastic repulsive force and a damping force proportional to the velocity as formulated in Eq. (18) [51, 119].

$$F_i^n = K_l^n S^n + C^n \frac{d}{dt} S^n \tag{18}$$

where C^n is the normal damping coefficient and defined as follows in Eq. (19).

$$C^n = 2\eta \sqrt{m^* K_l^n} \tag{19}$$

where the relationship between the damping ratio and the restitution coefficient can be described in Eq. (20) [120]. In detail, (Fig. 5) describes the relationship between the damping ratio and restitution coefficient given by Eq. 19. The graph is showing the increase of damping ratio when the restitution coefficient decreased; because of the inverse relationship between the two parameters.

$$\varepsilon = \begin{cases} exp\left[-\frac{\eta}{\sqrt{1-\eta^2}}\left(\pi - arctan\frac{2\eta\sqrt{1-\eta^2}}{1-2\eta^2}\right)\right] & if\ 0 \le \eta < \frac{1}{\sqrt{2}} \\ exp\left[-\frac{\eta}{\sqrt{1-\eta^2}}\left(arctan\frac{2\eta\sqrt{1-\eta^2}}{1-2\eta^2}\right)\right] & if\ \frac{1}{\sqrt{2}} \le \eta \le 1 \\ exp\left[-\frac{\eta}{\sqrt{\eta^2-1}}\left(\ln\frac{2\eta\sqrt{1-\eta^2}}{1-2\eta^2}\right)\right] & if\ \eta > 1 \end{cases} \tag{20}$$

For soft biological materials such as apple, potato, and tomato, etc. in addition to the soft and high moisture content of seeds, Visco-elastic contact model is efficient and appropriate to predict the energy dissipation and the impact reaction [121, 122]. While for dry and hard seeds such as rapeseed, the Elastic–plastic contact model works well to estimate the contact and impact behavior [72].

2.3.2 Tangential Force Modeling

2.3.2.1 Linear Spring Coulomb Model This model named by the Linear Elastic-frictional model; because of its elastic behavior before the friction commencement, and it can regenerate Coulomb frictional contact behavior for static and dynamic frictional values. During the tangential contact, the particle sliding plays a vital role in determining the total tangential contact force, where Eq. (21). can express this effect [29, 53, 118].

$$F_i^{t,T} = min\left(F_i^{t,(T-\Delta T)} + K_l^n \Delta S^t, \mu F_i^{n,T}\right) \tag{21}$$

where $F_i^{t,T}$ and $F_i^{t,(T-\Delta T)}$ are the tangential contact forces at the current and previous time of the simulation, respectively,ΔS^t is the change in the tangential overlapping during the time step, and μ is the friction coefficient which can be defined as a static and dynamic coefficient (μ_s, μ_d) depending on the tangential sliding contact, as shown in Eq. (22) [29, 117].

$$\mu = \begin{cases} \mu_s & \text{if no sliding at the contact} \\ \mu_d & \text{if sliding act at the contact} \end{cases} \tag{22}$$

When the tangential force exceeds the limit of $\mu_s F_i^{n,T}$ The sliding is considered to be taking place on the contact. Once that force falls below the value of this value, the contact is considered non-sliding again. This model applied effectively and shoe a high validity to separate jojoba seeds from its leaves using cyclonic separation process [35] and for vertical pneumatic separation of sugarcane bagasse particles [29].

2.3.2.2 Mindlin-Deresiewicz Model This model is called the elastic-frictional contact model, which is first derived from the mathematical analytic of elastic spheres in contact under varying oblique forces [123]. It is mainly consisting of simple loading histories of varying normal and tangential forces and a minimal range of tangential displacement between the contacting spheres [124, 125]. The tangential force in this model is given by Eq. (23) [107]:

$$F_i^{t,T} = \mu F_i^n \left[1 - \left(1 - \frac{min\left(|s^t|, s_{max}^t\right)}{s_{max}^t}\right)^{3/2}\right] \frac{s^t}{|s^t|} + \eta^t \left(\frac{6\mu m^* F_i^n}{s_{max}^t} \sqrt{1 - \left(\frac{|s^t|}{s_{max}^t}\right)}\right)^{1/2} \left(\hat{n}_c \times \frac{d}{dT} S^t\right) \times \hat{n}_c \tag{23}$$

where s^t is the tangential relative displacement at the contact, $\hat{n}_c$ is the unit vector in the normal direction at the contact, η^t is the tangential damping ratio and is estimated using Eq. (24), s_{max}^t is the maximum relative tangential displacement at which particles begin to slide as can be formulated in Eq. (25), and $\frac{d}{dT} S^t$ is the relative tangential velocity at the contact.

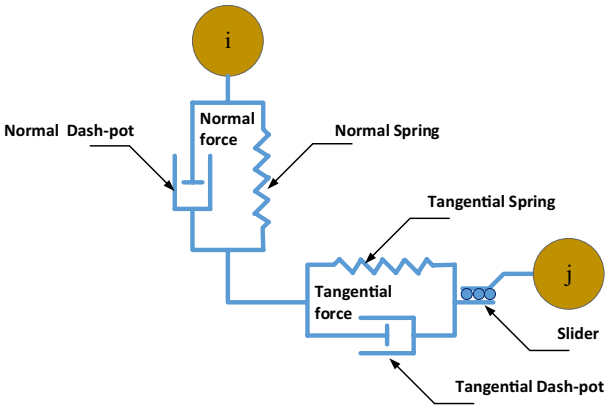

Fig. 6 Hertz-Mindlin contact model with viscous damping and frictional slider in the tangential direction [35]

$$\eta^t = -\ln \varepsilon \frac{1}{\sqrt{ln^2 \varepsilon + \pi^2}} \tag{24}$$

$$s_{max}^t = \mu \left(\frac{1 - \nu_i}{2 - \nu_i} + \frac{1 - \nu_j}{2 - \nu_j}\right)^{-1} S^n \tag{25}$$

The Mindlin–Deresiewicz model does not work appropriately with rolling resistance models for non-spherical particles. Therefore, when the Mindlin-Deresiewicz model is selected with non-round particles, the rolling resistance must be neglected [107]. This model was improved to be suitable in simulating soybeans flowing down an inclined chute [68]. In this simulation, the soybeans (non-spherical particles) are represented by clusters of spheres to simplify contact detection, and the modeling showed a good agreement with the experimental data. The frictional contact model of spherical particles was also developed based on the Mindlin-Deresiewicz model to predict the particle–particle slip and the sliding of stainless steel beads, pea, and rapeseed [126].

2.4 Tangent Stiffness Model

Hertz-Mindlin contact model is usually used to represent the tangent stiffness model, which is applied in DEM applications as the primary law to calculate particle interaction forces in the tangent directions [44, 123, 125]. It is also named as a linear spring-dashpot model that includes springs, dashpots, and frictional sliders, as shown in

(Fig. 6) [127]. This model combining Hertz's theory [109] to describe normal stiffness and Mindlin and Deresiewicz's theory [123] to describe tangential stiffness. These stiffnesses were calculated as mentioned in the above sections by assuming the presence of elastic springs and dashpots in the normal and tangential directions. The spring stiffness, dashpot coefficient, and friction sliders are expressed through Young's modulus parameter, friction coefficient, and coefficient of restitution, respectively [39, 116, 128].

This model is applied intensively to model and predict the interaction of bio-particulate matter, including seeds and grains. The calibrations and validations showed high reliability of this model, which is presented a high prediction of the particle's behavior. For an instant, simulating the motion of rice grain and short straw in air-and-screen cleaning device [39], simulating the flow of corn-shaped particles in spouted bed [40], simulating of rapeseed and wheat grain motion in seed feeding device [81], predicting the corn grain flow behavior in a commercial screw auger [129], simulating the motion of rice grain and rice straw in a variable-amplitude screen box [76], and optimizing the air-blowing maize precision seed-metering device [42], etc.

2.5 Adhesion Contact Model

In order to separate bodies in intimate contact; mechanical work must be expended to overcome the adhesive forces. They have appeared in beddings of biological materials that have an amount of moisture content, and its effect is shown in agglomeration of powders and small size particles that may create problems for storage and handling [130, 131]. In order to capture this behavior numerically, the normal repulsive force has to be supplemented by the attractive normal force to predict its flow characteristics accurately [107]. Adhesion between biological particles not only acts because of moisture content but van der Waals forces, electrostatic forces, or liquid bridges effects as well [132]. Liquid bridge force plays a vital role during modeling particles more significant than a fraction of millimeter-scale, which arises from the capillary pressure in the bulk of the liquid and the sum of the surface tension of the liquid [119, 133]. This force value depended on some significant aspects, such as space area between particles, the surface tension of the liquid, geometry and the volume of the bridge, and contact angle between the liquid and solid surface [134].

The most common and popular model for representing the adhesive behavior is developed by Johnson-Kendall-Roberts (JKR) [135]. This model introduces the effect of adhesion into the Hertzian contact model, where the contact area between two particles is slightly larger than the one predicted by the Hertzian theory. This surface energy term is added to the total energy of the system [107]. The normal JKR adhesive model force can be calculated according to Eq. (26) [107]:

$$F_{i_{adh}}^{n,T} = \frac{E^* a^3}{6R^*} \tag{26}$$

where $F_{i_{adh}}^{n,T}$ is the normal adhesive contact force at the current time, a is the separation distance of contact between particles or between a particle and a boundary, as shown in (Fig. 7), where it is related to the normal overlap using the expression introduced in Eq. (27) [51, 107]:

$$S^n = \frac{a^2}{4R^*} - \left(\frac{\pi \Gamma a}{E^*}\right)^{1/2} \tag{27}$$

where Γ is the surface energy and can be used to calculate the maximum liquid bridge tensile force that occurs between two particles as formulated in Eq. (28) [119]:

$$P_{max} = -2\pi \Gamma E^* \tag{28}$$

where P_{max} is the maximum liquid bridge tensile force since the effect of its behavior can be observed through the DEM simulation of the particle's free-flowing and the discharge rate from hoppers of different inclinations [74, 136]. Another study was performed on agricultural material and reported that the maximum liquid bridge tensile force between wet rapeseeds is approximately tenfold of the seed weight, which means that cohesive behavior can occur in the case of some millimeters of particles' size [51].

The JKR model has a strong theoretical basis and is widely accepted for adhesive elastic sphere particles. Since the surface energy can be measured experimentally, this model could be used without calibration, in principle, for simulating perfect spheres [107].

On the other hand, when adhesion between particles is due to liquid bridge forces (big attraction between the polar molecules of water), another adhesive model was used, namely the constant adhesive force model [29, 127]. This model depends on two significant aspects: the

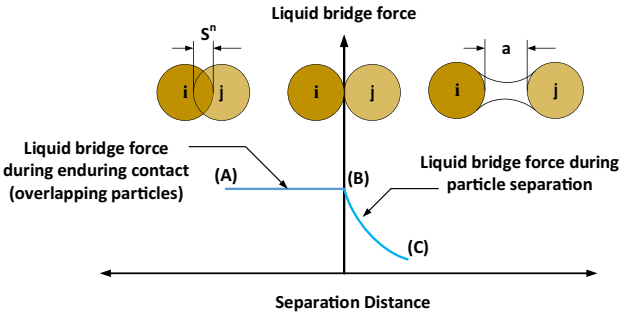

Fig. 7 Schematic diagram of the liquid bridge force as a function of the separation distance between two particles [74]

minimum distance between particles or particles and a boundary before the adhesive forces applied and the force fraction expressed as a function of the particle gravity force. Hence, it means that since the force fraction reached 1, the adhesive force will be equal to the gravity force applied to the particle. In the case of contact between two particles of different masses, the smaller mass is considered for the calculation of gravitational force [107], as described in Eq. (29):

$$F_{i_{adh}}^{n,T} = \begin{cases} 0 & if - \Delta S^n > \delta_{adh} \\ f_{adh} \times g \times min\left(m_i, m_j\right) & if - \Delta S^n < \delta_{adh} \end{cases} \quad (29)$$

where f_{adh} and δ_{adh} are the force fraction and the adhesive distance, respectively. Note that, when $\Delta S^n \geq 0$ the particles start adhering to each other, but if $\Delta S^n < 0$ the particles separate [127]. This model is applied effectively to represent the adhesion force of sugarcane bagasse particles during the pneumatic separation [29].

3 Modeling of Particles

The granular material is introduced in many fields of industries such as chemistry, agricultural processing, civil engineering, but their behavior is not yet well understood. Even though a pile of particles will behave like a porous solid, it will flow like a liquid if it is put on an inclined plane. Nevertheless, if it subjected to significant vibrations, it would have a gas-like behavior. These behaviors of granular solids were first described in an old proverb (ca. 98–55 B.C.) as "One can scoop up poppy seeds with a ladle as easily as if they were water and, when dipping the ladle, the seeds flow in a continuous stream" [95]. To model granular materials correctly, the shape is not only required but physical properties, which include size, density, moisture content, etc. should be taken into consideration and determined individually for each particular DEM modeling application as well [106].

Generally, realistic modeling of the particle shape in simulations plays an essential role in emulating real processes [137–140]. The Bio-granular materials, such as grain, seeds, tubers, and soft fruits have a considerable difference of shapes, from spherical (e.g., rapeseed), ellipsoidal (e.g., rice) and diamond with round (e.g., corn) or sharp-edged (e.g., buckwheat), to very complex, non-convex shapes of fruits and tubers [51]. The dimensions of these materials can vary from below an mm to tens of cm, which gives it a significant consideration during modeling. Although measuring the three dimensions: length, width, and thickness of the particles is very important for modeling, the roundness of edges and a ratio of the dimensions should also be determined especially to describe the complex shapes [106, 141].

Real particles are almost non-spherical, so they are rarely used in simulation studies due to difficulties in representing these shapes in simulations' software [137]. Early, particles in DEM simulations were modeled as discs and spheres; because the direction of the normal contact forces is always toward the center, and the particles' rotation is only affected by tangential contact forces [142]. Athanassiadis et al.[143] reported that the particle shape has a strong influence on the mechanical response and the interaction forces of granular material, particularly on stiffness and yielding parameters. They obtained this quote based on an experimental work carried out on fourteen particle geometries where all are in three dimensions (3-D) printed from the same material. The work includes several shapes, such as sphere, tetrahedron, cube, octahedron, dodecahedron, icosahedron truncated, tetrahedron, triangular bipyramid, tetrahedral frame, and jacks with arm length. Not only the particle size, shape, physical and mechanical properties are regarded as a big challenge for operating the DEM simulation modeling but the computing power, time-consuming, and the number of discrete particles in the system as well [59, 106, 143].

Complex shapes or non-spherical particles which are very common in the bio-particulate matter are often modeled on DEM as the multi-sphere approach [124, 137, 144, 145]. In this method, the particle shape is made by assembling a different number of spherical particles together, which in turn increases the computational speed and increasing the accuracy to determine the interaction between spheres [145]. The multi-sphere approach was ideally used to model the shape of bio-particles such as soybean [106, 124], corn [40], rice [146], wheat [69], pea, and bean [147]. The Accuracy of the particle behavior prediction is influenced by the number of sub-spheres combined. In the case of a small number of sub-spheres (≤ 9), the particles interpreted as interlocked, if higher than that it may be simply classified as a decrease of roughness when the number of sub-spheres increases [148].

Advanced approaches were developed to model more complex particle shape in DEM using 3-D shapes, such as ellipsoidal [149–151], super-ellipsoid [152–154], sphero-cylinders and capsules [41, 155, 156], superquadric [157–159], bonded particles [160–163], polyhedral [35, 164, 165] and polygonal [166–168]. Applying these advanced approaches needs a precise determination of the contact point, and normal and tangential contact vectors [51, 169].

Table 1 summarized the developed particle shape models used for predicting the behavior of most common agricultural cereal grains. As presented, the multi-sphere approach is commonly used where the best number of spheres to represent a single grain, or a seed kernel has not been confirmed yet. This leakage is because of the complicated shape of agricultural grains, and the presence of the surface crease makes it challenging to develop a particle with identical shapes. So, the number of spheres should be approximated

Table 1 Grain models used for DEM simulation

Grain type	DEM model/Reference	Particle shape	Research representations and investigations
Soybeans	2-D single-circular disc model [82]	Circular disc	Simulate the separation of soybeans and mustard seeds using a sieve device under the condition of feeding rate and bed depth
	3-D 4-sphere model [170]	Ellipsoid	Simulate the behavior of a single soybean kernel bouncing in aluminum, glass, and acrylic surfaces to measure the coefficient of restitution with high accuracy
	3-D 4-sphere model [124]	Ellipsoid	Predict the dry flow of soybean in a chute device comparing with experimental data
	3-D 4-sphere model [68]	Ellipsoid	Simulating soybeans flowing down on an inclined chute with a bumpy bottom to predict the flow velocity and force statistics of the soybean during flow
	Comparison of 3-D 1-sphere, 2-sphere, 3-sphere, and 4-sphere model [106]	Sphere & ellipsoid	Developing a particle model with appropriate parameters of coefficients of restitution, static friction, rolling friction, particle size distribution, and particle shear modulus that best matched the property values available in the literature. The best model is a single-sphere particle model that can correctly simulate soybean kernels in the bulk property tests
	Comparison of 3-D 5-sphere, 9-sphere, 13- sphere model [171]	Ellipsoid	Developing a particle model to analyze the discharging process of a silo. The result of the 5-sphere model was the best for modeling the soybean seed particle, which verified the feasibility and validity of the modeling methods of soybean seeds
Rice	2-D single circular model [75]	Circular element	Modeling paddy and brown rice kernels in the shaking separation process comparing with an experiment on the same scale
	3-D triaxial particle model [142]	Ellipsoid	Simulating the impact behavior against the grain loss sensor. The DEM results were similar to experimental data, which provide evidence for optimizing the grain loss sensors design for accurately identifying rice seed impact signals
	3-D 11-sphere model [146]	Ellipsoid	Simulating the filling and discharge flow and piling of the rice kernels with rolling friction coefficients of zero and 0.3. Considering the rolling friction, the pile shape is similar to the actual pile. While, without rolling friction, particle mobility was higher, resulting in a spread of particles rather than a pile
	3-D 7-sphere model [172]	Ellipsoid	Predicting the impact behavior of rice kernels on the impact board of an inclined elevator head with high accuracy
	3-D single-spheroid model [39]	Spheroid	Simulating the separation process of rice kernels and straws using a coupled DEM and CFD model in an air and screen cleaning device

Table 1 (continued)

Grain type	DEM model/Reference	Particle shape	Research representations and investigations
Corn	Comparison of 3-D 1-sphere, 2-sphere, 5-sphere, and 13-sphere mode [129]	Sphere & cluster shape	Studying the influence of corn shape and the interaction effects of DEM parameters such as coefficients of static and rolling friction. The developed models were validated and calibrated by comparing the flow rate and corn pile with experimental tests of commercial screw auger. It is showed that the 2-sphere model is the best DEM corn shape model
	2-D 2-disc clump model [173]	Disc	Modeling the internal friction angle and stiffness of grains where the calibration process validated by modeling silo discharge and bucket filling
	Bonded particle model (BPM) [42]	Spheres	Simulating and optimizing the air-seeds flow in the aerodynamic seed-metering device using CFD–DEM. The model is reliable as a tool for understanding the physical phenomenon of seed movement in the gas phase and can be applied successfully to analyze the sources of difference
	3-D 4-sphere model [174]	Cluster autonomous shape	Simulating the influence of the gravitational field on the bulk responses of the corn seeds under three different loadings
	3-D 6-sphere model [175]	Cluster autonomous shape	Studying the pressure distributions, bulk density distributions, and flow properties during filling and emptying of silos
	Comparison of 3-D single-sphere, 4-sphere, 6-sphere 8-sphere, and 12-sphere model [176]	Cluster autonomous shape	Developing the most accurate modeling shape considering the rolling friction effect using the calibration of silo discharging. Depending on the required accuracy, the approach of 6 sub-spheres could be sufficient to represent the shape of the grain of maize

Table 1 (continued)

Grain type	DEM model/Reference	Particle shape	Research representations and investigations
Rapeseed	3-D single-sphere model [81]	Sphere	Simulating rapeseed and wheat motion using a coupled of DEM and CFD model in seed feeding device at different air velocities. The model can correctly predict the physical phenomenon of seeds movement in the airflow field
	3-D single-sphere model [72]	Sphere	Predicting the rapeseed flow through a horizontal orifice using different contact models. The result showed that contact models give the same behavior for slow particle flow comparing to experimental results but needed some improvement, including dissipation for higher particle flow rates
	3-D single-sphere model [73]	Sphere	Simulating the deformation under bulk compressive loading of rapeseeds that there was a little deviation in the initial particle positions between the experiment and simulation
	3-D single-sphere model [177]	Sphere	Investigating the influence of the moisture content of rapeseeds on the physical properties of grain bedding during uniaxial compression testing. Both the simulations and experiments showed differences in the elasticity and the stress transmission at various grain moisture contents. Besides, the mechanical response is significantly affected by the moisture content of kernels
	3-D single-sphere model [178]	Sphere	Simulating the free fall and impact of rapeseeds against a flat surface using different contact models and moisture content
	2-D single circular disc model [179]	Circular disc	Modeling the bulk behavior of rapeseed during a direct shear test to determine the influence of three different levels of the coefficient of interparticle friction

Table 1 (continued)

Grain type	DEM model/Reference	Particle shape	Research representations and investigations
Wheat	3-D 3-sphere model [67]	Cluster shape	Predicting the velocity distribution of wheat kernels in a mixed-flow dryer where the obtained velocity was nearly accurate to the real
	Comparison of 3-D single-sphere, 4-sphere, and 8-sphere model [180]	Cluster autonomous shape	Comparing the performance of different particle models in predicting the angle of internal friction and cohesion of wheat using both linear and nonlinear contact models. The single-sphere particle model behaved better in the simulations than the multi-sphere models. Also, 3-D particle models have higher accuracy in predicting the bulk behavior of wheat than a 2-D approach
	2-D single circular disc model [181, 182]	Circular disc	Investigating the wheat velocity, moisture content, and residence time distributions in a mixed-flow dryer. The DEM can adequately predict the main features of particle flow comparing to the experimental results
	2-D 5-disc ellipsoidal clump model [69]	Ellipsoid	Evaluating the traditional designs of mixed-flow dryers with different air ducts by coupling CFD–DEM to discover design deficits. The model can predict the real flow pattern, but not produce the expected dynamic angle of repose that typically formed under the air ducts
	Comparison of 3-D single-sphere, multi-sphere model [183]	Sphere & kernel shape	Modeling the wheat in the first break milling process at different moisture content. The sphere-shaped model had a substantial deviation from the experimental milling results. However, the two shaped models were able to predict the trend observed for change in particle size of the first break stream with moisture content
Other			
Jojoba & leaves	Spherical and custom polyhedron shape [35]		Modeling Jojoba seeds and its leaves as a spherical and custom polyhedron shape to investigate the separation process using cyclone separator and applying the coupling of CFD–DEM. The model can ideally use to optimize cyclone geometry resulting in improving the performance
Bagasse particles	Rounded cylinder shape [29, 52]		Investigating theoretically the bagasse particle separation process in a pneumatic cylinder device using CFD–DEM in order to optimize the machine used for that purpose

by trials depending on the computation time and prediction accuracy required.

4 Theoretical Background of CFD

At present, Computational Fluid Dynamics (CFD) is frequently used in the simulation of the internal or external flow field of several fluid systems [184]. It is continued to expand the scope of application and offers new ways to solve practical engineering and agricultural problems. It can predict and provide a qualitative and sometimes even quantitative prediction of fluid flows via mathematical modeling (partial differential equations), numerical methods such as finite volume method, and software tools by solving the transport phenomena equations of mass, momentum, and energy [54, 185]. It has been widely used in industry to optimize processes, reduce the energy costs, create new designs without wasting resources by carrying out experiments, and predict fluid flow in several processes such as mixing, drying, separation, and fluidized bed granulators [186].

Usually, to drive the continuum flow pattern in the presence of a secondary particulate phase, the system domain is discretized in small grid cells where the volume-averaged Navier–Stokes–Equations governed the fluid phase motion [53, 102, 103, 187]. These 3-D governing Eqs. (30 and 31) are typically referred to as continuity and momentum conservation equations. Recently, the solution of these equations is solved computationally utilizing finite volume method in a CFD code, which can be written as:

$$\frac{\partial(\rho_f \alpha_f)}{\partial_t} + \nabla.(\rho_f \alpha_f V_f) = 0 \tag{30}$$

$$\frac{\partial(\rho_f \alpha_f v_f)}{\partial_T} + \nabla.(\rho_f \alpha_f V_f V_f) = -\propto_f \nabla p + \nabla.(\propto_f \tau_{f)} + \propto_f \rho_f g - F_i^f \tag{31}$$

where α_f is the fluid volume fraction in each cell,ρ_f is the fluid density,v_f the average velocity of a fluid cell, p is the pressure shared by two phases, τ_f is the viscous stress tensor, and F_i^f is the interaction force of the fluid on the particle i.

The numerical settings of CFD should be selected appropriately to make the results more reliable. Therefore, a series of numerical calculations for aerodynamic systems were performed using different grid numbers and turbulence models [184]. The accuracy of the solution generally increases with an increase in cells in the region but using a smaller grid size to discretize the region results in longer computational time [186, 188]. Although the internal flow of most agricultural aerodynamic systems is considered a turbulent flow, it is an unfortunate fact to accept a single turbulence model to be generally used as a solver for all classes of problems. Numerically, the choice of turbulence model mainly depends on some parameters such as physics encompassed in the flow, established technique for a specific class of problem, level of accuracy required, the availability of computational resources, and the time available for the simulation [189].

Currently, the CFD technique with fast and advanced computational processing equipment makes the complex turbulent fluid systems possible to model. Furthermore, most commercial CFD software such as STAR-CCM + from CD-Adapco, COMSOL Multiphysics, SIMULIA PowerFlow, ANSYS Fluent, and other open or licensed sources software provide parallel computing options to speed up the computational processes. A large number of turbulence models starting by $k-\varepsilon$ model and renormalization group RNG $k-\varepsilon$ model to the more complicated as Reynolds stress models (RSM) can be applied smoothly in many CFD software codes. These models can provide a real velocity, pressure, and temperature profiles of the fluid over the given domain [54]. While it is impossible to state the best turbulent model for a specific application categorically, so in this section, we will draft a small brief about the most critical and popular turbulence models used in the aerodynamic systems related to the agricultural application.

4.1 Standard k – ε Model

The standard $k-\epsilon$ model was firstly proposed by Launder and Spalding [190, 191], which is regarded as a semi-empirical model based on modeling transport equations for the turbulence kinetic energy (k) and its dissipation rate (ϵ) as presented in Eqs. (32 and 33). Authenticity, validity, economy, and realism for a wide range of turbulent flows give an explanation of its popularity in industrial flow and heat transfer simulations. The assumption of driving this model is that the flow is fully turbulent with high-Reynolds-number, and the effects of molecular viscosity are negligible [29, 189].

$$\frac{\partial}{\partial t}(\rho_f k) + \frac{\partial}{\partial x}(\rho_f k u_f) = \frac{\partial}{\partial x}\left[\left(\mu_f + \frac{\mu_t}{\sigma_k}\right)\frac{\partial k}{\partial x}\right] + G_k + G_b - \rho\epsilon - Y_M + S_k \tag{32}$$

$$\frac{\partial}{\partial t}(\rho_f \epsilon) + \frac{\partial}{\partial x}(\rho_f \epsilon u_f) = \frac{\partial}{\partial x}\left[\left(\mu_f + \frac{\mu_t}{\sigma_\epsilon}\right)\frac{\partial \epsilon}{\partial x}\right] + C_1\frac{\epsilon}{k}(G_k + C_3 G_b) - C_2\rho_f\frac{\epsilon^2}{k} + S_\epsilon \tag{33}$$

where u_f is the average velocity component of fluid at the position x, μ_f is the turbulent fluid viscosity,G_k is the generation of turbulence kinetic energy due to the average velocity gradients, G_b is the generation of turbulence kinetic energy due to buoyancy, Y_M is the contribution of the fluctuating dilatation incompressible turbulence to the overall dissipation rate, σ_k and σ_ϵ is the turbulent Prandtl numbers for k and ϵ, respectively, S_k and S_ϵ are user-defined source terms, R_ϵ represents the dissipation of swirl and rotational effect on turbulence, where C_1, C_2, and C_3 are constants.

Although the standard $k-\epsilon$ model considered famous and popular for modeling the full turbulence flow, it provides an inaccurate rate result for high internal velocity with high swirling and turbulence (anisotropic flow). These results make it useless and weak for modeling real-flow in the chaotic aerodynamic systems, mainly cyclone separators [35, 49, 54, 192, 193].

4.2 RNG k – ε Model

To overcome the shortages of the standard $k-\epsilon$ model, the RNG-based $k-\varepsilon$ model has been successfully developed. It is derived from the instantaneous Navier–Stokes equations of average mass and momentum conservation, using a mathematical technique, namely "Renormalization Group"(RNG) methods [194]. This method has some powerful features, such as the effect of swirl on turbulence, an additional term in the dissipation rate equation that significantly improves the accuracy for rapidly strained flows, an analytically derived differential formula for effective viscosity that accounts for low-Reynolds-number effects. These characteristics make the models more accurate and reliable for a broader category of flows than the standard $k-\epsilon$ model [189, 195, 196]. Considering these refinements in the standard $k-\epsilon$ model equations mentioned above, the model can be mathematically described well as formulated in Eqs. (34 and 35):

$$\frac{\partial}{\partial t}\left(\rho_f k\right)+\frac{\partial}{\partial x}\left(\rho_f k u_f\right)=\frac{\partial}{\partial x}\left[\alpha_k \mu_{f_{eff}}\frac{\partial k}{\partial x}\right]+G_k+G_b-\rho\varepsilon-Y_M+S_k \tag{34}$$

$$\begin{aligned}\frac{\partial}{\partial t}\left(\rho_f \varepsilon\right)+\frac{\partial}{\partial x}\left(\rho_f \varepsilon u_f\right)&=\frac{\partial}{\partial x}\left[\alpha_\varepsilon \mu_{eff}\frac{\partial \varepsilon}{\partial x}\right]\\&+C_1\frac{\varepsilon}{k}\left(G_k+C_3G_b\right)-C_2\rho_f\frac{\varepsilon^2}{k}-R_\varepsilon+S_\varepsilon\end{aligned} \tag{35}$$

where $\mu_{f_{eff}}$ is the fluid effective turbulent viscosity, α_k and α_ϵ are the inverse Prandtl numbers for k and ϵ, respectively. For more details and the sufficient background theory about the RNG $k-\varepsilon$ model, it can be found in the following biographies [197–199].

4.3 Reynolds Stress Model

The Reynolds Stress Model (RSM) is mainly constructed for the effects of streamline curvature, swirl, rotation, and rapid changes in strain rate in a more accurate way than one-equation and two-equation models [200, 201]. So, this model has more significant potential to give accurate predictions for complex flows, especially when the flow has heavy swirls and anisotropic turbulence inside aerodynamic systems such as cyclone devices [197, 202–205]. The algebraic transport equation of the Reynolds stress $\rho\overline{u_i'u_j'}$ tensor can be given in Eq. (36), while the description can be drafted in Eqs. (37–44) [206–208]:

$$\frac{\partial}{\partial T}\left(\rho_f\overline{u_i'u_j'}\right)+C_{ij}=D_{T,ij}+D_{L,ij}+P_{ij}+G_{ij}+\phi_{ij}+\epsilon_{ij}+F_{ij}+S_{user} \tag{36}$$

where the first term from the left side is the local time derivative of Reynolds stress tensor, C_{ij} is the convection; $D_{T,ij}$ is the turbulent diffusion, $D_{L,ij}$ is the molecular diffusion, P_{ij} and G_{ij} are the stress and buoyancy production rate of $\overline{u_i'u_j'}$, respectively, ϕ_{ij} is the pressure strain consists of three contributions to the pressure-strain correlation considered below, ϵ_{ij} is the dissipation, F_{ij} is the production by system rotation, and S_{user} is the user-defined source term.Whereas:

$$C_{ij}=\frac{\partial}{\partial x_k}\left(\rho_f u_k\overline{u_i'u_j'}\right) \tag{37}$$

$$D_{L,ij}=\frac{\partial}{\partial x_k}\left[\mu\frac{\partial}{\partial x_k}\left(\overline{u_i'u_j'}\right)\right] \tag{38}$$

$$P_{ij}=-\rho_f\left(\overline{u_i'u_k'}\frac{\partial u_j}{\partial x_k}+\overline{u_j'u_k'}\frac{\partial u_i}{\partial x_k}\right) \tag{39}$$

$$F_{ij}=-2\rho_f\Omega_k\left(\overline{u_j'u_m'}\epsilon_{ikm}+\overline{u_i'u_m'}\epsilon_{jkm}\right) \tag{40}$$

$$D_{T,ij}=-\frac{\partial}{\partial x_k}\left(\frac{\mu_t}{\sigma_k}\frac{\partial\overline{u_i'u_j'}}{\partial x_k}\right) \tag{41}$$

$$P_{ij}=\rho_f\left(\overline{u_i'u_k'}\frac{\partial u_j}{\partial x_k}+\overline{u_j'u_k'}\frac{\partial u_i}{\partial x_k}\right) \tag{42}$$

$$\epsilon_{ij}=2\mu_t\overline{\frac{\partial u_i'}{\partial x_k}\frac{\partial u_j'}{\partial x_k}} \tag{43}$$

$$\phi_{ij}=\phi_{ij,1}+\phi_{ij,2}+\phi_{ij,3} \tag{44}$$

where $\phi_{ij,1}$ is the slow pressure-strain which representing a return to isotropy by purely turbulent interactions [209], $\phi_{ij,2}$ is the rapid pressure-strain taking account of the return to isotropy by the interaction between the turbulence and the mean velocity gradients [201], and $\phi_{ij,3}$ is the wall-reflection term which is responsible for the damping of the velocity fluctuation component close and perpendicular to the wall that is included by default in the Reynolds Stress Model. Each component of the pressure strain can be formulated as following Eqs. (45–47):

$$\phi_{ij,1}=-C_1\rho_f\frac{\epsilon}{k}\left[\overline{u_i'u_j'}-\frac{2}{3}\delta_{ij}k\right] \tag{45}$$

$$\phi_{ij,2}=-C_2\left[P_{ij}-\frac{2}{3}\delta_{ij}\left(-\overline{u_i'u_j'}\frac{\partial u_i}{\partial x_j}\right)\right] \tag{46}$$

$$\begin{aligned}\phi_{ij,3}=&C_1'\frac{\epsilon}{k}\left(\overline{u_k'u_m'}n_kn_m\delta_{ij}-\frac{3}{2}\overline{u_i'u_k'}n_kn_j-\frac{3}{2}\overline{u_j'u_k'}n_kn_i\right)\frac{C_1k^{\frac{3}{2}}}{\epsilon d}\\&+C_2'\left(\phi_{km,2}n_kn_m\delta_{ij}-\frac{3}{2}\phi_{ik,2}n_kn_j-\frac{3}{2}\phi_{jk,2}n_kn_i\right)\frac{C_1k^{3/2}}{\epsilon d}\end{aligned} \tag{47}$$

where n_k is the x_k component of the unit normal to the wall, d is the normal distance to the wall, and $C_1 = \frac{C_\mu^{3/4}}{k}$. According to some applications, four terms can be neglected, such as the convection, the molecular diffusion, and the production by system rotation, where the buoyancy production can be equals zero for isothermal flow.

5 CFD–DEM Coupling

A CFD simulation has to be integrated with a DEM simulation to consider the effect of aerodynamic forces, which play an essential role in particle behavior. When a spherical particle is moving through the air, it is usually modeled by the sophisticated methodology of Maxey-Riley [210], which considers the flow field around the particle and the stresses obtained from the background flow. Several investigators such as Casas et al. [211], Ren et al. [40], and Sturm et al. [70] simplified these equations by combining the interaction of particle's Collision forces, Drag force, Magnus lift force, Saffman lift force, and Gravitation force. So, the translation motion of a particle through the airflow field was governed by the force balance equation, as indicated in Eq. (48) [70]:

$$m_i \frac{dv_i}{dt} = F_{ij}^C + F_D + F_M + F_S + F_{Gb} \tag{48}$$

where F_{ij}^C contact forces due to particle–particle and particle–wall contacts and can be calculated as mentioned before in Eq. (3), F_D is the drag force resulting from particle–fluid interaction (fluid damping force), and can be calculated as mentioned before in Eq. (3), F_M is the Magnus lift force generated by the relative motion between the rotating particle and the air which can be mathematically expressed by Eq. (49) [211, 212]:

$$F_M = \frac{1}{2}\rho_a A_i C_{LM} \left(\frac{\omega_i \times v_i}{|\omega_i|} \right) |v_i| \tag{49}$$

where v_i and ω_i are the relative velocity and the relative rotational angular velocity between air and particle, respectively, and C_{LM} represented the Magnus lift coefficient due to the rotation of the particle and can be expressed by the empirical formula given by Eq. (50) [40, 212, 213]:

$$C_{LM} = \begin{cases} 2\sigma & Re_i \le 1 \\ 2\sigma(0.178 + 0.822Re_i^{-0.522}) & 1 < Re_i < 1000 \\ 0.45 + (2\sigma - 0.45)exp[-0.75\sigma^{0.04}Re_i^{0.7}] & 10 < Re_i < 140 \end{cases} \tag{50}$$

where σ is a non-dimensional spin parameter which represents the particle lift due to its rotation and can be calculated according to Eq. (51).

$$\sigma = \frac{1}{2} d_i \left(\frac{|\omega_i|}{|v_i|} \right) \tag{51}$$

The Saffman lift force F_S which generated in the normal direction due to fluid shearing field around the spherical particle can be proposed by Eq. (52) [214–217]:

$$F_S = 1.615(v_a - v_i)(\rho_a \mu_a)^{\frac{1}{2}} d_i^2 C_{LS} \left| \frac{\partial v_a}{\partial n_{ij}} \right|^{\frac{1}{2}} Sign\left(\frac{\partial v_a}{\partial n_{ij}} \right) \tag{52}$$

where C_{LM} represented the Saffman shear lift coefficient and can be calculated from Eq. (53) [81, 216]:

$$C_{LM} = \begin{cases} (1 - 0.3314\gamma^{0.5})exp(-0.1Re_i) + 0.3314\gamma^{0.5} & Re_i \le 40 \\ 0.0524\sqrt{\gamma Re_i} & Re_i > 40 \end{cases} \tag{53}$$

where γ is the ratio between transitional and rotational Reynolds number as defined in Eq. (54):

$$\gamma = \frac{Re_{sh}}{2Re_i} \tag{54}$$

where Re_{sh} is the particle Reynolds number of shear flow and can be expressed by Eq. (55):

$$Re_{sh} = \frac{\rho_f d_i^2 \omega_a}{\mu_a} \tag{55}$$

Note that the value of $(F_M + F_S)$ is so-called the fluid-particle interaction force F_i^f. The net gravitational force of the particle immersed in the fluid F_{gb} was defined as the difference between particle gravity and buoyancy, as indicated in Eq. (56):

$$F_{Gb} = m_i \left(1 - \frac{\rho_f}{\rho_i} \right) g \tag{56}$$

Later, Guillermo et al. [211] concluded that the particle motion in an aerodynamic system could be numerically described through three non-dimensional groups by assuming the characteristics of length scale L_s and velocity scale U_s for the time scale. These non-dimensional groups as formulated in Eqs. (57–59) are mainly depended on the non-dimensional parameters such as spin parameter due to particle rotation σ, Remolds number of particles Re_i, particle Stokes number St_i, and gravitational parameter.

$$\pi_1 = \frac{C_d(Re_i)Re_i}{24St_i} \tag{57}$$

$$\pi_2 = \frac{C_{LM}(\sigma, Re_i)Re_i}{24St_i} \tag{58}$$

$$\pi_3 = \frac{L_s}{U_s^2} g \tag{59}$$

where group π_1 represents the drag forces over particle inertia, group π_2 represents the Magnus lift forces over particle inertia, and group π_3 represents the gravity over particle inertia.

Recently, the rotational motion of the particle in a flow field has been investigated considering the rolling friction when the particle rotates in a fluid that can be given by Eq. (60) [41, 104, 218, 219]:

$$M_{rij} = \frac{1}{64} \rho_i d_i^5 C_R \omega_{ir} |\omega_{ir}| \tag{60}$$

where ω_{ir} is the angular velocity of the particle relative to the fluid and C_R is the rotational resistance factor and can be calculated according to Eq. (61)

$$C_R \begin{cases} \frac{5.32}{Re_r^{0.5}} + \frac{37.2}{Re_r} & Re_r < 20 \\ \frac{64\pi}{Re_r} & 20 \le Re_r < 32 \\ \frac{12.9}{Re_r^{0.5}} + \frac{128.4}{Re_r} & 32 \le Re_r < 1000 \end{cases} \tag{61}$$

where Re_r is the rotational Reynolds number and can be defined in Eq. (62)

$$Re_r = \frac{\rho_a d_i^2 |\omega_{ir}|}{4\mu_a} \tag{62}$$

Casas et al. [211] also employed another reasonably approximated equation to describe the rotational motion of the spherical particle in the aerodynamic systems, as indicated in Eq. (63):

$$I_i \frac{d\omega_i}{dT} = -\mu_a d_i^3 \omega_i \left(2.01 + 0.40401 \sqrt{Re_r}\right) \tag{63}$$

As mentioned before, Coupling Discrete Element Method (DEM) with Computational Fluid Dynamics (CFD) is considered a powerful and reliable technique for understanding the physical phenomenon of particle movement in the fluid flow field, resulting in optimizing and designing the granular matter systems [35, 58, 97]. The CFD–DEM coupling approach was firstly proposed by Tsuji et al. [44], and then followed and developed by many others [47, 93, 96].

Generally, the granular flow can be defined as a group of discrete solid, and whenever it interacts with itself or fluid flow, part of the energy will be lost [95]. The granular matter has a wide range of industrial applications and is frequently modeled by coupling CFD–DEM approach [220]. CFD code can provide an interface to generate a set of fluid flow data files, which can include air, water, and other gases and fluids; thus, DEM code characterized the granular matter existing in that fluid to predict its behavior. Figure 8 provides a basic scheme to understand the main algorithm of CFD–DEM coupling.

First, the granular flow was assigned by DEM code to set the properties of the particles where each particle placed into the grid cell. Second, the fluid flow field characteristics were set and resolved by the CFD algorithm to reach the convergence. Afterward, the velocity, pressure, density, and viscosity of the flow at each position in the computational domain are transferred to DEM code in order to generate the coupling interface to compute the forces acting on each particle. Thus, the CFD–DEM coupling interface took the particle translational and rotational motion data from the DEM solver and computed the volume fractions and momentum exchange in the mesh cell of CFD. Consequently, the CFD and DEM solvers entered into the cycles of the time steps until the simulation time ended.

Generally, there are three main methods for simulating the interaction between particles and the surrounding fluids, depending on the turbulence effect [58, 221]. The first method simulates how fluids change the flow of the particles with which they come into contact. In contrast, the second approach simulates how the fluid flow changes due to the particle movement. Thus, the particle movement is not affected by the flow, but the flow around the particle is affected by the presence of particles. The last one considers the fluid streamlines compressed between particles during the simulation. In this review, we give a little brief about these coupling techniques where a complete and very comprehensive review of different CFD–DEM approaches can be found in [62].

Figure 9 illustrates the different regimes of coupling techniques on a diagram using dimensionless coordinates considering the interaction between the particles and turbulence [221, 222]. Nowadays, various configurations of commercial or open-source software packages have been developed for CFD-DEM coupling simulation, such as Rocky® (DEM package, can be coupled to Ansys Fluent®), EDEM® (DEM package can be coupled to Ansys Fluent®), PFC™ (DEM package with a built-in fluid coupling package), SAMADII© (DEM for single and multiple GPUs), CFDEM® (CFD-DEM code in C + + ; OpenFOAM® for CFD and LIGGGGHTS for DEM), LIGGGHTS® (DEM code in C + + on the LAMMPS platform), Yade (In C + + for DEM simulations), and MFIX-DEM (CFD-DEM code in FORTRAN for fluid-solid flows).

In the flow regimes diagram, the terminology of symbols can be defined as: α_i is the volume fraction of particles; [$\alpha_i = \frac{N \times Vol_i}{Vol}$, N number of particles, Vol_i particle volume, Vol volume occupied by particles and fluid], T_i is the response time of particle; [$T_i = \frac{\rho_i d_i}{18 \rho_f \upsilon_f}$, υ_f kinematic viscosity of the fluid], T_K is the Kolmogorov time scale; [$T_K = \sqrt{\frac{\upsilon_f}{\varepsilon}}$], T_e is the turnover time of large eddy; [$T_e = l/u$, l length scale of the energy-containing eddies, u root mean square of fluid velocity].

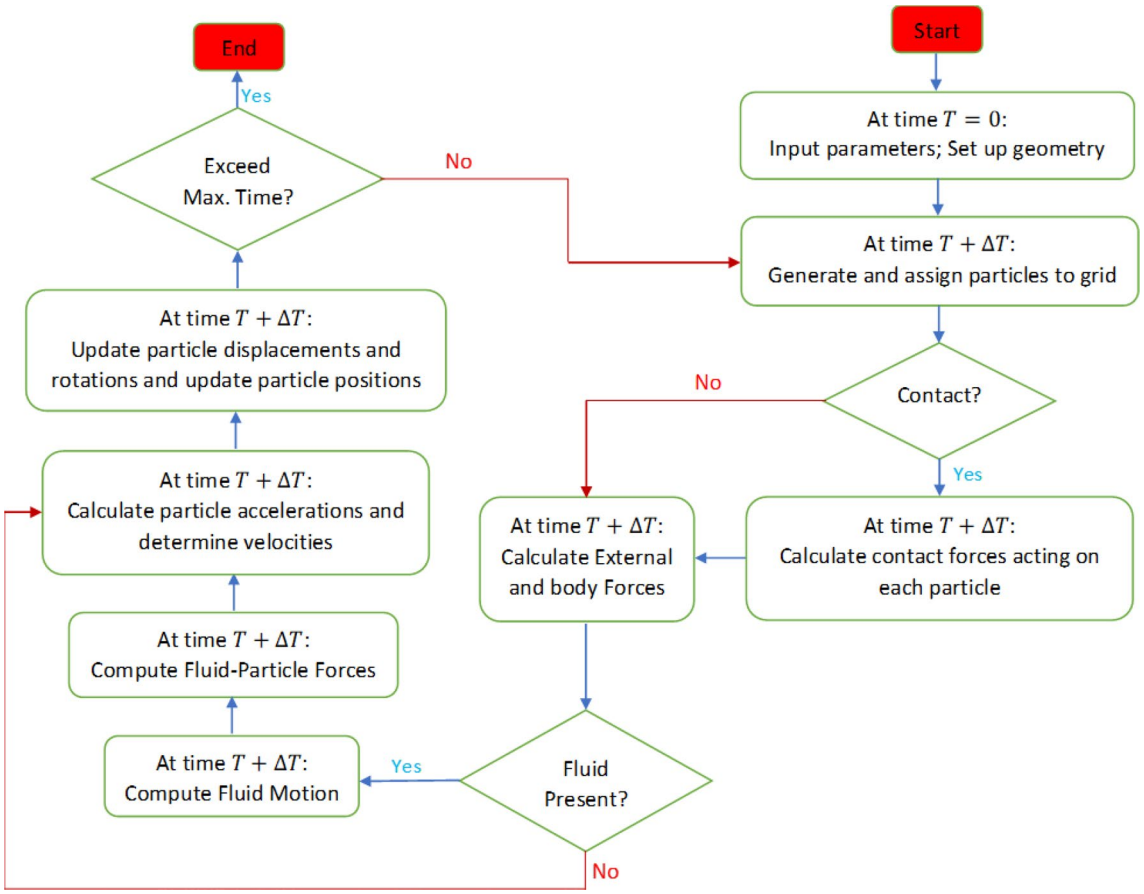

Fig. 8 Schematic diagram of CFD–DEM coupling technique

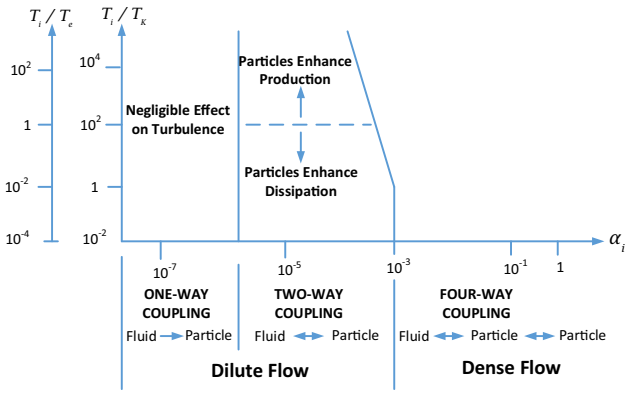

Fig. 9 Diagram of flow regimes depending on the interaction between particles and turbulence [221, 222]

5.1 One-Way Coupling

In the first interval of the flow regime, when the value of the particle volume fraction becomes very low ($\alpha_i \leq 10^{-6}$) the particles have infinitesimally effect on fluid turbulence, and the interaction between the particles and turbulence is named as one-way coupling. This phenomenon means that the distribution of the particles depends on the state of fluid turbulence and the momentum transfer from particles to turbulence. This phenomenon has an insignificant effect on the flow due to the low discrete particle concentrations. Consequently, the movement of the particle is only influenced by the fluid flow, where its velocity is considered to be the same as the surrounding fluid [221]. Numerically, the solution methodology starts with CFD calculations of the velocity and pressure distribution profiles generated by the fluid flow through the domain. Since the effect of the particles on the fluid is neglected, the only steady-state simulation needs to be performed [223]. At the end of CFD simulation, or once a steady state has reached the flow field, the CFD obtained data is then exported out and imported into DEM code. Thus, DEM calculates how the fluid flow would affect the particle flow by applying the external forces [35]. This method is particularly useful and ideally recommended in many investigations, especially for large particle separation process and unconfined homogeneous flows that has different densities of particles [186, 221, 224].

Potapov et al. [225] simulated the multiphase flow of gas and iron particles around the transfer chute using moving porosity technique with DEM Rocky® and CFD Ansys Fluent® one-way coupling. The authors mainly used this technique because of the relatively large and dense particles (+4 mm). The approving comparison of the model prediction against experimental results shows the validity of this model for the prediction of airflow around the industrial size of transfer chutes. Fonte et al. [53] flowed the strategy of one-way coupling of DEM Rocky® and CFD Ansys Fluent® to separate light from heavy particles in the wind-shifter device using different drag laws at a fixed value of airflow. Course particles with different geometries of paper (flat), stone (sphere), metal (rod), and wood (briquette), were used to determine the suitable drag low to use while simulating the separation process. The simulation showed that Ganser drag model [226] gives more accurate results because it considers the particle geometry.

Almeida et al. [29, 52] also used the one-way coupling method of DEM Rocky® and CFD Ansys Fluent® to put a theoretical algorism for separating the sugarcane bagasse into different groups of particles. Different air velocities through an aerodynamic conveying system were used considering the contact forces between particle–particle and particle–wall. The result showed that this coupling technique perfectly describes the separation process with reasonable accuracy. Since the main recommendation of this work is that the separation process will be more efficient and real when using coarse and large particles. El-Emam et al. [35] perfectly applied the above recommendations of DEM Rocky® and CFD Ansys Fluent® codes to simulate and optimize the separation process of real-particles of Jojoba seeds and its leaves. Five geometries of gas-cyclones were used, and the particle interaction was considered. The simulation can successfully predict the separation efficiency and the behavior of the particles that help to optimize the cyclone geometry and performance.

5.2 Two-Way Coupling

When the value of the particle volume fraction is located between $10^{-6} \leq \alpha_i \leq 10^{-3}$ and the particle loading volume is large enough to affect the turbulence structure, the term two-way coupling used. In this regime, the exchange of mass, momentum, and velocity information between the solid phase and the fluid phase occurred, where the meaningful feedback is noticed in turbulence damping due to buoyancy effects [186]. So, it can say that the particles are part of the fluid flow and will affect it in a two-way interaction. This phenomenon means that the particle movement is affected by the interaction with other particles and the fluid around it, while the flow is also affected by the particle presence. As described in (Fig. 9), at a specific value of particle volume fraction, when the diameters of the particles are small with the same material and fluid viscosity lowering (T_i is low), the surface area of the particulate phase increases resulting in increasing the dissipation rate of turbulence energy. On the other hand, increasing T_i for the same value of α_i (inclined line), the particle Reynolds number increases, and the vortex shedding takes place resulting in promoting the turbulence energy production.

The simulation scheme used in this coupling technique is a transient state simulation that allows both solvers of CFD and DEM to run in a parallel way that can significantly decrease the simulation time [223]. This coupling methodology is suitable for dealing with a large number of particles through a CFD cell and not for dealing with particles larger than CFD cells. Therefore, it is recommended that the domain mesh size should be larger than the largest particle size through the simulated domain [58, 227]. The significant advantage of the two-way coupling simulation is that particle agglomeration can alter airflow trajectories and velocities and vice versa. Thus, the interaction between solids and gas is considerably closer to actual phenomena [29].

Zhong et al. [156] carried out a three-dimensional simulation of cylinder-shaped particles in a gas–solid fluidized bed using a two-way approach considering drag force, contact force, and gravitational force. The predictive behavior of particles and pressure drops at different superficial gas velocities were in good agreement with the experimental results. Ren et al. [40] study the flow behavior of corn-shaped particles in the cylindrical spouted bed with a conical base device using this coupling technique. The obtained results demonstrate that the coupling model methodology is valid and useful in describing the hydrodynamic behavior of the spouted bed.

Fonte et al. [53] set a fluidized bed simulation case to apply the two-way coupling technique of DEM Rocky® and CFD Ansys Fluent® using Huilin and Gidaspow drag law. The agreement between the pressure drop predicted by Ergun's correlation and the pressure drop obtained in the simulation is relatively good until fluidization takes place, which states the capability of the fluid being affected by a reactive force. Devarampally [186] developed a two-way coupling of CFD–DEM using Simcenter STAR-CCM$^+$ code for a top spray fluidized bed granulator to study the effects of inlet air flow rate, the temperature on the particle dynamics and the residence time in the spray zone. The developed model was able to predict the changes in particle velocities, temperatures, collision dynamics, and particle transfer from one compartment to the other as the inlet velocity and the temperature of the air changes. This model can be recommended to determine the agglomeration rates in a granulation process, develop hybrid CFD-DEM-PBM that describes the rate processes in granulation, and understand the effect of process parameters on the product quality attributes.

Carlos Varas et al. [101] employed a CFD–DEM two-way model to simulate the co-current gas-particle flow in a pseudo 2-D dilute flow riser. The model reasonably predicted the core-annulus flow and other hydrodynamic parameters such as cluster frequency, internal solids volume fraction, and aspect ratio that showed close agreement with experimental data. Baran et al. [155] applied a fully coupled CFD-DEM two-way approach to study the effect of particle shape on fluidization in a cylindrical fluidized bed using Simcenter STAR-CCM$^+$ software. The observations are consistent with the similar simulation and experimental results reported in the literature [228, 229], which gives strong evidence for applying this technique to predict the dynamic behavior of different particles shape in the fluidized bed. Almeida et al. [29] simulated the dry bagasse separation in a pneumatic device using DEM Rocky® and CFD Ansys Fluent® coupling approach. The comparison with the experiment showed that the developed model predicted the particle separation phenomena with high accuracy.

5.3 Four-Way Coupling

Herein, the four-way coupling term is developed due to the interactions between particle-turbulence, particle–fluid-particle, particle–particle, and frictions of particles., In this case, the fluid streamlines between particles are compressed where the flow is considered to be dense [221]. This means the particle loading is very high and concentrated where the value of particle volume fraction is assumed to be higher than 10^{-3}. Due to the complexities of flows in this regime, most experimental and numerical studies considered the flow to be dilute. As can be seen in (Fig. 9), the line which separates the two-way and four-way couplings are inclined as the particle–particle collision occurs at higher values of T_i/T_e, thus transforming the two-way to four-way coupling technique. Note that, when particle volume fraction approaches to l, a total granular flow is presented in which there is no fluid will be obtained between particles. In this coupling approach, the simulation technique runs on a parallel implementation of CFD and DEM, which can significantly stimulate the two-phase fluid–solid phase.

Laín and Sommerfeld [230] predicted the behavior and the pressure drop in a particle-laden horizontal channel with rectangular cross-section by the Euler–Lagrange approach accounting for two-way and four-way coupling. Different diameters and mass loading ratios of particles were considered where the particle–wall interactions and inter-particle collisions have also been taken into account. The numerical simulation technique has reasonably reproduced the studied trends; however, the numerical predictions of wall-bounded flows cannot be appropriately applied when neglecting the wall roughness effects. Comparing the obtained data with the experiment result, it can be somewhat indicated that the considered model is appropriate to simulate aerodynamic conveying of spherical solid particles in a horizontal channel device with the dense flow. Kuang et al. [231] presented a 3-D numerical study of vertical aerodynamic conveying by combining a four-way CFD–DEM approach for dilute and dense gas–particles flow regimes. The numerical method can satisfactorily capture the key flow behaviors observed, such as particle flow pattern and gas pressure characteristics. In the dense-phase flow regime, the simulation results confirmed that the particle–particle and particle–wall force increases with the increase of the particle–fluid force, but in contrast for dilute-phase flow where it is small, if not negligible.

Sturm et al. [70] extended the previous simulation to also show the applicability of the presented simulation model to the different flow regimes: a dense vertical aerodynamic conveying system and dilute conveying in a horizontal-to-vertical pipe bend. To track the flow behavior, the Euler–Lagrange approach is presented, and an in-house soft sphere DEM code is coupled to Ansys Fluent®. It is shown that the different aerodynamic conveying regimes can be behaved well comparing to the experimental data. Traoré et al. [232] also derived a complete four-way coupling model of a gas–solid 3-D fluidized bed by taking into consideration particle–particle, fluid-particle, and particle–wall interactions. The simulation constructed on a high dense flow of 2.7 million particles in two different ways: pulsed jet and bubbly regime. The output data perfectly pointed out the existence of complex structures such as the worm-like shape one, similar to those that have already been described in other literature. Considering the above results, it is shown that a definite proof to use this coupling scheme for predicting sensitive phenomena in the large dense granular systems.

6 Drag Correlation Models

During the run of CFD–DEM coupling in an aerodynamic system, the drag correlation model shows vital importance besides pressure gradient forces, especially for describing and dealing with the interaction between particle shape and concentration and the surrounding fluid [139, 233, 234]. For successful coupling, it is crucial to choose a suitable drag correlation model [53]. There are several drag correlation models developed and available in the literature. Most of them are mainly dependent on the Reynolds number, where others need other properties, such as fluid volume fraction and particle sphericity. Here, in this review, we will concentrate the attention on the most common correlations that can be used in modeling bio-particles based on the flow regimes. The attempts by investigators and the developments for models listed in Table 2 illustrate the applicability of this approach.

Table 2 Drag correlation models used in CFD–DEM coupling

Flow regime	Models and Reference	Equations	Notes
Dilute flow	Schiller and Naumann (1933) [53, 100, 205, 235–237]	$C_D = \begin{cases} \frac{24}{R_{ei}}\left(1+0.15R_{ei}^{0.687}\right) & R_{ei} \le 1 \\ max\left[\frac{24}{R_{ei}}\left(1+0.15R_{ei}^{0.687}\right)\right] & 1 < R_{ei} \le 1000 \\ 0.44 & R_{ei} > 1 \end{cases}$	For spherical particles
	Dallavalle (1948) [238]	$C_D = \left(0.63 + \frac{4.8}{\sqrt{R_{ei}}}\right) R_{ei} < 3000$	For spherical particles
	Haider and Levenspiel (1989) [28]	$C_D = \frac{24}{R_{ei}}\left(1+AR_{ei}^{B}\right) + \frac{C}{1+\frac{D}{R_{ei}}} R_{ei} < 2.6\times10^5$ For spherical particles: $A = 0.1806, B = 0.6459, C = 0.4251, D = 6880.95$ For non-spherical particles: $A = exp\left(2.3288 - 64581\emptyset_i + 2.4486\emptyset_i^2\right)$ $B = 0.0964 + 0.5565\emptyset$ $C = exp\left(4.905 - 13.8944\emptyset_i + 18.4222\emptyset_i^2 - 10.2599\emptyset_i^3\right)$ $D = exp\left(1.4681 + 12.2584\emptyset_i - 20.7322\emptyset_i^2 + 15.8855\emptyset_i^3\right)$	For isometric non-spherical particles and non-isometric non-spherical particles
	Ganser (1993) [29, 52, 53, 226, 239]	$\frac{C_d}{K_2} = \frac{24}{R_{ei}K_1K_2}\left[1+0.1118\left(R_{ei}K_1K_2\right)^{0.6567}\right] + \frac{0.4305}{1+\frac{3305}{R_{ei}K_1K_2}}$ $K_1 = \left(\frac{d_i}{3d_{i_{vol}}} + \frac{2}{3}\emptyset_i^{\frac{-1}{2}}\right)^{-1} - 2.25\frac{d_{i_{vol}}}{D}$ $K_2 = 10^{1.8148\left(-log_{10}\emptyset_i\right)^{0.5743}}$	Valid when $R_{ei}K_1K_2 < 10^5$ Used when the particles in the domain differ in shape, concentration, and alignment
Dense flow	Wen & Yu (1966) [240, 241]	$C_D = \begin{cases} \frac{24}{\alpha_f R_{ei}}\left[1+0.15\left(\alpha_f R_{ei}^{0.687}\right)^{0.687}\right]\alpha_f^{-1.65} & \alpha_f R_{ei} < 1000 \\ 0.44\alpha_f^{-1.65} & \alpha_f R_{ei} \ge 1000 \end{cases}$	Relatively for low particle concentration:$\alpha_i < 0.2$
	Ergun (1958) [100, 139, 242, 243]	$C_D = 200\frac{\alpha_p}{\alpha_f\emptyset_i^2 R_{ei}} + \frac{7}{3\emptyset_i}$	For high particle concentration:$\alpha_i \ge 0.2$
	Huilin & Gidaspow (2003) [244]	$C_D = \varphi C_{D,Ergun} + (1-\varphi)C_{D,Wen\&Yu}$ $\varphi = \frac{arc\tan\left[262.5\left(0.8-\alpha_f\right)\right]}{\pi} + 0.5$	For particle concentration:$0.2 > \alpha_i \ge 0.2$
	Di Felice (1994) [29, 100, 223, 243, 245]	$C_D = \alpha_f^{2-\beta} C_{D,singleparticle}$ $\beta = 3.7 - 0.65exp\left\{-\frac{\left[1.5-\log_{10}\left(\alpha_f R_{ei}\right)\right]^2}{2}\right\}$	$10^{-2} \le R_{ei} \le 10^4$

7 Applications

To model the granular flow in the agricultural aerodynamic systems, various mathematical and numerical models include theoretical approaches, differential equations of motion, incremental technique, and computer programming were used. For instance, by MATLAB modeling, Adewumi [79] started to simulate the flow of cowpea grains through the transport and separation process in a horizontal airstream. He developed a 2-D Modeling using the aerodynamic principles of drag and gravitational forces to provide a clear vision about the air-particle dynamics in such a system. The obtained results showed the ability to construct the separation, cleaning, sorting, grading, and density classification processes in one machine. Recently, with the increase of agricultural industry applications concurrently with the high power of computer technology, CFD–DEM coupling approach is frequently used to model, predict the behavior, and provide the solutions of the air-particle flow problems [80, 246].

7.1 Air-Screening System

The process of separation and cleaning grain materials from impurities such as spikelet, leaves, straw remnants, husks, and small weed seeds, etc. is essential in agricultural grains

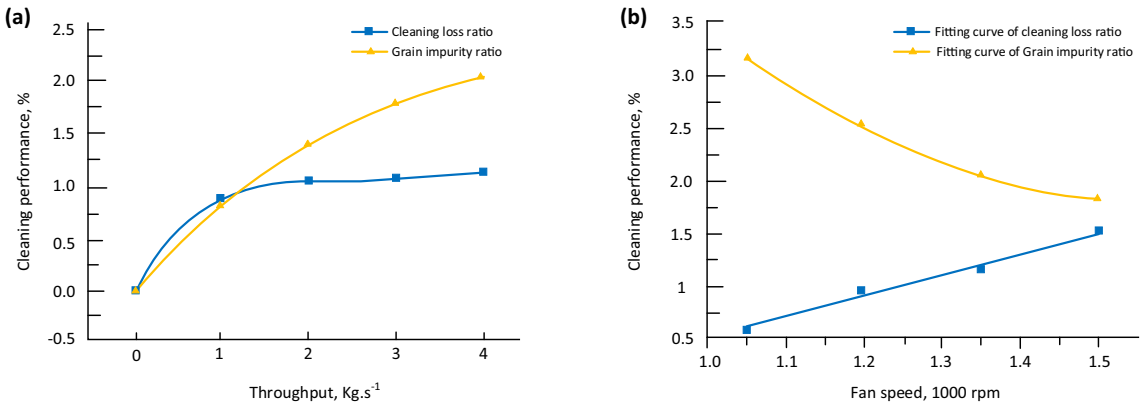

Fig. 10 Polynomial diagram of (a) throughput and (b) fan speed with cleaning performance [249]

production. In modern harvesting machines such as combine harvesters, the separation and cleaning processing are mainly implemented by air-screening or air-sieving systems [247]. In such a system, the modeling process can be numerically described as a complex system of two-phase flow. One phase is the airflow generated by a centrifugal fan, and the other is solid particles dispersed in the system by the airflow [248]. As mentioned before, the effect of air velocity has significant influence in such a separation process that the airflow entrains the light particles due to the aerodynamic drag force. At the same time, the heavy ones are mainly separated by the force of gravity and the inertia of sieves.

Numerically, Li et al. [39] carried out a 3-D coupled of CFD–DEM approach in an air-and-screen cleaning unit to study and analyze the influence of inlet airflow velocity on rice grain and short straw taking into consideration the longitudinal velocity, vertical height, and cleaning loss. The rice grains were modeled as a spheroid particle, and the short straws introduced as a cylinder shape. The particle materials were modeled and generated in EDEM software and allowed to fall on an inclined vibrating screen. A Eulerian–Eulerian model was used in simulating the airflow using Ansys Fluent® as a part of a coupling, where the Hertz-Mindlin contact model was applied to simulate particle–particle and particle-screen (wall) collisions. The simulation results reported that the length of the screen could be shortened if material straws and foreign materials are not too much since the higher the inlet airflow velocity, the faster the backward velocity of the materials on the screen surface and the more the cleaning loss. This work is extended by Li et al. [249] to simulate the effects of throughput and operating parameters on cleaning performance in the same device. Ansys Fluent®, as an auxiliary investigation software, was used to analyze the movement behavior of the internal airflow. The standard $k-\epsilon$ turbulence model is proposed for this simulation study to describe the real-physical processes at the different airflow velocities above and below the vibrating screen. The results as described in (Fig. 10a,b) showed that the fan speed have a great effect on cleaning performance by affecting the overall airflow velocities in the cleaning device where the throughput has a sharp effect on grain impurity ratio.

Furthermore, Lenaerts et al. [77] modeled the separation chamber in the combine harvester through a cubic box to predict the separation profile of the grain-straw using DEM simulations. The grains were assumed to be spherical, while the straw particles are modeled as a segmented hollow cylinder that can be bent in all directions using DEMeter + + software. The main prediction is that separation speed is influenced by particle properties, but the main effects can be related to straw coverage and grain diameter. Ma et al. [76] developed another variable-amplitude screen box to analyze the traditional reciprocating screen in the combine harvester. The particles used in their study were divided into two groups: rice grain and rice straw that are modeled as ellipsoidal and cylindrical, respectively, by a multi-sphere approach. Based on the Hertz-Mindlin contact model in EDEM software, the simulation showed that the variable-amplitude screen could make the particles at the front of the screen be quickly thrown up and moved back but could not favor their segregation and separation at the screen front.

On the other hand, [250] studied the grain behavior in an inertia separation chamber of the combine harvester based on CFD–DEM simulation. The grains were modeled as ellipsoidal, while the straw modeled as cylindrical shape through the multi-sphere approach. The $k-\epsilon$ turbulence model was used in Ansys Fluent® software to reach the convergence state of the airflow while the Euler-Lagrangian method in EDEM code was applied to model the particles. The simulations showed that the grains were effectively separated from the short straw through the airflow. Besides, the performance of separating and cleaning grains was improved with the increase of airflow velocity. However, turbulence

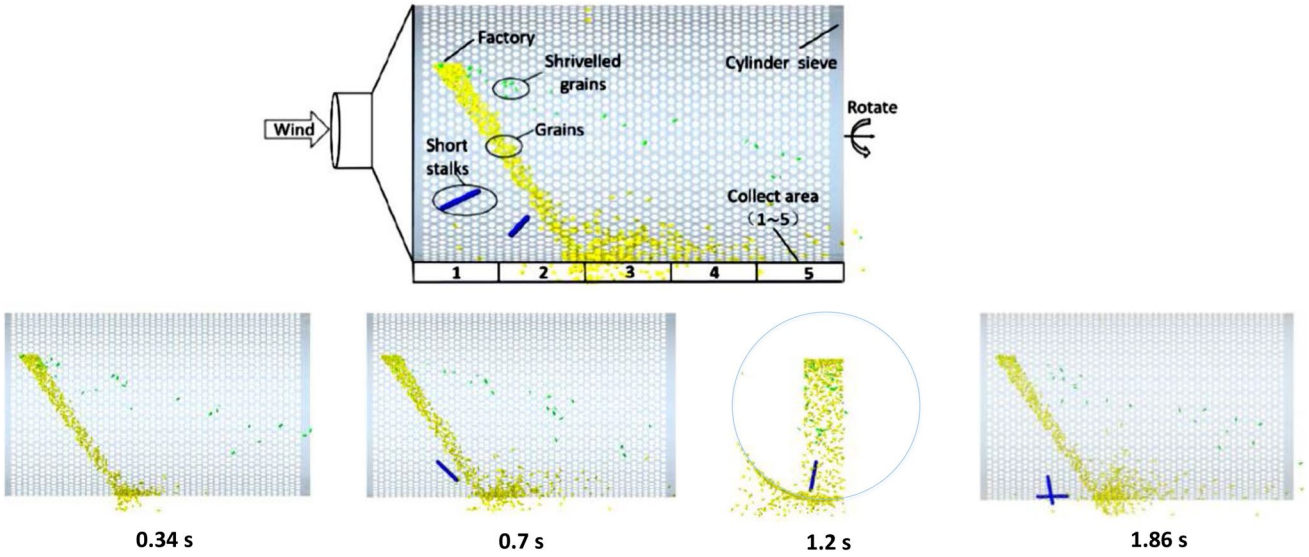

Fig. 11 The particle trajectories of the rice-threshed mixture during the simulation process [218]

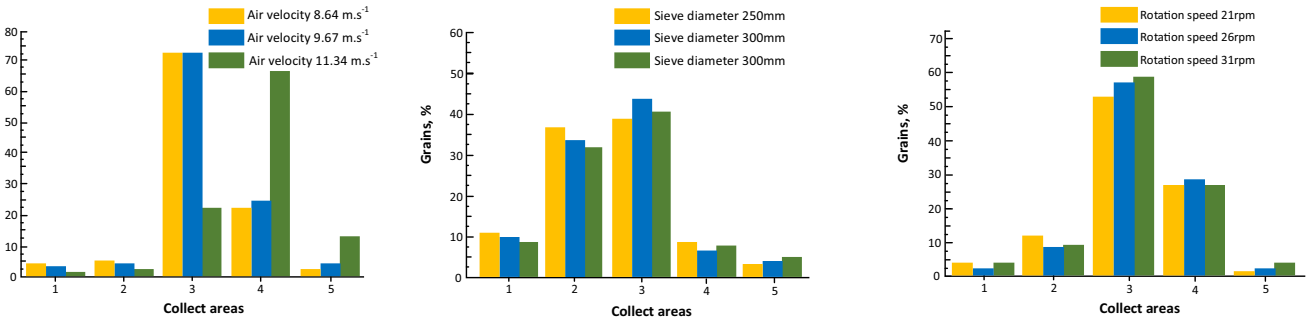

Fig. 12 The mass distribution of the grain during the screening process [218]

and pressure drop were severely increased at the end of the separation chamber.

Yuan et al. [218] investigated the screening process of rice-threshed mixture components (grains, shriveled grains, and short stalks) through a cylindrical sieve device using CFD–DEM coupling. The influence of inlet airflow velocity, the diameter of, and the rotating speed of the cylindrical sieve on the separation process was studied. First, the particles were scanned by a 3-D laser scanning system then, modeled by multi-balls fast filling method (API) in EDEM software and allowed to move smoothly through the cylinder sieve. The particle phase is considered to be in a continuous quasi-fluid phase and solved through the average Navier–Stokes equation, where the airflow was simulated through the existing Eulerian–Eulerian model in the Ansys Fluent® code. To track the separation process (Fig. 11), visualized the simulation of particle trajectories with the time though the device, where the yellow, green, and blue colors represent grains, shriveled grains, and short stalks, respectively. The numerical simulation showed an increase in the screening efficiency tendency when the cylindrical sieve diameter increased. At the same time, the rotating speed has a significant effect on the average axial velocity of the short stalks, screening loss rate, and screening efficiency. Figure 12 showed the mass distribution in every collect area (from 1 to 5) as a relation of inlet airflow velocity, cylindrical sieve diameter, and its rotational speed.

As shown in the investigations, the technique and the methodology of the numerical simulations used for modeling the air-screening systems can provide a useful reference for predicting the flow behavior and solving the separation problems of biomaterials. Because CFD–DEM coupling models had a reasonable predict comparing to the experimental results in the above investigations, it is strongly recommended to be used for improving and optimizing the design of air-screening devices in the combined harvesters.

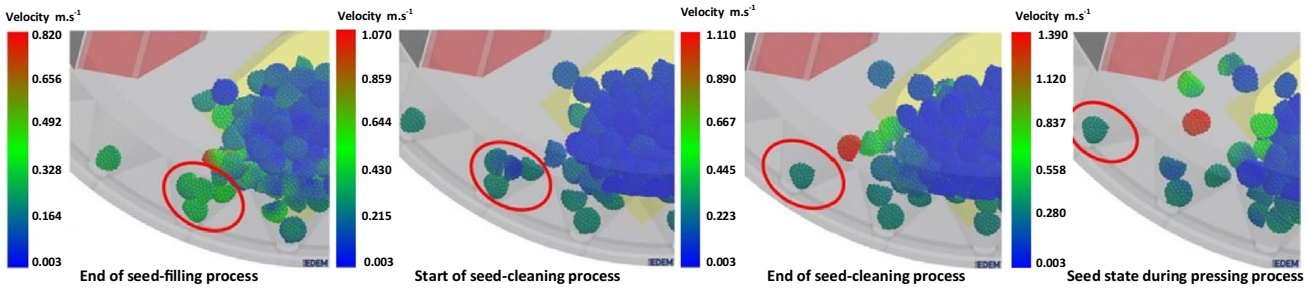

Fig. 13 Seed motion behavior of the seed-cleaning process [42]

7.2 Seed-Metering Device

Precision agriculture made agricultural production and agricultural management more accurate and useful [251]. Precision seeding is an essential part of precision agriculture, which has always attracted the attention of researchers [252]. It can be defined as the placement of single seeds in the soil at the desired plant spacing [253]. The Seed-metering device considers the main component of the planter machine to represent adequate seeding performance. Although there are various types of seed-metering devices, each with unique individual working principles, aerodynamic seed-metering devices are used more widely because of their high accuracy, preservation of seed integrity and fitness for high-speed operation [254, 255]. Recently, the numerical simulation approach has effectively applied for modeling the air-seeds flow in the aerodynamic seed-metering devices to promote effectiveness and performance.

For instance, Dandan et al. [256] applied the coupling method of CFD–DEM to simulate the effect of different air nozzle installation positions on the working performance of inside-filling air-blowing precision seed metering device. They concluded that CFD–DEM simulation could detect and predict the maize seed movement behavior in a single seed meter. Han et al. [42] extended their work to simulate and optimize the air-maize flow in the same device using the same numerical methodology. The effects of positions, width, and average arc length of the lateral hole were studied in terms of the gas field and seed movement. The maize particles were regarded as a hard-sphere model and created by EDEM software using the bonded particle model (BPM) technique, which allows the particles treated as a soft sphere model. While the standard $k-\epsilon$ two-equation turbulence model was used to solve the gas phase and the Eulerian two-fluid coupling approach was applied.

According to the numerical simulations, the seed motion behavior of the seed-cleaning process can be correctly predicted, as illustrated in (Fig. 13). The simulation results also indicated that the area of the lateral hole seriously affected the movement and airflow field of seeds in the hole. When the position is lower, the optimized lateral hole, which has a width of 1.5 mm and an average arc length of 10 mm, had an excellent working performance, with less pressure loss, superior drag force, and differential pressure. The performance of the optimized seed-metering device in the experiments reached 93% when the working pressure was above 5.5 kPa with a working speed lower than 10 km.h^{-1}.

Lei et al. [81] studied and analyzed the effects of the throat's structure, airflow inlet velocity, and seed feed rate in seed feeding device (pneumatic Venturi tube) in terms of air and seed behavior using CFD–DEM coupling approach. This feeding device is usually used in the pneumatic seeding planter machine. Rapeseed and wheat were used and modeled as spheres and multi-sphere, respectively, using EDEM software. Hertz-Mindlin model was chosen as particle modeling while the gas-phase was solved with the standard $k-\epsilon$ two equations turbulence model. The coupling interface was implemented by the Lagrangian coupling method. Simulation results showed that the throat's area and airflow inlet velocity mainly affected airflow outlet velocity, while seed movement was slightly affected by throat length and seed feed rate. The increase in the throat area resulted in a decrease in seed's velocity and pressure loss in a certain range. When the inlet air velocity increased, resultant force and seed velocity developed. Figure 14a,b showed the simulation flow patterns of rapeseed and wheat seed at the designed air velocities. It can be concluded that the appropriate airflow inlet velocity was 16–20 m.s^{-1} and 20–24 m.s^{-1} for rapeseed and wheat, respectively.

Although Venturi tube was widely used in industry, limited numerical studies are available in the literature, especially for particle motion in aerodynamic seeding systems. Lei et al. [257] extended their study to characterize the rapeseed and wheat migration trajectory and predict the distribution behavior of a pneumatic distribution head in the air-assisted centralized seed-metering device (Planter). The streamlined angle, the radius of baseline, outlet diameter of streamlined angle, lid angle, and installation location in the distribution head were the main parameters to investigate in this study. The particles were regarded as

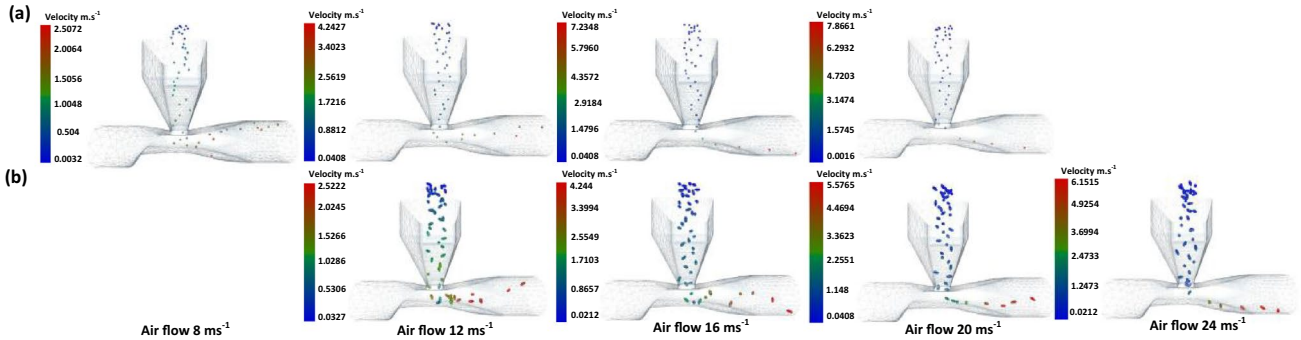

Fig. 14 Flow patterns of (**a**) rapeseed and (**b**) wheat seed at different air velocity [81]

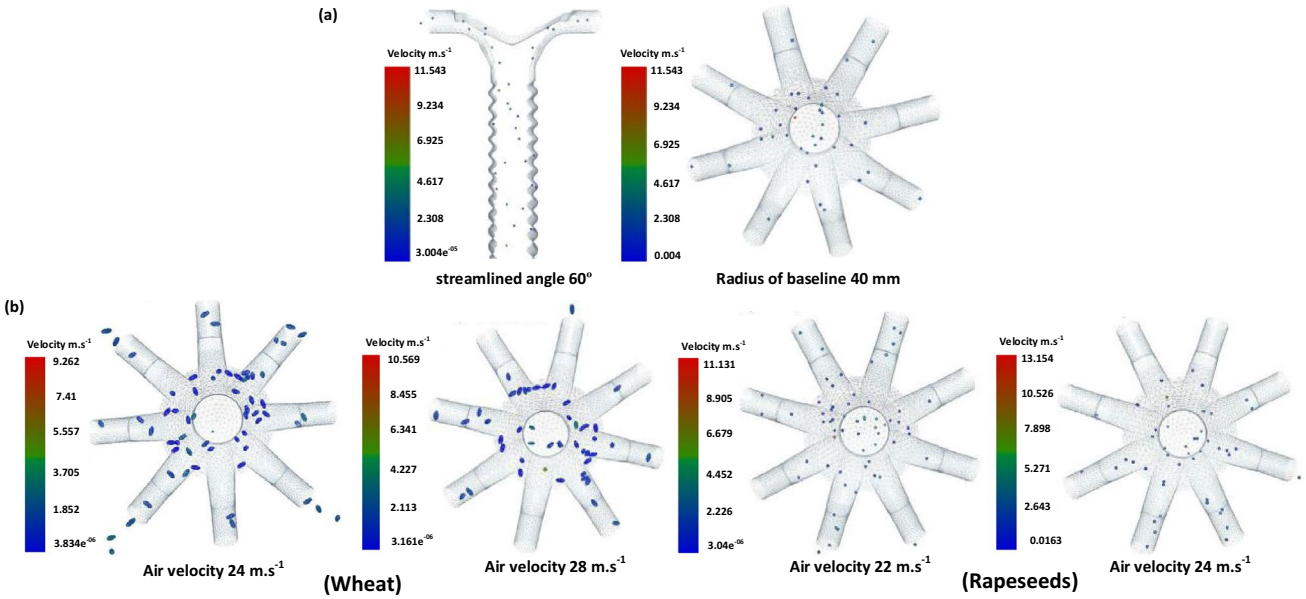

Fig. 15 Snapshots of wheat and rapeseeds simulation in the distribution head [257]

a hard-sphere model where the Hertz-Mindlin (no-slip) model was applied as the particle contact model, and the seed feed rating was adjusted by EDEM software. The rapeseeds were modeled as the spherical shape where the wheat seeds were generated as ellipsoidal shape by a multi-sphere approach. To model the turbulence in the airflow, the standard $k-\epsilon$ turbulence model and the airflow velocity were set in the Ansys Fluent® software. Simulation results first predicted the variation coefficient of seeds distribution in the head. With the increase of streamlined angle from 10° to 50°, the variation decreased initially and then increased for an inlet diameter of 20 mm and an airflow velocity of 20 m.s^{-1}. Also, when the radius of baseline was less than 20 mm, the air pressure loss and resultant seed force visibly increased.

Furthermore, the resultant seed force and resultant velocity increased with the increase of airflow velocity. Second, as showed in (Fig. 15a), the distribution of the seed was more uniform when the streamlined angle is 60°, the radius of the baseline is 40 mm, and the lid angle is 120°. Also, the distribution uniformity and power consumption improved at the airflow velocity of 20–24 m.s^{-1} for rapeseed and 24–28 m.s^{-1} for wheat of different seed feed rates, as illustrated in (Fig. 15b).

The obtained result approved that the CFD–DEM coupling approach is a reliable and feasible tool for simulating the physical phenomenon of seed movement in the airflow field. Also, It can help improve distribution uniformity, explain the seed distribution mechanism, assist the performance, and optimizing the design of air blowing seed devices.

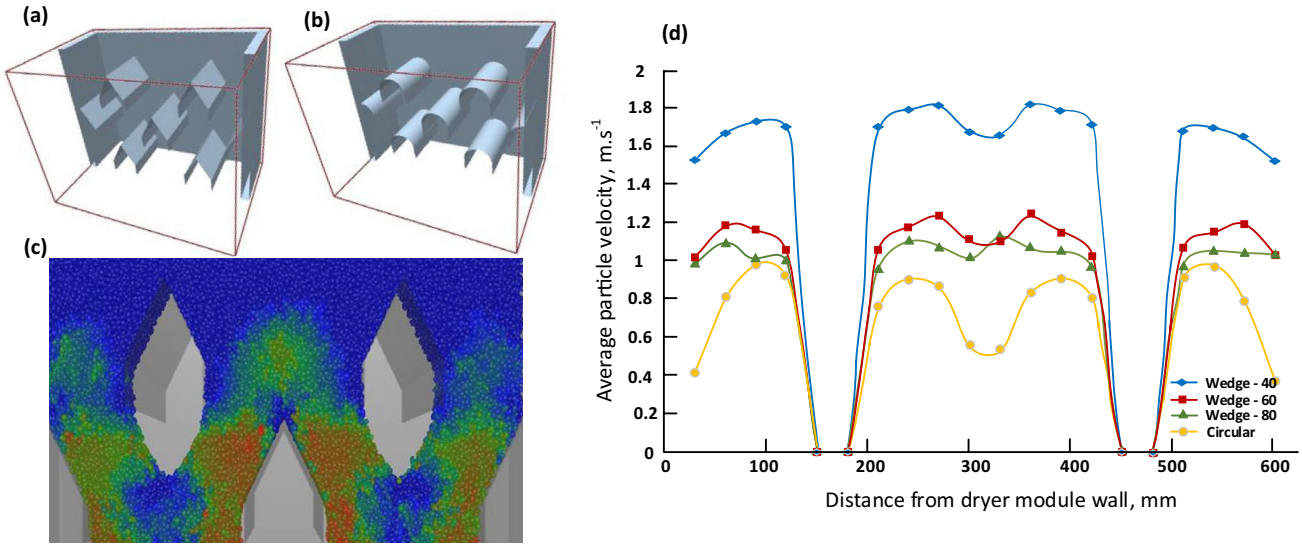

Fig. 16 Simulated velocity differences around the different air ducts (right): **a** wedge duct, **b** circular duct, **c** velocity distribution of the wheat (red higher, blue lower velocities), and (**d**) velocity differences from the dryer wall [67]

7.3 Drying Systems

Drying technology is widely applied in agriculture to preserve large mass flows of food grains, seeds, kernels, and other macroscopic particulate matter after harvesting in farms [258, 259]. For continuous drying, which is common in the industry, mixed-flow or cross-flow dryers (MFDs) are widely used [260]. The moisture is removed from the grain by forced dry air convection through the grain bed using air ducts installed in the bed, in order to prevent microbial activity and spoilage.

Keppler et al. [67] analyzed the influence of different constructional modifications of air duct shape and wall friction on the velocity distribution difference of wheat particle within the MFD module through the EDEM code package. Two types of modified air duct shapes were used: wedge and circular ducts, as shown in (Fig. 16a,b). The particles were modeled by a multi-sphere approach as a clump of three spheres, where the Hertz-Mindlin (no-slip) contact model was used to model the interaction forces. The simulation data represented substantial velocity differences when using the circular air ducts, so it is not appropriate in wheat drying usage. Also, significant velocities difference observed depending on particle place in the module. While, the near-wall is much lower than in the middle, as shown in (Fig. 16c,d). So, using smooth structure materials lead to decreasing the particle–wall friction ratio resulting in more even velocities distribution. By this, it would be easy to get an excellent homogeneous drying for the particles.

To avoid extra drying costs and improve the product quality, Weigler et al. [69] evaluated the traditional designs of MFDs employing CFD–DEM to discover design imperfection. The dryer geometry and different air duct arrangements (horizontal and diagonal) were studied. Wheat particles were chosen and modeled in two geometries as an ellipsoidal clump and spherical by Particle Flow Code (DEM-PFC 2-D) software to compare the particle flow simulation. The airflow domain was discretized by generating a finite volume grid employing the software ANSYS ICEM. Then, the airflow was regarded as a turbulence flow and modeled by ANSYS CFX® software using the two-equation shear stress transport (SST) model. The simulation data successfully captured the particle-air flow distribution inside the dryer, comparing to the experimental result. It was found that the drying is not perfect in the traditional mixed-flow dryers because of air duct arrangements, the appearance of dead zones in airflow, and irregular distribution of airflow due to the wall frictions. In this context, appropriate air duct arrangements should be fixed to adjust the higher and lower air velocities in the middle part and near to sidewalls of the dryer, respectively. Consequently, the current authors recommended a new dryer model to adjust the airflow distribution; consequently the particle flow velocities that the sidewalls of the dryer should be inclined, and the half air ducts should be removed.

So, Weigler et al. [261] worked in the previous recommended model to develop a new geometry of MFDs that results in the homogeneous particle drying, higher energy efficiency, and increase product quality. The wheat flow was tracked by the different grain colors through a transparent sidewall using DEM-PFC2-D. Based on the experiments and numerical simulation observations, the new design meets most requirements of the particles drying.

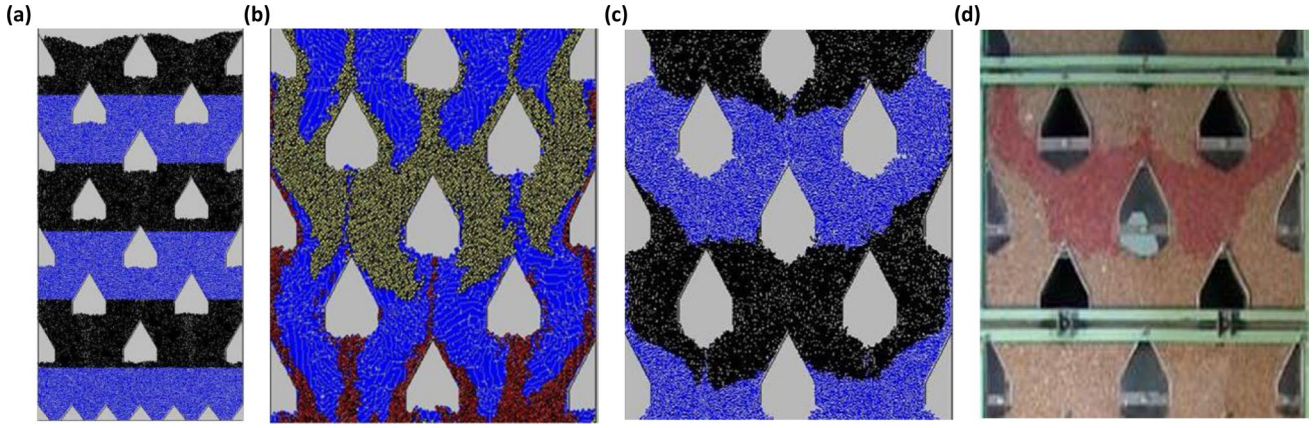

Fig. 17 Particles flow patterns in MFD: **a** particles after DEM gravitational generation, **b** DEM sphere particles, **c** DEM ellipsoidal clamp, **d** experimental result [258]

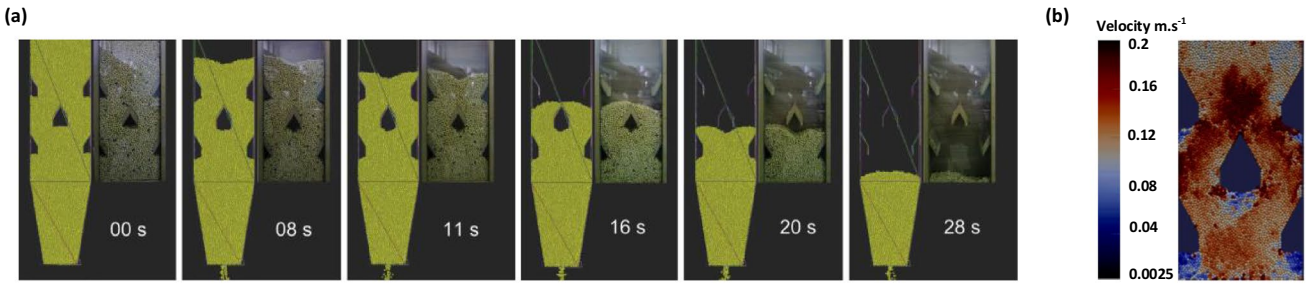

Fig. 18 **a** comparison of soya bean discharge for simulation (left frame) and experiment (right frame) at discharging hole 20 mm, and (**b**) velocity field distribution [37]

On the other hand, Weigler and Mellmann [258] discovered without airflow the dry wheat kernels behavior through the traditional MFD of Weigler et al. [69] using DEM-PFC2-D where the results were compared with the experiments. A multi-sphere approach shaped the wheat kernels as an ellipsoidal clump and its flow behavior compared to the spherical shape. Alternately, the particles were colored black and blue to observe the mass flow behavior in the 2-D view, as shown in (Fig. 17a–d). As illustrated, the DEM model based on the ellipsoidal particle can effectively predict the real-grain flow behavior that the colored grain layer in the experiment showed the same profile as in the numerical simulation. In contrast, when spherical particles were used, the bed angle that was typically formed under the air ducts did not appear.

The simulation findings which are entirely agreed with the experimental results promoted the main flow features of particle flow: the higher flow velocities were through the center of the dryer and had lower friction effects than those flowing through the regions near the dryer walls. These particles traveled with lower vertical velocities due to the higher frictional effects, which made the grains have different residence times in the dryer. This phenomenon leads to a non-uniform moisture distribution at the dryer outlet. Consequently, developing a new design that can adequately evanesce the difference in residence time of the particles is still need. Moreover, the main recommendation is that the 2-D DEM model does not accurately predict the absolute values of the grain mass flow pattern and velocity. Therefore, a three-dimensional simulation should be applied for dryer modeling.

Hence, Khatchatourian et al. [37] carried out the first trial to develop a 3-D model of soya beans flow applying DEM-Yade software package to predict the behavior and motion of particles during the discharging process in MFDs. The particles were modeled as a 3-D single spherical geometry considering the physical properties. An experiment was carried out to validate the simulation data that showed a satisfactory agreement between their results, as shown in (Fig. 18a).

By Applying the method of colored particles for continuous flow in the MFD, the differences of soya bean velocities successfully observed. Near the wall regions, seed velocities were lower than in the center, as illustrated in (Fig. 18b). Thus, the seed velocity field is nonuniform, leading to

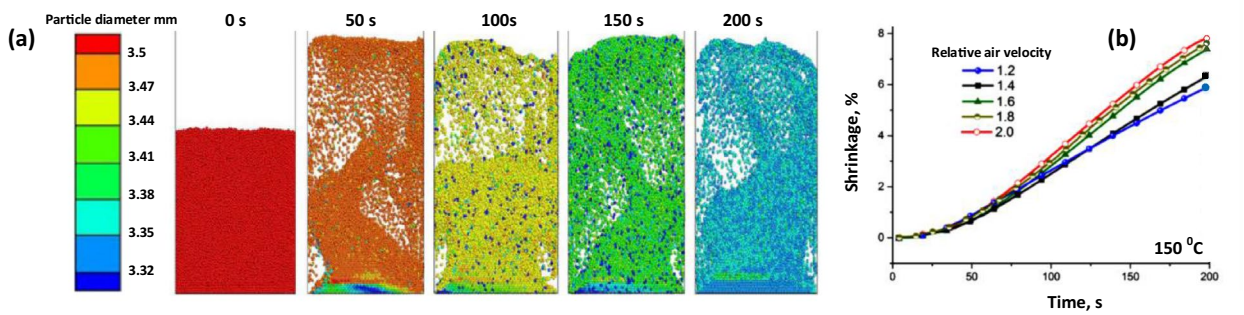

Fig. 19 **a** Snapshot of particle size change throughout the drying process, **b** effect of inlet air velocity on particle size reduction [263]

different residence times of the particles. This result is typically agreed with the previous investigation, as mentioned above. The current authors suggested thoughtfully combining the mass and heat transfer model with the air-particle flow for better simulation results that lead to optimizing the flow in the dryers.

As a result of that, Scaar et al. [262] extended the work on the developed MFD model recommended by Weigler et al. [69] using the heat and mass transfer models. Their study aims to predict the airflow distribution and investigate the effect of air duct arrangements. Based on 3-D CFD ANSYS CFX® code, two different bed materials were used: wheat and rapeseed and considered as a porous medium. The turbulence of fluid flow is modeled by an eddy viscosity approach using SST (Shear Stress Transport) $k-\omega$ model. The numerical observations were validated by experimental data which showed that the air duct arrangement has a strong influence on the airflow distribution. In addition, the horizontal air duct arrangement showed more homogeneous airflow pattern as compared to the diagonal one. Furthermore, the numerical model well calculated the influence of the bed material with its different particle characteristics which gives a good support to use this model in future investigations.

On the other hand, Azmir et al. [263] established an in-house CFD–DEM drying model for food grains considering the shrinkage characteristics to investigate the influence of inlet air temperature and velocity on drying process in the fluidized bed. Wheat particles with spherical shape are considered as a model grain where a 2-D CFD–3-D DEM are coupled by assuming only one control volume in the thickness direction, and the source in the bed thickness direction is negligible. Hot air (100°–180°) is used to dry the grains at a given velocity (1.2–2 m s^{-1}), which is introduced from the two corners of the bed. The developed drying model can successfully predict the overall particle shrinkage rate and the diameter of each particle during drying the simulation time, as shown in (Fig. 19a,b). At the studied range of air velocity, the particle shrinkage rate increases significantly with the increase of inlet air temperature but increases slightly with increasing inlet air velocity.

Azmir et al. [264] continued their research to study the influence of the grain properties such as size, density, and initial moisture content on the drying process using the same methodology of CFD–DEM coupling. Millet particles were mainly used and compared with the five same genera that all of them modeled in shape as spherical particles. Three different inlet air temperatures (50, 150, and 200 °C) are set to predict the effect of different heat transfer modes. The numerical simulations proved that the convection and conduction heat transfer has a significant influence on drying, while the contribution of the radiation mode has a negligible effect. With decreasing the grain size, the drying rate exponentially increases while the size distribution and the uniformity of moisture content decreases. Besides, decreasing the initial moisture content leads to low drying rate and make the moisture content to be homogeneous. Finally, increasing grain density occurs at a lower drying rate with longer drying time and a lower uniformity of moisture content.

A sequel, the main advantage of using computational modeling, especially CFD–DEM coupling techniques in grain drying, is the ability to study the grain and air velocity distribution through the dryer sections, which affected by geometrical modifications. Based on the previous results, the coupling approach with mass and heat transfer models will be beneficial in a realistic-industrial scale because understanding grain behavior within the dryer allows analysis of drying without requiring an expensive prototype.

7.4 Pneumatic Separation Systems

The separation process is widely used in process engineering, for example, to obtain more homogeneous fractions of material in terms of size or even in chemical characteristics. Nowadays, studies have been conducted with the simulation of fluidization of mineral particles and medicines for equipment development and process improvement. However, with the bio-particulate matter field, it still has little studies.

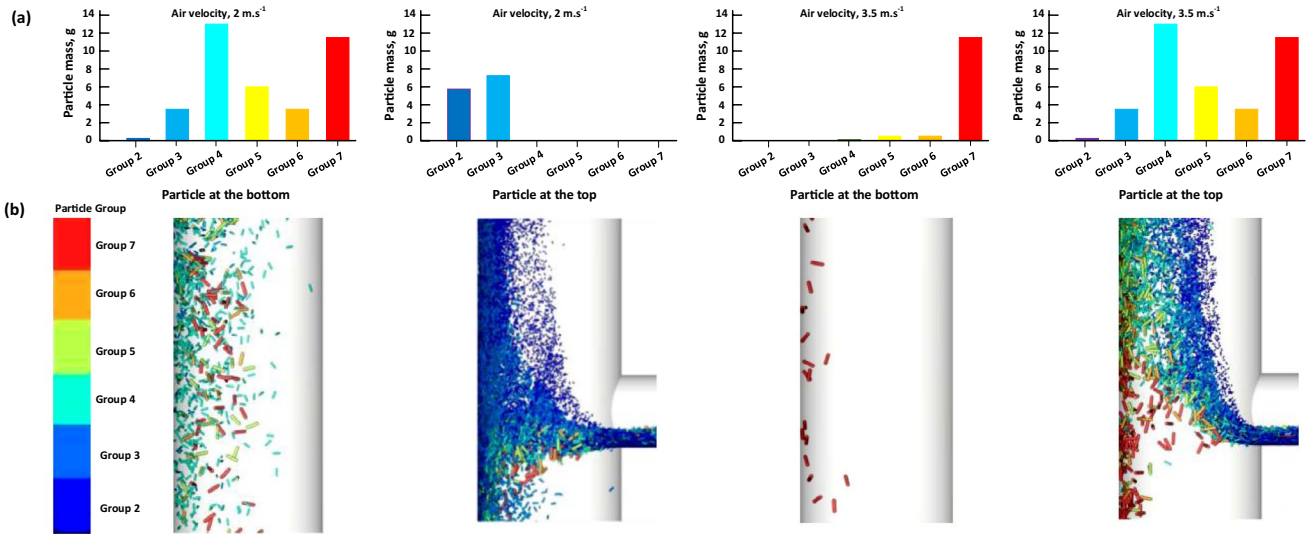

Fig. 20 **a** particle mass distributions, **b** snapshot during the simulation at the bottom and top of the riser device with different air velocities [52]

Almeida et al. [52] established a new computational model to separate the sugarcane bagasse particles pneumatically by a riser device based on CFD Ansys Fluent® and DEM Rocky® tools. One-way coupling was used referred to as the Lagrangian–Eulerian method, while the linear hysteresis model was applied to model the interaction forces between particles and boundaries. For air turbulence flow, $k-\epsilon$ turbulent model was chosen. The particles were classified into seven groups based on its characteristics and aspect ratio: group 1 as pith (fine particles), groups 2, 3, and 4 as fibers (coarse particles), and groups 5, 6, and 7 as the rind (coarse particles). The fiber and the rind particles are modeled as cylinders using Rocky® software. The pith particles will be neglected in simulation; because the air will entrain all of them due to the chosen velocities; besides, a lot of computational power and time will be consumed, making the simulations insignificant.

The chosen air velocities were set at 2.0 m s^{-1} and 3.5 m s^{-1} based on the calculated terminal velocities of the particles. During the simulation process, the particle mass distributions at the top and the bottom of the riser device with different air velocities are analyzed and visualized, as shown in (Fig. 20a,b). As a result of these data, it can be proved that the coarse particles can be easily tracked during separation even though the particles have a similar property.

The current authors continued their investigation using one-way, and two-way coupling approaches for dry and wet particles to put a theoretical basis and understand the separation phenomena resulting in developing and improving the separation equipment used for that process [29]. The same methodology of the particle modeling was followed from the previous study. The mass distribution of dry and wet bagasse collected at the top and bottom outlets of the riser at different air velocities form the two coupling approaches provided the right prediction and showed high feasibility of the separation process comparing to the experiment result. The utilized parameters and the obtained results of this simulation give a confidant for these coupling models to be extended in several processes such as drying, pyrolysis, fluidization, and gasification. It will also result in studying and developing the ideal configurations of these devices.

In this context, El-Emam et al. [35] also applied the one-way coupling approach of CFD Ansys Fluent® and DEM Rocky® codes to observe the separation behavior of Jojoba seeds from its leaves using cyclone separator. The highly curved streamlines and the chaotic turbulence of the continuum airflow in the cyclone separator were modeled through RNG $k-\epsilon$ turbulent model. The particles were modeled in shape as a sphere and custom polyhedron for the seeds and leaves, respectively. Also, the interaction forces of particle–particle and particle-boundary in the normal and tangential directions were modeled by the Hysteretic linear spring model and Linear spring coulomb limit model, respectively. Four geometrical modifications of the cyclone inlet height were used compared to the original one to optimize the performance. First, to make sure that the modeling methodology is correct, the performance validation of the original model has been carried out that showed a good between the numerical and the experimental data as shown in (Fig. 21a). Second, by tracking the number of separated seeds and the bottom of the cyclones and counting the number of leaves dragged by air at the top outlet numerically, the performance of the cyclone can be obtained as shown in (Fig. 21b).

As illustrated in (Fig. 21c), the snapshots discovered the disadvantages of the original cyclone that a considerable number of leaves concentrated in the top portion of the

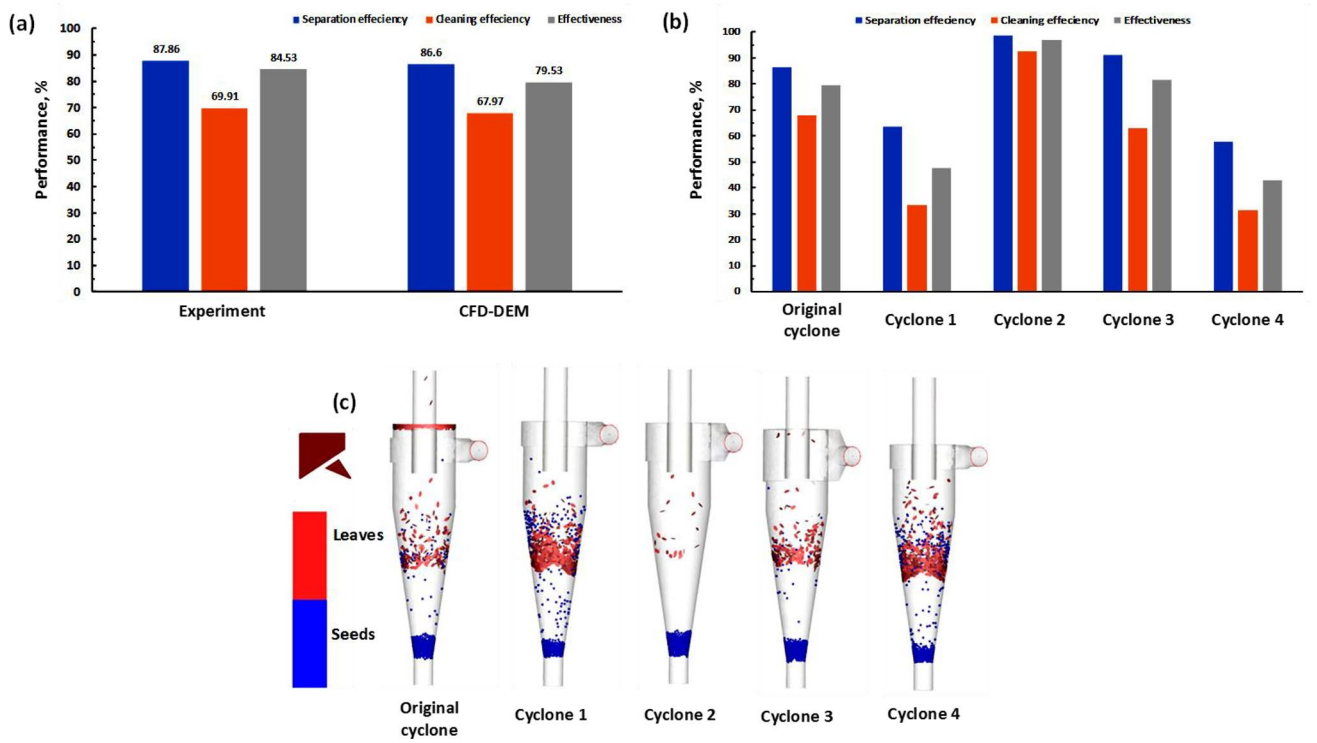

Fig. 21 **a** validation of the original model, **b** optimized cyclones performance, and (**c**) snapshot of particle separation at the end of the simulation time [35]

cyclone lead to decreasing the performance. So, by modifying the cyclone inlet height, the performance significantly improved by increasing the separation efficiency, cleaning efficiency, and effectiveness. This data was useful for considering cyclone (2) as the most suitable modified and optimized design geometry for harvesting jojoba seeds with the lowest operation cost and highest performance.

8 Challenges and Future Issues

Considerable efforts mentioned above have proved that CFD–DEM coupling is a high-potential method to investigate the bio-particulate matter by capturing its behavior characteristics in the aerodynamic systems. However, since these systems are significantly varied and complex, there are still a significant shortage and many problems in terms of determining accuracy, efficiency, and appropriate model of CFD–DEM coupling for simulations. Insufficient understanding and description of the interaction between the particle–particle, particle–fluid, and particle-boundaries give misunderstanding of the way of CFD–DEM coupling resulting in impairing the simulation modeling. Additionally, due to the limitation of computational resources and complex shape structures of grains, most of the current CFD–DEM simulations for bio-particles are a little far from being perfect enough to deal with real-particulate systems in nature or industry accurately. Besides, it is still focusing on laboratory-scale systems. On the other hand, developing an advanced process for understanding and determining contact models of irregular shapes of grains opens up the possibility of computing particle behavior (translation and rotation) in 3-D modulation and hence of obtaining high-resolution impact.

As indicated above, many models have been used for describing bio-particle shapes and perceiving particle contacts. However, each of these models has its advantages and disadvantages regarding the accuracy, flexibility, numerical stability, and efficiency, considerable challenges still exist in the bio-particles flow models especially when applying in the real world. Usually, to compute the contact force of the non-spherical grains, which are common, models that are initially constructed for the ideal spherical particles are directly used. As indicated, the last decade introduced new and advanced models, namely bounded particle model and software such as Rocky®, for simulating the irregular particles by its true and real shape. By this methodology, the simulations proved to be useful for different modeling problems in the agricultural process. Therefore, to find out and develop more efficient, accurate, and trustable models to represent different particle shapes and detect their contact forces is still one of the urgent needs and most interesting

areas to focus on in the near future. As mentioned in this review, since the current CFD–DEM coupling methods can be briefly divided into three categories: namely one-way, two-way, four-way, most of the research related to agricultural field concentrate on one-way only, while other ways are neglected which are considered more precise and accurate for representing real contacts.

One of the main bottlenecks faces CFD–DEM simulation is the massive computational cost when simulating intensive particulate systems, particularly the multiphase flow system. With typical PC hardware or workstation, three-dimensional CFD–DEM simulations are usually limited to systems with limited particle numbers, since in realistic systems, the number of particles often exceeded millions of particles. With recent developments in computer technology, parallel computing has shown great potential in accelerating computer simulations using multi-core CPU and GPU (Graphics Processing Unit). To date, using CPU and GPU platforms in the coupling CFD–DEM algorithm is still new technology compared to the traditional CPU that needs adequate development to reduce the time-consuming, especially when simulating agricultural crop grains.

Another significant problem still poses a severe challenge is simulating large ranges in grain shapes and sizes in some aerodynamic systems; also, the presence of the smallest particles in large systems requires an efficient treatment to model and simulate. Overall, modeling the bio-particulate matter process in disperse systems is a particularly open area of research that is very important for understanding agricultural processes such as precise planting, harvesting, post-harvesting, industrial, and agrophysical systems. At the same time, until now, little investigations have been done on these systems. However, the vital evaluating factors such as the validity, accuracy, speed, and versatility of the numerical technique need to be improved in the near future.

9 Summary and Conclusions

Existing literature that used CFD–DEM coupling approach to simulate aerodynamic granular systems, limited to bio-particulate matter, has been reviewed. Usually, the soft-sphere approach of DEM was commonly used to develop these grain simulations process. The advantage of soft sphere models was their capability to represent multiple particle contacts, which are of importance when modeling bulk grain systems. Particle models varied with the type of grain. For near-spherical grains such as soybean and rapeseed, single-sphere particle models predicted particle behavior with high accuracy. For non-spherical grains such as rice, wheat, and corn, particle, multi-sphere approach was used, resulting in increasing the simulation time and computational cost. That is because of the higher number of contact points requiring force and deformation calculation at each contact point. To avoid this excess computation time problem, most researchers have used single-sphere models and had reasonable success in predictions.

Depending on the software used in the simulation case, both linear and nonlinear Hertz-Mindlin contact models have been used effectively to study the aerodynamic operations such as separation and cleaning of crop grains. In general, coupling DEM with CFD has adequately simulated the separation of air-grain flow and recommended for better predictions. Although this coupling has been increasingly used to study particle processes, it has not been widely applied in agricultural grains. The considerable variation in grains characteristics such as size, shape, surface roughness, density, friction coefficients, composition, and other factors could be limiting the use of CFD–DEM. Computational cost also limits CFD–DEM application; specifically, most of the cereal crops are smaller, which need long computation time for simulation. The development of precision particle models could help spur the adoption of this numerical modeling concept and optimize process and equipment design in the grain handling and processing industry.

To date, up to the authors' investigating and searching, few studies have been made on the gas–solid flow in aerodynamic separation devices employing CFD–DEM approach. One-way coupling approach is a proper technique for predicting the behavior of macroscopic particles, where it commonly applied in agriculture systems that consume less power for simulation. In contrast, two-way and four-way are commonly used in describing the particles flow in fluidized bed related to chemical or pharmaceutical field. However, limited research used these techniques in agriculture, but it still a big gap for simulation in many aerodynamic systems related to the agriculture field. Future developments for this coupling include implementation of non-drag laws, thermal fluid-particle coupling, and mass exchange between fluid and particles should be considered.

Finally, research effort should also focus on seeking far more efficient methods for multi-phase and multi-physics problems, which are often complexly coupled together. The comparison between simulations and real experimental results showed that the CFD-DEM model is predictive and can be extended to several aerodynamic processes related to the agricultural field. Using this coupling technique and simulation methods will make it possible to improve the aerodynamic systems of agricultural machines without high costs and efforts. The obtained characteristics from the above investigations can seriously provide a basis for developing and optimizing the structural and technological parameters of the aerodynamic systems of agricultural machines.

Acknowledgements This work was supported by the National Natural Science Foundation of China (Grant Nos. 52079058 and 51979138), Nature Science Foundation for Excellent Young Scholars of Jiangsu Province (Grant No. BK20190101), National Key Research and Development Project (Grant No. 2020YFC1512404).

Declarations

Conflict of interest The authors are not aware of any biases that might be perceived as affecting the objectivity of this review. The authors also declare no conflict of interest.

References

1. Simonyan KJ, Yiljep YD (2008) Investigating grain separation and cleaning efficiency distribution of a conventional stationary Rasp-bar Sorghum Thresher. Agric Eng Int CIGR J 10:1–13
2. Wang YJ, Chung DS, Spillman CK et al (1994) Evaluation of laboratory grain cleaning and separating equipment: part I. Trans ASAE 37:507–513
3. Sokhansanj S, Fang R, Opoku A (1999) Influence of physical properties and operating conditions on particle segregation on gravity table. Appl Eng Agric. 15(5):495–499. https://doi.org/10.13031/2013.5809
4. Pouliot Y, Conway V, Leclerc P (2014) Separation and concentration technologies in food processing. In: Clark S, Jung S, Lamsal B (eds) Food processing: principles and applications, second. John Wiley and Sons Ltd, Québec, pp 33–60
5. Sosulski F (1987) Yield and functional properties of air classified protein and starch fractions from eight legume flours. J Am Chem Soc 6:363–370
6. Uhl JB, Lamp BJ (1966) Pneumatic separation of grain and straw mixtures. Trans ASAE 61–135:244–246
7. Hollatz B, Quick GR (2003) Combine tailings returns, part 1: the effects of combine performance and settings on tailings. In: International conference on crop harvesting and processing. ASABE, St. Joseph, Michigan, Louisville, Kentucky, USA, p 22
8. Tylek P, Walczyk J (2003) Critical air velocity as a separation feature in nuts of european beech (*Fagus sylvatica L.*). Electron J Polish Agric Univ, 6
9. IAEE (2008) Develop technical and technological bases improve separation of grain and seed set of physical and mechanical properties. Glevaha
10. Kotov BI, Stepanenko SP, Swiftly VA, Smith JG (2009) Design, production and operation of agricultural machinery. A Natl Interdep Sci Tech Collect 39:209–214
11. Kotov BI (2009) The theory of separation of grains in the air stream. A Natl Interdep Sci Tech Collect 39:209–214
12. Stepanenko S (2017) Research pneumatic gravity separation grain materials. Scientific proceedings V international scientific-technical conference "agricultural machinery." Glevakha, Ukraine, pp 143–145
13. Reichert RD (1982) Air classification of peas (Pisum sativum) varying widely in protein content. J Food Sci 47:1263–1267
14. Emami S, Tabil LG, Tyler RT, Crerar WJ (2007) Starch-protein separation from chickpea flour using a hydrocyclone. J Food Eng 82:460–465. https://doi.org/10.1016/j.jfoodeng.2007.03.002
15. Panasiewicz M, Sobczak P, Mazur J et al (2012) The technique and analysis of the process of separation and cleaning grain materials. J Food Eng 109:603–608. https://doi.org/10.1016/j.jfoodeng.2011.10.010
16. Hellevang KJ (1985) Pneumatic grain conveyors. Fargo, North Dakota
17. Piven VV (2018) Determination of the extent of fraction in air separation of grain material. J Phys Conf Ser. https://doi.org/10.1088/1742-6596/1059/1/012001
18. Clarke B (1985) Cleaning seeds by fluidization. J Agric Eng Res 31:231–242. https://doi.org/10.1016/0021-8634(85)90090-3
19. Gorial BY, O'Callaghan JR (1990) Aerodynamic properties of grain/straw materials. J Agric Eng Res 46:275–290. https://doi.org/10.1016/S0021-8634(05)80132-5
20. Zewdu AD (2007) Aerodynamic properties of tef grain and straw material. Biosyst Eng 98:304–309. https://doi.org/10.1016/j.biosystemseng.2007.08.003
21. Samantaray SK, Mohapatra SS, Munshi B (2018) Experimental findings and analysis of terminal velocity and drag coefficient of Raschig Ring in vertical and inclined channel. Powder Technol 340:440–448. https://doi.org/10.1016/j.powtec.2018.09.030
22. Zhang L, Honaker R, Liu W et al (2015) Calculation of terminal velocity in transitional flow for spherical particle. Int J Min Sci Technol 25:311–317. https://doi.org/10.1016/j.ijmst.2015.02.022
23. Czernik Z (1983) Studies of aerodynamical features of seeds of Scotch pine, Norway spruce and European larch (Badania wlasciwosci aerodynamicznych nasion sosny zwyczajnej, swierka pospolitego i modrzewia europejskieg). Sylwan 9:31–40
24. Ghamari S, Borghei AM, Rabbani H et al (2010) Modeling the terminal velocity of agricultural seeds with artificial neural networks. Afr J Agric Res 5:389–398. https://doi.org/10.5897/AJAR09.626
25. Khodabakhshian R, Emadi B, Khojastehpour M, Golzarian MR (2018) Aerodynamic separation and cleaning of pomegranate arils from rind and white segments (locular septa). J Saudi Soc Agric Sci 17:61–68. https://doi.org/10.1016/j.jssas.2016.01.003
26. Mohsenin NN (1986) Physical properties of plant and animal materials. Gordon and Breach Science, New York
27. Tylek P, Walczyk J (2004) Effectiveness of the pneumatic separation of Norway spruce *Picea abies* (L.) Karst seeds. Dendrobiology 51:101–104
28. Levenspiel O, Haider A (1989) Drag coefficient and terminal velocity of spherical and nonspherical particles. Powder Technol 58:63–70. https://doi.org/10.1016/0032-59109(89)80008-7
29. De AE, Spogis N, Taranto OP, Silva MA (2019) Theoretical study of pneumatic separation of sugarcane bagasse particles. Biomass Bioenerg 127:105256. https://doi.org/10.1016/j.biombioe.2019.105256
30. Lapple CE (1951) Fluid and particle mechanics, 1st edn. University of Delaware, Newark
31. Hauhouot-O'Hara M, Criner BR, Brusewitz GH, Solie JB (2000) Selected physical characteristics and aerodynamic properties of cheat seed for separation from wheat. J Sci Res Dev, 2
32. Afonso Júnior PC, Corrêa PC, Pinto FAC, Queiroz DM (2007) Aerodynamic properties of coffee cherries and beans. Biosyst Eng 98:39–46. https://doi.org/10.1016/j.biosystemseng.2007.03.010
33. Shellard JE, Macmillan RH (1978) Aerodynamic properties of threshed wheat materials. J Agric Eng Res 23:273–281. https://doi.org/10.1016/0021-8634(78)90101-4
34. Shahbazi F (2013) Aerodynamic properties of wild mustard (*Sinapis arvensis* L.) seed for separation from canola. J Sci Food Agric 93:1466–1470. https://doi.org/10.1002/jsfa.5916
35. El-Emam MA, Shi W, Zhou L (2019) CFD-DEM simulation and optimization of gas-cyclone performance with realistic macroscopic particulate matter. Adv Powder Technol 30:2686–2702. https://doi.org/10.1016/j.apt.2019.08.015
36. Binelo MO, de Lima RF, Khatchatourian OA, Stránský J (2019) Modelling of the drag force of agricultural seeds applied to the

discrete element method. Biosyst Eng 178:168–175. https://doi.org/10.1016/j.biosystemseng.2018.11.013
37. Khatchatourian OA, Binelo MO, de Lima RF (2014) Simulation of soya bean flow in mixed-flow dryers using DEM. Biosyst Eng 123:68–76. https://doi.org/10.1016/j.biosystemseng.2014.05.003
38. Guo Y, Curtis JS (2015) Discrete element method simulations for complex granular flows. Annu Rev Fluid Mech 47:21–46. https://doi.org/10.1146/annurev-fluid-010814-014644
39. Li H, Li Y, Gao F et al (2012) CFD-DEM simulation of material motion in air-and-screen cleaning device. Comput Electron Agric 88:111–119. https://doi.org/10.1016/j.compag.2012.07.006
40. Ren B, Zhong W, Chen Y et al (2012) CFD-DEM simulation of spouting of corn-shaped particles. Particuology 10:562–572. https://doi.org/10.1016/j.partic.2012.03.011
41. Liu X, Gan J, Zhong W, Yu A (2019) Particle shape effects on dynamic behaviors in a spouted bed: CFD-DEM study. Powder Technol. https://doi.org/10.1016/j.powtec.2019.07.099
42. Han D, Zhang D, Jing H et al (2018) DEM-CFD coupling simulation and optimization of an inside-filling air-blowing maize precision seed-metering device. Comput Electron Agric 150:426–438. https://doi.org/10.1016/j.compag.2018.05.006
43. Tsuji Y (2007) Multi-scale modeling of dense phase gas–particle flow. Chem Eng Sci 62:3410–3418
44. Tsuji Y, Tanaka T, Ishida T (1992) Lagrangian numerical-simulation of plug flow of cohesionless particles in ahorizontal pipe. Powder Technol 71:239–250
45. Zhou ZY, Kuang SB, Chu KW, Yu AB (2010) Assessments of CFD–DEM models in particle–fluid flow modelling. J Fluid Mech 661:482–510
46. Wang B, Chu KW, Yu AB (2007) Numerical study of particle–fluid flow in a hydrocyclone. Ind Eng Chem Res 46:4695–4705
47. Xu BH, Yu AB (1997) Numerical simulation of the gas–solid flow in a fluidized bed by combining discrete particle method with computational fluid dynamics. Chem Eng Sci 52:2785–2809
48. Chu KW, Wang B, Yu AB, Vince A (2009) CFD–DEM modelling of multiphase flow in dense medium cyclones. PowderTechnology 193:235–247
49. Cortés C, Gil A (2007) Modeling the gas and particle flow inside cyclone separators. Prog Energy Combust Sci 33:409–452. https://doi.org/10.1016/j.pecs.2007.02.001
50. Derksen JJ, Sundaresan S, van den Akker HEA (2006) Simulation of mass-loading effects in gas-solid cyclone separators. Powder Technol 163:59–68. https://doi.org/10.1016/B978-008044544-1/50089-3
51. Horabik J, Molenda M (2016) Parameters and contact models for DEM simulations of agricultural granular materials: a review. Biosyst Eng 147:206–225. https://doi.org/10.1016/j.biosystemseng.2016.02.017
52. Almeida E, Spogis N, Silva MA (2016) Computational study of the pneumatic separation of sugarcane bagasse. In: Nzihou A (ed), 6th international conference on engineering for waste and biomass valorisation. Albi : Mines Albi, 2016, Albi, France, pp 1–16
53. Fonte CB, Jr JAAO, Almeida LC De (2015) Dem-Cfd coupling : mathematical modelling and case studies using Rocky-Dem ® and Ansys Fluent ®. In: Eleventh international conference on CFD in the minerals and process industries. CSIRO Organization, Melbourne, Australia, pp 1–7
54. Chu KW, Wang B, Xu DL et al (2011) CFD-DEM simulation of the gas-solid flow in a cyclone separator. Chem Eng Sci 66:834–847. https://doi.org/10.1016/j.ces.2010.11.026
55. Romaní Fernández X, Nirschl H (2013) Simulation of particles and sediment behaviour in centrifugal field by coupling CFD and DEM. Chem Eng Sci 94:7–19. https://doi.org/10.1016/j.ces.2013.02.039
56. Wang Y, Williams K, Jones M, Chen B (2017) CFD simulation methodology for gas-solid flow in bypass pneumatic conveying: a review. Appl Therm Eng 125:185–208. https://doi.org/10.1016/j.applthermaleng.2017.05.063
57. Ullah A, Hong K, Gao Y et al (2019) An overview of Eulerian CFD modeling and simulation of non-spherical biomass particles. Renew Energy 141:1054–1066. https://doi.org/10.1016/j.renene.2019.04.074
58. Norouzi HR, Zarghami R, Sotudeh-gharebagh R, Mostoufi N (2016) Coupled CFD-DEM modeling : formulation, implementation and application to multiphase flows. Wiley, New York
59. Boac JM, Ambrose RPK, Casada ME et al (2014) Applications of discrete element method in modeling of grain postharvest operations. Food Eng Rev 6:128–149. https://doi.org/10.1007/s12393-014-9090-y
60. Cundall PA, Strack ODL (1979) A discrete numerical model for granular assemblies. Géotechnique 29:47–65. https://doi.org/10.1680/geot.1979.29.1.47
61. Dewicki G (2003) Bulk material handling and processing: numerical techniques and simulation of granular material. Bulk Solids Handl Int J Storing Handl Bulk Mater 23:110–113
62. Zhu HP, Zhou ZY, Yang RY, Yu AB (2007) Discrete particle simulation of particulate systems: theoretical developments. Chem Eng Sci 62:3378–3396. https://doi.org/10.1016/j.ces.2006.12.089
63. Berger R, Kloss C, Kohlmeyer A, Pirker S (2015) Hybrid parallelization of the LIGGGHTS open-source DEM code. Powder Technol 278:234–247. https://doi.org/10.1016/j.powtec.2015.03.019
64. Theuerkauf J, Dhodapkar S, Jacob K (2007) Modeling granular flow using discrete element method—from theory to practice. Chem Eng 114:154–162
65. Williams JR, Hocking G, Mustoe G (1985) The theoretical basis of the discrete element method. In: NUMETA '85 conference. Balkema, Rotterdam, pp 897–906
66. Zhu HP, Zhou ZY, Yang RY, Yu AB (2008) Discrete particle simulation of particulate systems: a review of major applications and findings. Chem Eng Sci 63:5728–5770. https://doi.org/10.1016/j.ces.2008.08.006
67. Keppler I, Kocsis L, Oldal I et al (2012) Grain velocity distribution in a mixed flow dryer. Adv Powder Technol 23:824–832. https://doi.org/10.1016/j.apt.2011.11.003
68. Zhang X, Vu-Quoc L (2000) Simulation of chute flow of soybeans using an improved tangential force-displacement model. Mech Mater 32:115–129. https://doi.org/10.1016/S0167-6636(99)00043-5
69. Weigler F, Scaar H, Mellmann J (2012) Investigation of particle and air flows in a mixed-flow dryer. Dry Technol 30:1730–1741. https://doi.org/10.1080/07373937.2012.703742
70. Sturm M, Wirtz S, Scherer V, Denecke J (2010) Coupled DEM-CFD simulation of pneumatically conveyed granular media. Chem Eng Technol 33:1184–1192. https://doi.org/10.1002/ceat.201000162
71. Lim EWC, Wang CH, Yu AB (2006) Discrete element simulation for pneumatic conveying of granular material. AIChE J 52:496–509. https://doi.org/10.1002/aic.10645
72. Parafiniuk P, Molenda M, Horabik J (2013) Discharge of rapeseeds from a model silo: physical testing and discrete element method simulations. Comput Electron Agric 97:40–46. https://doi.org/10.1016/j.compag.2013.06.008
73. Raji AO, Favier JF (2004) Model for the deformation in agricultural and food particulate materials under bulk compressive loading using discrete element method. II: Compression of oilseeds. J Food Eng 64:373–380. https://doi.org/10.1016/j.jfoodeng.2003.11.005

74. Anand A, Curtis JS, Wassgren CR et al (2009) Predicting discharge dynamics of wet cohesive particles from a rectangular hopper using the discrete element method (DEM). Chem Eng Sci 64:5268–5275. https://doi.org/10.1016/j.ces.2009.09.001
75. Sakaguchi E, Suzuki M, Favier JF, Kawakami S (2001) Numerical simulation of the shaking separation of Paddy and Brown rice using the discrete element method. J Agric Eng Res 79:307–315. https://doi.org/10.1006/jaer.2001.0706
76. Ma Z, Li Y, Xu L (2015) Discrete-element method simulation of agricultural particles' motion in variable-amplitude screen box. Comput Electron Agric 118:92–99. https://doi.org/10.1016/j.compag.2015.08.030
77. Lenaerts B, Aertsen T, Tijskens E et al (2014) Simulation of grain-straw separation by discrete element modeling with bendable straw particles. Comput Electron Agric 101:24–33. https://doi.org/10.1016/j.compag.2013.12.002
78. Woo MW, Daud WRW, Mujumdar AS et al (2010) Role of rheological characteristics in amorphous food particle-wall collisions in spray drying. Powder Technol 198:251–257. https://doi.org/10.1016/j.powtec.2009.11.015
79. Adewumi BA (2008) 2D modeling of grain transport and separation in the horizontal air stream. In: Food processing automation conference CD-Rom, pp 1–10
80. Guo Y, Wu CY, Kafui KD, Thornton C (2011) 3D DEM/CFD analysis of size-induced segregation during die filling. Powder Technol 206:177–188. https://doi.org/10.1016/j.powtec.2010.05.029
81. Lei X, Liao Y, Liao Q (2016) Simulation of seed motion in seed feeding device with DEM-CFD coupling approach for rapeseed and wheat. Comput Electron Agric 131:29–39. https://doi.org/10.1016/j.compag.2016.11.006
82. Li J, Webb C, Pandiella SS, Campbell GM (2002) A numerical simulation of separation of crop seeds by screening: effect of particle bed depth. Food Bioprod Process Trans Inst Chem Eng Part C 80:109–117. https://doi.org/10.1205/096030802529387 44
83. Li J, Webb C, Pandiella SS, Campbell GM (2003) Discrete particle motion on sieves: a numerical study using the DEM simulation. Powder Technol 133:190–202. https://doi.org/10.1016/S0032-5910(03)00092-5
84. Boac JM, Casada ME, Maghirang RG, Harner JP (2012) 3-D and quasi-2-d discrete element modeling of grain commingling in a bucket elevator boot system. Trans ASABE 55:659–672
85. González-Montellano C, Baguena EM, Ramírez-Gómez Á, Barreiro P (2014) Discrete element analysis for the assessment of the accuracy of load cell-based dynamic weighing systems in grape harvesters under different ground conditions. Comput Electron Agric 100:13–23. https://doi.org/10.1016/j.compag.2013.10.008
86. Van Zeebroeck M, Tijskens E, Dintwa E et al (2006) The discrete element method (DEM) to simulate fruit impact damage during transport and handling: model building and validation of DEM to predict bruise damage of apples. Postharvest Biol Technol 41:85–91. https://doi.org/10.1016/j.postharvbio.2006.02.007
87. Ramírez-Gómez Á, Gallego E, Fuentes JM et al (2014) Values for particle-scale properties of biomass briquettes made from agroforestry residues. Particuology 12:100–106. https://doi.org/10.1016/j.partic.2013.05.007
88. Cundall PA (1988) Detect and represent contacts in a system composed of many polyhedral blocks. Int J Rock Mech Min Sci Geomech 25:107–116
89. Hart R, Cundall PA, Lemos J (1988) Formulation of a three-dimensional distinct element model-part II. Mechanical calculations for motion and interaction of a system composed of many polyhedral blocks. Int J Rock Mech Min Sci 25:117–125. https://doi.org/10.1016/0148-9062(88)92294-2
90. Kosinski P, Hoffmann AC (2010) An extension of the hard-sphere particle-particle collision model to study agglomeration. Chem Eng Sci 65:3231–3239. https://doi.org/10.1016/j.ces.2010.02.012
91. O'Sullivan C (2011) Particle-based discrete element modeling: geomechanics perspective. Int J Geomech 11:449–464. https://doi.org/10.1061/(asce)gm.1943-5622.0000024
92. O'Sullivan C (2011) Particulate discrete element modelling : a geomechanics perspective, 1st edn. Spon Press, New York
93. Hoomans BPB, Kuipers JAM, Briels WJ, Van Swaaij WPM (1996) Discrete particle simulation of bubble and slug formation in a two-dimensional gas-fluidized bed: a hard-sphere approch. Chem Eng Sci 51:99–118. https://doi.org/10.1016/0009-2509(95)00271-5
94. Fortin J, Millet O, de Saxcé G (2005) Numerical simulation of granular materials by an improved discrete element method. Int J Numer Methods Eng 62:639–663. https://doi.org/10.1002/nme.1209
95. Duran J (2000) Sands, powders, and grains: an introduction to the physics of granular materials. Springer, New York
96. Tsuji Y, Kawaguchi T, Tanaka T (1993) Discrete particle simulation of two-dimensional fluidized bed. Powder Technol 77:79–87. https://doi.org/10.1016/0032-5910(93)85010-7
97. Zhao J, Shan T (2013) Coupled CFD-DEM simulation of fluid-particle interaction in geomechanics. Powder Technol 239:248–258. https://doi.org/10.1016/j.powtec.2013.02.003
98. Campbell CS (2006) Granular material flows: an overview. Powder Technol 162:208–229. https://doi.org/10.1016/j.powtec.2005.12.008
99. Delaney GW, Inagaki S, Aste T (2007) Fine tuning DEM simulations to perform virtual experiments with three-dimensional granular packings. In: Tomaso A, Di MT, Tordesillas A (eds) Granular and complex materials. World Scientific, Singapore, pp 141–168
100. Crowe CT, Schwarzkopf JD, Sommerfeld M, Tsuji Y (2011) Multiphase flows with droplets and particles, 2nd edn. CRC Press, Taylor and Francis Group, Boca Raton
101. Carlos Varas AE, Peters EAJF, Kuipers JAM (2017) CFD-DEM simulations and experimental validation of clustering phenomena and riser hydrodynamics. Chem Eng Sci 169:246–258. https://doi.org/10.1016/j.ces.2016.08.030
102. He Y, Bayly AE, Hassanpour A (2018) Coupling CFD-DEM with dynamic meshing: a new approach for fluid-structure interaction in particle-fluid flows. Powder Technol 325:620–631. https://doi.org/10.1016/j.powtec.2017.11.045
103. Neuwirth J, Antonyuk S, Heinrich S, Jacob M (2013) CFD-DEM study and direct measurement of the granular flow in a rotor granulator. Chem Eng Sci 86:151–163. https://doi.org/10.1016/j.ces.2012.07.005
104. Kuang SB, Yu AB, Zou ZS (2009) Computational study of flow regimes in vertical pneumatic conveying. Ind Eng Chem Res 48:6846–6858
105. Akhshik S, Behzad M, Rajabi M (2015) CFD-DEM approach to investigate the effect of drill pipe rotation on cuttings transport behavior. J Pet Sci Eng 127:229–244. https://doi.org/10.1016/j.petrol.2015.01.017
106. Boac JM, Casada ME, Maghirang RG (2010) Material and interaction properties of selected grains and oilseeds for modeling discrete particles. Trans ASABE. 53:1201–1216. https://doi.org/10.13031/2013.32577
107. ESSS-Rocky (2018) Rocky-Dem technical manual. In: Rocky E (ed) Models used in Rocky, 4.13. ESSS, Rio de Janeiro, Brazi, pp 3–11
108. Cundall PA (1988) Computer simulations of dense sphere assemblies. Micromech Granul Mater 20:113–123. https://doi.org/10.1016/B978-0-444-70523-5.50021-7

109. Timoshenko SP, Goodier JN (1970) Theory of elasticity, 3rd edn. McGraw-Hill, New York
110. ASAE S368.4 (2001) Compression test of food materials of convex shape, revised. ASAE, Michigan
111. Antypov D, Elliott JA (2011) On an analytical solution for the damped Hertzian spring. Europhys Lett. https://doi.org/10.1209/0295-5075/94/50004
112. Walton OR, Braun RL (1986) Viscosity, granular-temperature, and stress calculations for shearing assemblies of inelastic, frictional disks. J Rheol (NY) 30:949–980. https://doi.org/10.1122/1.549893
113. Tomas J (2000) Particle adhesion fundamentals and bulk powder consolidation. KONA Powder Part J 18:157–169. https://doi.org/10.14356/kona.2000022
114. Luding S (2008) Cohesive, frictional powders: contact models for tension. Granul Matter 10:235–246. https://doi.org/10.1007/s10035-008-0099-x
115. Freireich B, Litster J, Wassgren C (2009) Using the discrete element method to predict collision-scale behavior: a sensitivity analysis. Chem Eng Sci 64:3407–3416. https://doi.org/10.1016/j.ces.2009.04.019
116. Walton OR (1993) Numerical simulation of inelastic, frictional particle-particle interactions. In: Roco MC (ed) Particulate two-phase flow. Butterworth-Heinemann, Adivision of Reed Publishing (USA) Inc., Reed, pp 855–947
117. Bartsch P, Zunft S (2019) Granular flow around the horizontal tubes of a particle heat exchanger : DEM-simulation and experimental validation. Sol Energy 182:48–56. https://doi.org/10.1016/j.solener.2019.01.086
118. Vivacqua V, López A, Hammond R et al (2019) DEM analysis of the effect of particle shape, cohesion and strain rate on powder rheometry. Powder Technol 342:653–663. https://doi.org/10.1016/j.powtec.2018.10.034
119. Seville JPK, Willett CD, Knight PC (2000) Interparticle forces in fluidisation.pdf. Powder Technol 113:261–268. https://doi.org/10.1016/S0032-5910(00)00309-0
120. Schwager T, Pöschel T (2007) Coefficient of restitution and linear-dashpot model revisited. Granul Matter 9:465–469. https://doi.org/10.1007/s10035-007-0065-z
121. Van Zeebroeck M, Tijskens E, Van Liedekerke P et al (2003) Determination of the dynamical behaviour of biological materials during impact using a pendulum device. J Sound Vib 266:465–480. https://doi.org/10.1016/S0022-460X(03)00579-0
122. Stropek Z, Gołacki K (2015) A new method for measuring impact related bruises in fruits. Postharvest Biol Technol 110:131–139. https://doi.org/10.1016/j.postharvbio.2015.07.005
123. Deresiewicz H, Mindlin RD (1953) Elastic spheres in contact under varying oblique forces. J Appl Mech 20:327–344
124. Vu-Quoc L, Zhang X, Walton OR (2000) A 3-D discrete-element method for dry granular flows of ellipsoidal particles. Comput Methods Appl Mech Eng 187:483–528. https://doi.org/10.1016/S0045-7825(99)00337-0
125. Di Renzo A, Di Maio FP (2004) Comparison of contact-force models for the simulation of collisions in DEM-based granular flow codes. Chem Eng Sci 59:525–541. https://doi.org/10.1016/j.ces.2003.09.037
126. Łukaszuk J, Molenda M, Horabik J, Wiącek J (2009) Method of measurement of coefficient of friction between pairs of metallic and organic objects. Acta Agrophys 13:407–418
127. Nyembwe AM, Cromarty RD (2019) Simulation of the pressure drop across granulated mixtures using a coupled DEM–CFD model. Adv Powder Technol 30:85–97. https://doi.org/10.1016/j.apt.2018.10.010
128. Sun J, Battaglia F, Subramaniam S (2006) Dynamics and structures of segregation in a dense, vibrating granular bed. Phys Rev E 74:061307. https://doi.org/10.1103/PhysRevE.74.061307
129. Mousaviraad M, Tekeste MZ, Rosentrater KA (2017) Calibration and validation of a discrete element model of corn using grain flow simulation in a commercial screw grain auger. Trans ASABE 60:1403–1415. https://doi.org/10.13031/trans.12200
130. Chan EL, Washino K (2018) Coarse grain model for DEM simulation of dense and dynamic particle flow with liquid bridge forces. Chem Eng Res Des 132:1060–1069. https://doi.org/10.1016/j.cherd.2017.12.033
131. Olaleye AK, Shardt O, Walker GM, Van Den AH (2019) Pneumatic conveying of cohesive dairy powder: experiments and CFD-DEM simulations. Powder Technol. https://doi.org/10.1016/j.powtec.2019.09.046
132. Sakai M, Takahashi H, Pain CC et al (2012) Study on a large-scale discrete element model for fine particles in a fluidized bed. Adv Powder Technol 23:673–681. https://doi.org/10.1016/j.apt.2011.08.006
133. Sorace CM, Louge MY, Crozier MD, Law VHC (2009) High apparent adhesion energy in the breakdown of normal restitution for binary impacts of small spheres at low speed. Mech Res Commun 36:364–368. https://doi.org/10.1016/j.mechrescom.2008.10.009
134. Althaus TO, Windhab EJ, Scheuble N (2012) Effect of pendular liquid bridges on the flow behavior of wet powders. Powder Technol 217:599–606. https://doi.org/10.1016/j.powtec.2011.11.026
135. Johnson KL, Kendall K, Roberts AD (1971) Surface charge and the contact of elastic solids. Proceeding R Soc London 324:301–313. https://doi.org/10.1088/0022-3727/6/9/304
136. Nase ST, Vargas WL, Abatan AA, McCarthy JJ (2001) Discrete characterization tools for cohesive granular material. Powder Technol 116:214–223. https://doi.org/10.1016/S0032-5910(00)00398-3
137. Favier JF, Abbaspour-Fard MH, Kremmer M, Raji AO (1999) Shape representation of axisymmetrical, non-spherical particles in discrete element simulation using multi-element model particles. Eng Comput 16:467–480. https://doi.org/10.1108/02644409910271894
138. Hogu C (1998) Shape representation and contact detection for discrete element simulations of arbitrary geometries. Eng Comput 15:374–390
139. Zhong W, Yu A, Liu X et al (2016) DEM/CFD-DEM modelling of non-spherical particulate systems: theoretical developments and applications. Powder Technol 302:108–152. https://doi.org/10.1016/j.powtec.2016.07.010
140. Kureck H, Govender N, Siegmann E et al (2019) Industrial scale simulations of tablet coating using GPU based DEM : a validation study. Chem Eng Sci 202:462–480. https://doi.org/10.1016/j.ces.2019.03.029
141. ISO 3435 (1977) Continuous mechanical handling equipment classification and symbolization of bulk materials. Geneva: International Organization for Standardization
142. Zhan Z, Yaoming L, Zhenwei L, Zhiqiang G (2013) DEM simulation and physical testing of rice seed impact against a grain loss sensor. Biosyst Eng 116:410–419. https://doi.org/10.1016/j.biosystemseng.2013.10.002
143. Athanassiadis AG, Miskin MZ, Kaplan P et al (2014) Particle shape effects on the stress response of granular packings. Soft Matter 10:48–59. https://doi.org/10.1039/c3sm52047a
144. Kruggel-Emden H, Rickelt S, Wirtz S, Scherer V (2008) A study on the validity of the multi-sphere discrete element method. Powder Technol 188:153–165. https://doi.org/10.1016/j.powtec.2008.04.037
145. Saeed MK, Siraj MS (2019) Mixing study of non-spherical particles using DEM. Powder Technol 344:617–627. https://doi.org/10.1016/j.powtec.2018.12.057

146. Markauskas D, Kačianauskas R (2011) Investigation of rice grain flow by multi-sphere particle model with rolling resistance. Granul Matter 13:143–148. https://doi.org/10.1007/s10035-010-0196-5
147. Wiacek J, Molenda M, Horabik J, Ooi JY (2012) Influence of grain shape and intergranular friction on material behavior in uniaxial compression: experimental and DEM modeling. Powder Technol 217:435–442. https://doi.org/10.1016/j.powtec.2011.10.060
148. Markauskas D, Kačianauskas R, Džiugys A, Navakas R (2010) Investigation of adequacy of multi-sphere approximation of elliptical particles for DEM simulations. Granul Matter 12:107–123. https://doi.org/10.1007/s10035-009-0158-y
149. Ma H, Zhao Y (2017) Modeling of the flow of ellipsoidal particles in a horizontal rotating drum based on DEM simulation. Chem Eng Sci 172:636–651. https://doi.org/10.1016/j.ces.2017.07.017
150. Zhou Z, Zou R, Pinson D, Yu A (2011) Dynamic simulation of the packing of ellipsoidal particles. Ind Eng Chem Res 50:9787–9798. https://doi.org/10.1021/ie200862n
151. Luo X, Zhao L, Zhang S et al (2018) Experimental and DEM studies on the distribution of voidage in the random filling bed of ellipsoidal particles. Powder Technol 340:400–410. https://doi.org/10.1016/j.powtec.2018.09.042
152. Ma H, Zhao Y, Cheng Y (2019) CFD-DEM modeling of rod-like particles in a fl uidized bed with complex geometry. Powder Technol 344:673–683. https://doi.org/10.1016/j.powtec.2018.12.066
153. Chen H, Zhao S, Zhou X (2019) DEM investigation of angle of repose for super-ellipsoidal particles. Particuology. https://doi.org/10.1016/j.partic.2019.05.005
154. Zhao Y, Xu L, Umbanhowar PB, Lueptow RM (2019) Discrete element simulation of cylindrical particles using super-ellipsoids. Particuology 46:55–66. https://doi.org/10.1016/j.partic.2018.04.007
155. Baran O, Eppinger T, Han K (2018) DEM simulation of cylinders and capsules in a fluidized bed. In: 8th world congress on particle technology, Orlando, pp 232–242
156. Zhong WQ, Zhang Y, Jin B, Zhang M (2009) Discrete element method simulation of cylinder-shaped particle flow in a gas-solid fluidized bed. Chem Eng Technol 32:386–391. https://doi.org/10.1002/ceat.200800516
157. Wu M, Peters B, Rosemann T, Kruggel-emden H (2019) A forcing fictitious domain method to simulate fluid-particle interaction of particles with super-quadric shape. Powder Technol. https://doi.org/10.1016/j.powtec.2019.09.088
158. Lu G, Third JR (2012) Critical assessment of two approaches for evaluating contacts between super-quadric shaped particles in DEM simulations. Chem Eng Sci 78:226–235. https://doi.org/10.1016/j.ces.2012.05.041
159. Wang S, Fan Y, Ji S (2018) Interaction between super-quadric particles and triangular elements and its application to hopper discharge. Powder Technol 339:534–549. https://doi.org/10.1016/j.powtec.2018.08.026
160. Metzger MJ, Glasser BJ (2013) Simulation of the breakage of bonded agglomerates in a ball mill. Powder Technol 237:286–302. https://doi.org/10.1016/j.powtec.2012.12.006
161. Potyondy DO, Cundall PA (2004) A bonded-particle model for rock. Int J Rock Mech Min Sci 41:1329–1364. https://doi.org/10.1016/j.ijrmms.2004.09.011
162. Spettl A, Bachstein S, Dosta M et al (2016) Bonded-particle extraction and stochastic modeling of internal agglomerate structures. Adv Powder Technol 27:1761–1774. https://doi.org/10.1016/j.apt.2016.06.007
163. Park B, Min K, Thompson N, Horsrud P (2018) Three-dimensional bonded-particle discrete element modeling of mechanical behavior of transversely isotropic rock. Int J Rock Mech Min Sci 110:120–132. https://doi.org/10.1016/j.ijrmms.2018.07.018
164. Govender N, Wilke DN, Pizette P, Abriak N (2018) A study of shape non-uniformity and poly-dispersity in hopper discharge of spherical and polyhedral particle systems using the Blaze-DEM GPU code. Appl Math Comput 319:318–336. https://doi.org/10.1016/j.amc.2017.03.037
165. Nezami EG, Hashash YMA, Zhao D, Ghaboussi J (2007) Simulation of front end loader bucket–soil interaction using discrete element method. Int J Numer Anal Methods Geomech 31:1147–1162. https://doi.org/10.1002/nag.594
166. Li X, Wang F, Zhang D et al (2019) Fluid-solid interaction simulation for particles and walls of arbitrary polygonal shapes with a coupled LBM-IMB-DEM method. Powder Technol 356:177–192. https://doi.org/10.1016/j.powtec.2019.08.006
167. Peña AA, Lind PG, Herrmann HJ (2008) Modeling slow deformation of polygonal particles using DEM. Particuology 6:506–514. https://doi.org/10.1016/j.partic.2008.07.009
168. Fu X, Yao Z, Zhang X (2017) Numerical simulation of polygonal particles moving in incompressible viscous fluids. Particuology 31:140–151. https://doi.org/10.1016/j.partic.2016.05.016
169. Džiugys A, Peters B (2001) An approach to simulate the motion of spherical and non-spherical fuel particles in combustion chambers. Granul Matter 3:231–265
170. Locurto GJ, Zhang X, Zakirov V et al (1997) Soybean impacts: experiments and dynamic simulations. Trans ASAE 40:789–794
171. Xu T, Yu J, Yu Y, Wang Y (2018) A modelling and verification approach for soybean seed particles using the discrete element method. Adv Powder Technol 29:3274–3290. https://doi.org/10.1016/j.apt.2018.09.006
172. Jiang G, Qiu B (2011) Discrete element method simulation of impact-based measurement of grain mass flow. In: 2011 international conference on computer distributed control and intelligent environmental monitoring. IEEE, Changsha, China, pp 419–422
173. Coetzee CJ, Els DNJ (2009) Calibration of discrete element parameters and the modelling of silo discharge and bucket filling. Comput Electron Agric 65:198–212. https://doi.org/10.1016/j.compag.2008.10.002
174. Chung YC, Ooi JY (2008) A study of influence of gravity on bulk behaviour of particulate solid. Particuology 6:467–474. https://doi.org/10.1016/j.partic.2008.07.017
175. González-Montellano C, Ramírez A, Fuentes JM, Ayuga F (2012) Numerical effects derived from en masse filling of agricultural silos in DEM simulations. Comput Electron Agric 81:113–123. https://doi.org/10.1016/j.compag.2011.11.013
176. Markauskas D, Ramírez-Gómez Á, Kačianauskas R, Zdancevičius E (2015) Maize grain shape approaches for DEM modelling. Comput Electron Agric 118:247–258. https://doi.org/10.1016/j.compag.2015.09.004
177. Wiacek J, Molenda M (2011) Moisture-dependent physical properties of rapeseed: experimental and DEM modeling. Int Agrophys 25:59–65
178. Wojtkowski M, Pecen J, Horabik J, Molenda M (2010) Rapeseed impact against a flat surface: physical testing and DEM simulation with two contact models. Powder Technol 198:61–68. https://doi.org/10.1016/j.powtec.2009.10.015
179. Molenda M, Horabik J, Łukaszuk J, Wiacek J (2011) Variability of intergranular friction and its role in DEM simulation of direct shear of an assembly of rapeseeds. Int Agrophys 25:361–368
180. Sarnavi HJ, Noor Mohammadi A, Modares Motlagh A, Rahmani Didar A (2013) Dem model of wheat grains in storage considering the effect of moisture content in direct shear test. Res J Appl Sci Eng Technol 5:829–841. https://doi.org/10.19026/rjaset.5.5029

181. Iroba KL, Mellmann J, Weigler F et al (2011) Particle velocity profiles and residence time distribution in mixed-flow grain dryers. Granul Matter 13:159–168. https://doi.org/10.1007/s10035-010-0222-7
182. Mellmann J, Iroba KL, Metzger T et al (2011) Moisture content and residence time distributions in mixed-flow grain dryers. Biosyst Eng 109:297–307. https://doi.org/10.1016/j.biosystemseng.2011.04.010
183. Patwa A, Ambrose RPK, Casada ME (2016) Discrete element method as an approach to model the wheat milling process. Powder Technol 302:350–356. https://doi.org/10.1016/j.powtec.2016.08.052
184. He X, Jiao W, Wang C, Cao W (2019) Influence of surface roughness on the pump performance based on computational fluid dynamics. IEEE Access 7:105331–105341. https://doi.org/10.1109/access.2019.2932021
185. Zhou L, Deshpande K, Zhang X, Agarwal RK (2020) Process simulation of chemical looping combustion using ASPEN plus for a mixture of biomass and coal with various oxygen carriers. Energy 195:116955. https://doi.org/10.1016/j.energy.2020.116955
186. Devarampally DR (2017) Development of two-way coupled CFD–DEM model for top spray fluid bed granular using star CCM +. The State University of New Jersey, Rutgers
187. Drew DA (1983) Mathematical modeling of two-phase flow. Annu Rev Fluid Mech 15:261–291. https://doi.org/10.1146/annurev.fl.15.010183.001401
188. Yang Y, Zhou L, Shi W et al (2020) Interstage difference of pressure pulsation in a three-stage electrical submersible pump. J Pet Sci Eng. https://doi.org/10.1016/j.petrol.2020.107653
189. ANSYS Fluent Inc. (2009) Turbulence. In: ANSYS I, ANSYS Europe L (eds) Ansys Fluent 12.0 Theory Guide, 12th ed. SAS IP, Inc., Canonsburg, pp 1–58
190. Launder BE (1972) Lectures in mathematical models of turbulence. Academic Press, London, New York
191. Launder BE, Spalding DB (1974) The numerical computation of turbulent flows. Comput Methods Appl Mech Eng 3:269–289. https://doi.org/10.1016/0045-7825(74)90029-2
192. Boysan F, Ayers WH, Swithenbank J (1982) A fundamental mathematical modelling approach to cyclone design. Chem Eng Res Des 60:222–230
193. Narasimha M, Brennan MS, Holtham PN (2006) Numerical simulation of magnetite segregation in a dense medium cyclone. Miner Eng 19:1034–1047. https://doi.org/10.1016/j.mineng.2006.03.013
194. Orszag SA, Yakhot V, Flannery WS, Boysan F (1993) Renormalization group modeling and turbulence simulations. In: International conference, Near-wall turbulent flows. Elsevier, Tempe, Arizona, p 1031
195. Azadi M, Azadi M, Mohebbi A (2010) A CFD study of the effect of cyclone size on its performance parameters. J Hazard Mater 182:835–841. https://doi.org/10.1016/j.jhazmat.2010.06.115
196. Soe TM, Khaing SY (2017) Comparison of turbulence models for computational fluid dynamics simulation of wind flow on cluster of buildings in mandalay. Int J Sci Res Publ 7:337–350
197. Gimbun J, Chuah TG, Fakhru'l-Razi A, Choong TSY (2005) The influence of temperature and inlet velocity on cyclone pressure drop: a CFD study. Chem Eng Process 44:7–12. https://doi.org/10.1016/j.cep.2004.03.005
198. Griffiths WD, Boysan F (1996) Computational fluid dynamics (CFD) and empirical modelling of the performance of a number of cyclone samplers. J Aerosol Sci 27:281–304. https://doi.org/10.1016/0021-8502(95)00549-8
199. Ma L, Ingham DB, Wen X (2000) Numerical modelling of the fluid and particle penetration through small sampling cyclones. J Aerosol Sci 31:1097–1119. https://doi.org/10.1016/S0021-8502(00)00016-1
200. Gibson MM, Launder BE (1978) Ground effects on pressure fluctuations in the atmospheric boundary layer. J Fluid Mech 86:491–511. https://doi.org/10.1017/S0022112078001251
201. Launder BE, Reece GJ, Rodi W (1975) Progress in the development of a Reynolds-stress turbulence closure. J Fluid Mech 68:537–566. https://doi.org/10.1017/S0022112075001814
202. Wan G, Sun G, Xue X, Shi M (2008) Solids concentration simulation of different size particles in a cyclone separator. Powder Technol 183:94–104. https://doi.org/10.1016/j.powtec.2007.11.019
203. Xiang RB, Lee KW (2005) Numerical study of flow field in cyclones of different height. Chem Eng Process 44:877–883. https://doi.org/10.1016/j.cep.2004.09.006
204. Gronald G, Derksen JJ (2011) Simulating turbulent swirling flow in a gas cyclone: a comparison of various modeling approaches. Powder Technol 205:160–171. https://doi.org/10.1016/j.powtec.2010.09.007
205. Parvaz F, Hosseini SH, Elsayed K, Ahmadi G (2020) Influence of the dipleg shape on the performance of gas cyclones. Sep Purif Technol 233:116000. https://doi.org/10.1016/j.seppur.2019.116000
206. Inc. AF (2001) Modeling Turbulence. In: ANSYS I, ANSYS Europe L (eds) ANSYS Fluent Guide, 12th ed. SAS IP, Inc., Canonsburg, pp 1–102
207. Houben JJH, Weiss C, Brunnmair E, Pirker S (2016) CFD simulations of pressure drop and velocity field in a cyclone separator with central vortex stabilization rod. J Appl Fluid Mech 9:487–499
208. Talbi K (2011) An experimental study and a numerical simulation of the turbulent flow under the vortex finder of a cyclone separator an experimental study and a numerical simulation of the turbulent flow under the vortex finder of a cyclone separator. J Appl Fluid Mech 4:69–75
209. Rotta JC (1962) Turbulent boundary layers in incompressible flow. Prog Aerosp Sci 2:1–95. https://doi.org/10.1016/0376-0421(62)90014-3
210. Maxey MR, Riley JJ (1983) Equation of motion for a small rigid sphere in a nonuniform flow. Phys Fluids 26:883–889. https://doi.org/10.1063/1.864230
211. Casas G, Mukherjee D, Celigueta MA et al (2017) A modular, partitioned, discrete element framework for industrial grain distribution systems with rotating machinery. Comput Part Mech 4:181–198. https://doi.org/10.1007/s40571-015-0089-9
212. Lun CKK (2000) Numerical simulation of dilute turbulent gas-solid flows. Int J Multiph Flow 26:1707–1736. https://doi.org/10.1016/S0301-9322(99)00106-8
213. Oesterlé B, Bui Dinh T (1998) Experiments on the lift of a spinning sphere in a range of intermediate Reynolds numbers. Exp Fluids 25:16–22. https://doi.org/10.1007/s003480050203
214. Saffman PG (1965) The lift on a small sphere in a slow shear flow. J Fluid Mech 22:385–400. https://doi.org/10.1017/S0022112065000824
215. Saffman PG (1968) The lift on a small sphere in a slow shear flow: corrigendum. J Fluid Mech 31:624–624. https://doi.org/10.1017/S0022112068999990
216. Mei R (1992) An approximate expression for the shear lift force on a spherical particle at finite reynolds number. Int J Multiph Flow 18:145–147. https://doi.org/10.1016/0301-9322(92)90012-6
217. Ren B, Zhong W, Chen Y et al (2012) Particuology CFD-DEM simulation of spouting of corn-shaped particles. Particuology 10:562–572. https://doi.org/10.1016/j.partic.2012.03.011

218. Yuan J, Wu C, Li H et al (2018) Movement rules and screening characteristics of rice-threshed mixture separation through a cylinder sieve. Comput Electron Agric 154:320–329. https://doi.org/10.1016/j.compag.2018.09.012
219. Karimi H, Dehkordi AM (2015) Prediction of equilibrium mixing state in binary particle spouted beds: effects of solids density and diameter differences, gas velocity, and bed aspect ratio. Adv Powder Technol 26:1371–1382. https://doi.org/10.1016/j.apt.2015.07.013
220. Wang Z, Teng Y, Liu M (2019) A semi-resolved CFD–DEM approach for particulate flows with kernel based approximation and Hilbert curve based searching strategy. J Comput Phys 384:151–169. https://doi.org/10.1016/j.jcp.2019.01.017
221. Elghobashi S (1994) On predicting particle-laden turbulent flows. Appl Sci Res 52:309–329. https://doi.org/10.1007/BF00936835
222. Elghobashi S (1991) Particle-laden turbulent flows: direct simulation and closure models. Appl Sci Res 48:301–314. https://doi.org/10.1007/BF02008202
223. Zhao H, Zhao Y (2019) CFD–DEM simulation of pneumatic conveying in a horizontal channel. Int J Multiph Flow 118:64–74. https://doi.org/10.1016/j.ijmultiphaseflow.2019.06.003
224. Elsayed K, Lacor C (2014) Analysis and optimisation of cyclone separators geometry using RANS and LES methodologies. Turbul Interact Notes Numer Fluid Mech Multidiscip Des 125:65–74. https://doi.org/10.1007/978-3-662-43489-5
225. Potapov A, Chen X, Donohue T, Wheeler C (2013) Computer simulation of airflow around transfer chutes via linked discrete element method: computational fluid dynamics approach. In: 11th international congress on bulk materials storage, Handling and transportation
226. Ganser GH (1993) A rational approach to drag prediction nonspherical particles. Powder Technol 77:143–152. https://doi.org/10.1016/0032-59109(93)80051-b
227. ESSS-Rocky (2015) Rocky User Manual, 4.0. Rocky DEM, Inc., Rio de Janeiro, Brazi
228. Mahajan VV, Nijssen TMJ, Fitzgerald BW, et al (2017) Fluidization of spherocylindrical particles. In: 8th international conference on micromechanics on granular media
229. Buist KA, Jayaprakash P, Kuipers JAM et al (2017) Magnetic particle tracking for nonspherical particles in a cylindrical fluidized bed. AIChE J 63:5335–5342. https://doi.org/10.1002/aic.15854
230. Laín S, Sommerfeld M (2008) Euler/Lagrange computations of pneumatic conveying in a horizontal channel with different wall roughness. Powder Technol 184:76–88. https://doi.org/10.1016/j.powtec.2007.08.013
231. Kuang SB, Yu AB, Zou ZS (2009) Flow regimes in vertical pneumatic conveying. Ind Eng Chem Res 1145:1005–1008. https://doi.org/10.1063/1.3179812
232. Traoré P, Laurentie JC, Dascalescu L (2015) An efficient 4 way coupling CFD-DEM model for dense gas-solid particulate flows simulations. Comput Fluids 113:65–76. https://doi.org/10.1016/j.compfluid.2014.07.017
233. Carruthers AC, Filippone A (2005) Aerodynamic drag of streamers and flags. J Aircr 42:976–982. https://doi.org/10.2514/1.9754
234. Gent SP, Gent SP (2009) Computational modeling of multiphase fibrous flows for simulation based engineering. Iowa State University
235. Schiller L, Naumann AZ (1933) Ueber die grundlegenden Berechnungen bei der Schwerkraftaufbereitung. Ver Deut Ing 77:317–320
236. Fox RW, Mcdonald's AL, (2011) Introdution to fluid mechanics, 8th edn. John Wiley and Sons, INC., New York
237. Liu R, Zhou Z, Xiao R, Yu A (2019) CFD-DEM modelling of mixing of granular materials in multiple jets fluidized beds. Powder Technol. https://doi.org/10.1016/j.powtec.2019.08.002
238. Dallavalle JM (1948) Micromeritics: the technology of fine particles, 2nd edn. Pitman Publishing Corp, New York
239. ESSS-Rocky (2016) Particle drag laws implemented in the Rocky DEM–CFD oneway and twoway coupling modules. In: Rocky E (ed) Rocky-Dem Technical Manual, 4.13. Rocky DEM, Inc., Rio de Janeiro, Brazi, pp 1–9
240. Wen CY, Yu YH (1966) Mechanics of fluidization. Chem Eng Prog Symp Ser 162:100–111
241. Benzarti S, Mhiri H, Bournot H (2012) Drag models for simulation gas-solid flow in the bubbling fluidized bed of FCC particles. Int J Chem Mol Eng 61:1138–1143
242. Ergun S (1952) Fluid flow through packed columns. Chem Eng Prog 48:89–94
243. Knight C, O'Sullivan C, van Wachem B, Dini D (2020) Computing drag and interactions between fluid and polydisperse particles in saturated granular materials. Comput Geotech 117:103210. https://doi.org/10.1016/j.compgeo.2019.103210
244. Huilin L, Gidaspow D (2003) Hydrodynamics of binary fluidization in a riser: CFD simulation using two granular temperatures. Chem Eng Sci 58:3777–3792. https://doi.org/10.1016/S0009-2509(03)00238-0
245. Di Felice R (1994) The voidage function for fluid-particle interaction systems. Int J Multiph Flow 20:153–159. https://doi.org/10.1016/0301-9322(94)90011-6
246. Wang Q, Melaaen MC, De Silva SR (2001) Investigation and simulation of a cross-flow air classifier. Powder Technol 120:273–280. https://doi.org/10.1016/S0032-5910(01)00282-0
247. Badretdinov I, Mudarisov S, Lukmanov R et al (2019) Mathematical modeling and research of the work of the grain combine harvester cleaning system. Comput Electron Agric 165:104966. https://doi.org/10.1016/j.compag.2019.104966
248. Mudarisov S, Khasanov E, Rakhimov Z et al (2017) Specifying two-phase flow in modeling pneumatic systems performance of farm machines specifying two-phase flow in modeling pneumatic systems performance of farm machines. J Mech Eng Res Dev 40:706–715. https://doi.org/10.7508/jmerd.2017.04.018
249. Li Y, Xu L, Zhou Y et al (2018) Effects of throughput and operating parameters on cleaning performance in air-and-screen cleaning unit: A computational and experimental study. Comput Electron Agric 152:141–148. https://doi.org/10.1016/j.compag.2018.07.019
250. Enchen J, Zhanfeng S, Zhiyang P, Lijun W (2014) Numerical simulation based on CFD-DEM and experiment of grain moving laws in Inrtia separation chamber. J Agric Mach 45:117–122. https://doi.org/10.6041/j.issn.1000-1298
251. Balafoutis A, Beck B, Fountas S et al (2017) Precision agriculture technologies positively contributing to GHG emissions sustainability precision agriculture technologies positively contributing to GHG emissions mitigation. Farm Prod Econ Sustain 9:1339. https://doi.org/10.3390/su9081339
252. Minfeng J, Yongqian D, Hongfeng Y et al (2018) Optimal structure design and performance tests of seed metering device with fluted rollers for precision wheat seeding machine. IFAC Pap OnLine 17:509–514. https://doi.org/10.1016/j.ifacol.2018.08.158
253. Singh RC, Singh G, Saraswat DC (2005) Optimisation of design and operational parameters of a pneumatic seed metering device for planting cottonseeds. Biosyst Eng 92:429–438. https://doi.org/10.1016/j.biosystemseng.2005.07.002
254. Jianbo Z, Junfang X, Yong Z, Shun Z (2014) Design and experimental study of the control system for precision seed-metering device. Int J Agric Biol Eng 7:13–18. https://doi.org/10.3965/j.ijabe.20140703.002

255. Kamgar S, Eslami M, Maharlouie M (2013) Design, development and evaluation of a mechatronic transmission system to improve the performance of a conventional row crop planter. Intl J Agron Plant Prod 4:480–487
256. Dandan H, Dongxing Z, Li Y et al (2017) EDEM-CFD simulation and experiment of working performance of inside-filling air-blowing seed metering device in maize. Trans Chin Soc Agric Eng 33:23–31
257. Lei X, Liao Y, Zhang Q et al (2018) Numerical simulation of seed motion characteristics of distribution head for rapeseed and wheat. Comput Electron Agric 150:98–109. https://doi.org/10.1016/j.compag.2018.04.009
258. Weigler F, Mellmann J (2014) Investigation of grain mass flow in a mixed flow dryer. Particuology 12:33–39. https://doi.org/10.1016/j.partic.2013.04.004
259. Bacelos MS, Almeida PIF (2011) Modelling of drying kinetic of potatoes taking into account shrinkage. Procedia Food Sci 1:713–721. https://doi.org/10.1016/j.profoo.2011.09.108
260. Oksanen T (2018) Controlling air flow in recirculating mixed flow batch dryer with double bed mode. Comput Electron Agric 149:133–138. https://doi.org/10.1016/j.compag.2017.07.018
261. Weigler F, Mellmann J, Franke G, Scaar H (2013) Experimental studies on a newly developed mixed-flow dryer. Dry Technol 31:1736–1743. https://doi.org/10.1080/07373937.2013.806929
262. Scaar H, Franke G, Weigler F et al (2016) Experimental and numerical study of the airflow distribution in mixed-flow grain dryers. Dry Technol 34:595–607. https://doi.org/10.1080/07373937.2015.1064946
263. Azmir J, Hou Q, Yu A (2019) CFD-DEM simulation of drying of food grains with particle shrinkage. Powder Technol 343:792–802. https://doi.org/10.1016/j.powtec.2018.11.097
264. Azmir J, Hou Q, Yu A (2019) CFD-DEM study of the effects of food grain properties on drying and shrinkage in a fluidised bed. Powder Technol. https://doi.org/10.1016/j.powtec.2019.10.021